

MODELING TISSUE POLARIZATION AND SYMMETRY BREAKING
IN DEVELOPMENT AND DISEASE

Julio Monti Belmonte

Submitted to the faculty of the University Graduate School

in partial fulfillment of the requirements

for the degree

Doctor of Philosophy

in the Department of Physics

Indiana University

December, 2014

UMI Number: 3669289

All rights reserved

INFORMATION TO ALL USERS

The quality of this reproduction is dependent upon the quality of the copy submitted.

In the unlikely event that the author did not send a complete manuscript and there are missing pages, these will be noted. Also, if material had to be removed, a note will indicate the deletion.



UMI 3669289

Published by ProQuest LLC (2014). Copyright in the Dissertation held by the Author.

Microform Edition © ProQuest LLC.

All rights reserved. This work is protected against unauthorized copying under Title 17, United States Code



ProQuest LLC.
789 East Eisenhower Parkway
P.O. Box 1346
Ann Arbor, MI 48106 - 1346

Accepted by the Graduate Faculty, Indiana University, in partial fulfillment of the
requirements for the degree of Doctor of Philosophy.

Doctoral Committee

Prof. James A. Glazier, Ph.D.

Prof. John M. Beggs, Ph.D.

Prof. Sima Setayeshgar, Ph.D.

Prof. Joseph R. Pomeroy, Ph.D.

Date of Defense

14 April, 2014

Dedicated to my parents and my wife.

ACKNOWLEDGEMENTS

I would like to thank:

- My advisor Dr. James A. Glazier for everything he taught me, all the opportunities he provided and doors he opened to me.
- Dr. Gilberto Lima Thomas for using his influence to convince James to take me as a graduate student. I hope James is not mad at you.
- Dr. Rita de Almeida, for reading the thesis manuscript and provided valuable feedback. I would also like to thank you for all your advice and guidance throughout all those years.
- Dr. Maciek Swat, Mr. Randy Heiland and Mr. Benjamim Zailten for their help with CompuCell3D and Python.
- My colleagues, Dr. Abbas Shirinifard, whom I looked to as a model PhD student, and Dr. Susan Hester, with whom I worked closely in my first two years on the multi-scale somitogenesis project. I look forward to opportunities to work with you again in the future.
- To my co-workers in James' lab: Dr. J. Scott Gens, Dr. Jim P. Sluka, Dr. Srividhya Jeyaraman, Dr. Nikodem J. Poplawski, Dr. Dragos Amarie, Mr. Alin Cosmanescu and Mr. Andy Somogy for companionship and fruitful discussions about science, programming, academic life and similar topics; and Ms. Talia Andereson and Ms. Debbie McKinney for all their assistance with grants and travel arrangements.

- Dr. Maciek Swat, Dr. Octavian Voiculescu and Dr. Mansoor Raza for introducing me to convergent-extension processes during chicken primitive streak formation. Without them I would never have built the pulling-force model of cell intercalation.

- Dr. James A. Sharpe and Dr. Gaja Lesnicar-Pucko for believing in me and giving me the opportunity to apply an early version of the cell-intercalation model to the study of chicken limb bud growth.

- Dr. Raymond Keller and his team at University of Virginia for valuable feedback regarding the cell-intercalation model.

- Dr. Claudio Stern for giving me the opportunity to work on ectopic somites. This very challenging and exciting project gave me my first opportunity to demonstrate the power of the cell polarization model.

- Dr. Sherry G. Clendenon and Dr. Robert L. Bacallao for providing my first opportunity to step outside the realm of developmental biology and work on the mechanisms of an important human disease.

- The funding agencies that paid for all of this work: National Institutes of Health/National Institute of General Medical Sciences grants R01 GM076692 and R01 GM077138; QuanTissue/ESF short visit grant 4892; an Indiana University OVPR Internal Collaborative Research Grant, the Biocomplexity Institute at Indiana University and the Physics Department at Indiana University.

- My Family. I would not be able to move forward without knowing that you will always be there to support me.

- And finally God, Who made all this possible and to Whom I am eternally grateful.

Julio Monti Belmonte

MODELING TISSUE POLARIZATION AND SYMMETRY BREAKING
IN DEVELOPMENT AND DISEASE

The development of all complex multi-cellular organisms involves some sort of symmetry breaking. As an organism develops from an egg, the patterns derived by successive symmetry breakings – the form – must be maintained against the entropic force represented by uncontrolled cell growth, movement and death. It is this balance and the mechanisms used for such end that characterize and define each species. Proper understanding of such processes requires much more than knowledge of gene expression patterns – it requires knowledge of the interactions between gene regulation, the forces cells generate and extracellular structures. The complexity of these processes and the difficulty of performing controlled experiments at the interface between cell and tissue scales make computer simulations essential tools to understand which set of cell behaviors can lead to the normal development of a tissue and how they operate. We therefore require a proper set of mathematical approaches to describe biological symmetry breaking and pattern generation. In this thesis I have developed and refined numerical techniques that allow concurrent simulations of symmetry breaking events within cells (the dynamic domains model) and by cells in tissues (the dynamic links model). Dynamic domains can model cell polarization and dynamic links can exert forces between cells, leading to cell rearrangement, tissue

reconstruction and the generation of new structures. I have applied these techniques to study three different biological processes: limb bud growth, somitogenesis and the onset of human polycystic kidney disease. Each of these studies led to unexpected conclusions: In the first two I propose mechanism for two basic developmental processes that drastically differ from the accepted model. In the latter, I offer the first explanation of how a single defective cell in a kidney can lead to the formation of cysts.

Prof. James A. Glazier, Ph.D.

Prof. John M. Beggs, Ph.D.

Prof. Sima Setayeshgar, Ph.D.

Prof. Joseph R. Pomerening, Ph.D.

TABLE OF CONTENTS

ACKNOWLEDGEMENTS.....	iv
TABLE OF CONTENTS.....	ix
LIST OF FIGURES.....	xii
LIST OF TABLES	xv
ACRONYMS	xvi
CHAPTER 1 – INTRODUCTION	1
The general problem of development	3
The object of my thesis.....	5
Outline	6
CHAPTER 2 – THE CELLULAR POTTS/GGH MODEL.....	9
Cell-based models.....	9
The Cellular Potts/GGH model.....	13
Modeling of cell compartments using CPM/GGH	17
CHAPTER 3 – CELL POLARITY AND THE <i>SUBCELLULAR</i> POTTS/GGH MODEL	21
Dynamic domain model	22
Membrane restriction	24
CPM scope and the <i>sub</i> Cellular Potts/GGH	26
Molecular-Cell Integration (MCI) model	28
Cell polarity models – Apico-basal polarity.....	29
Cell polarity models – PCP.....	31
Extensions of cell polarity models.....	34
CHAPTER 4 – CONVERGENT-EXTENSION.....	36
Pulling forces.....	36
Other uses of links in the CP/GGH model	39
The purpose of this chapter	41
Convergent-extension.....	41
Filopodial tension model	43
Metrics	46

Surface tension	47
Parameter sensitivity analysis	49
Size effects on CE.....	52
Contact-mediated pulling	53
Polarization misalignment	55
Heterogeneous cultures	56
3D versions	59
CHAPTER 5 – LIMB BUD GROWTH.....	64
Background.....	65
How does a limb growth?	66
Project.....	70
Experimental techniques.....	71
Experimental Results.....	72
3D limb bud model.....	79
Random vs. oriented cell divisions	81
Direct migration.....	83
Ectoderm-oriented cell intercalation.....	83
A new role for the AER-FGF signaling?.....	88
Discussion	90
CHAPTER 6 – POLYCYSTIC KIDNEY DISEASE	93
The disease	94
Recent findings	95
Project.....	96
3D renal tubule model.....	98
Contact-inhibition of cell proliferation model.....	100
Cell divisions	102
Cystogenesis model	104
Cadherin-8 knock-in model.....	106
Cadherin-8 acts by reducing normal cell adhesion	108
Adhesion vs proliferation ADPKD initiation patterns	110

Conclusion	112
CHAPTER 7 – SOMITES <i>WITH</i> AND <i>WITHOUT</i> A CLOCK	114
What is somitogenesis?.....	115
Do we really know how somites form?.....	118
A multi-scale model of somitogenesis.....	119
Model of cell differentiation	125
An experimental challenge to the clock and wavefront model.....	127
What does control somite formation?.....	133
A self-organizing somitogenesis model.....	134
Results	139
Back to normal somites	145
Discussion	148
REFERENCES.....	151
CURRICULUM VITAE.....	

LIST OF FIGURES

Figure 1.1 – Cell Polarity	2
Figure 2.1 – Cell-based computational models	11
Figure 2.2 – Cellular Potts/GGH model	12
Figure 2.3 – Cell compartments.....	17
Figure 3.1 – Dynamic domains models.....	22
Figure 3.2 – Membrane restriction	25
Figure 3.3 – CPM/GGH scope and extensions	27
Figure 3.4 – Apico-Basal polarity model	30
Figure 3.5 – Polar PCP model results	34
Figure 3.6 – Boundary PCP model.....	35
Figure 4.1 – Use of dynamic length constraints.....	40
Figure 4.2 – Force-driven cell intercalation model	44
Figure 4.3 – Simulation snapshots and measured metrics.....	46
Figure 4.4 – Effects of force and surface tension on the 2D intercalation model.....	48
Figure 4.5 – Parameter sensitivity analysis	50
Figure 4.6 – Size effects on the simulation results	52
Figure 4.7 – Contact-mediated pulling.....	54
Figure 4.8 – Results for different levels of polarization misalignment.....	55
Figure 4.9 – Results for heterogeneous tissues	57
Figure 4.10 – Final shapes of simulations with heterogeneous tissues	58
Figure 4.11 – 3D cell intercalation model versions.....	60
Figure 4.12 – Dependence of τ and κ with θ_{\max} in the 3D versions.....	61
Figure 5.1 – Limb bud initiation in chick.....	65
Figure 5.2 – Proposed limb bud behaviors.....	68
Figure 5.3 – In ovo imaging.....	71
Figure 5.4 – Division orientation.....	72

Figure 5.5 – Mesenchymal cell shapes	74
Figure 5.6 – Cell migration analysis	76
Figure 5.7 – Cell registration and time-lapse analysis	77
Figure 5.8 – 3D limb bud model	79
Figure 5.9 – Division orientations and limb bud shapes	82
Figure 5.10 – Migration vs. cell intercalation	84
Figure 5.11 – Toy model for limb elongation	85
Figure 5.12 – Filopodia and Golgi orientations.....	87
Figure 5.13 – New limb bud growth model.....	89
Figure 6.1 – Autosomal dominant polycystic kidney disease	94
Figure 6.2 – Renal tubule and renal epithelial cell models.....	99
Figure 6.3 – Averaging cell surface measurements	101
Figure 6.4 – Division planes.....	103
Figure 6.5 – Cystogenesis simulation	105
Figure 6.6 – ADPKD simulation.....	107
Figure 6.7 – Cadherin-8 expression reduces cell-cell adhesion	109
Figure 6.8 – ADPKD initiation patterns.....	111
Figure 6.9 – In vitro cyst formation pattern	112
Figure 7.1 – Chick somitogenesis	116
Figure 7.2 – Schematic version of the clock and wavefront hypothesis.....	117
Figure 7.3 – Clock and wavefront complexity	118
Figure 7.4 – Multi-scale model of somitogenesis via the clock and wavefront mechanism....	120
Figure 7.5 – Modeled network for the clock.....	123
Figure 7.6 – Clock periodicity and pseudo-travelling waves.....	124
Figure 7.7 – Ad hoc differentiation model.....	125
Figure 7.8 – Multi-scale model results.....	127
Figure 7.9 – Ectopic somite experiment	128
Figure 7.10 – Ectopic somite transplant.....	129
Figure 7.11 – Clock and somite expressions on ectopic somites.....	130

Figure 7.12 – Motor axons and neural crest staining on grafts	132
Figure 7.13 – Ectopic somite model	135
Figure 7.14 – Ectopic somite simulation with 198 cells	140
Figure 7.15 – Somite sizes	141
Figure 7.16 – Number of cells and somite formation	142
Figure 7.17 – Graft geometry and somite formation	144
Figure 7.18 – Ectopic somite formation on a PSM-like strip	145
Figure 7.19 – Wavefront speed versus somite formation	146
Figure 7.20 – Somitogenesis with self-organizing somites	147

LIST OF TABLES

Table 2.1 – Contact energies between compartments of different cells (different cell-index θ) used in Figure 2.3b.	18
Table 2.2 – Contact energies between compartments of the same cell (same cell-index θ) used in Figure 2.3b.	18
Table 3.1 – Internal contact energies between domains of the same cell (same cluster index θ) used for models shown in Figure 3.1.	23
Table 3.2 – External contact energies between domains of different cells (distinct cluster indexes θ) used in Figure 3.1d.	24
Table 3.3 – External contact energies between domains of different cells shown in Figure 3.2c-d.	26
Table 3.4 – Internal contact energies between domains of the same cell used shown in Figure 3.2.	26
Table 3.5 – Internal contact energies between domains of the same cell used on Figure 3.4.	31
Table 3.6 – External contact energies between domains of different cells used on Figure 3.4.	31
Table 3.7 – Internal contact energies between domains of the same cell used on Figure 3.4.	32
Table 3.8 – External contact energies between domains of different cells used on Figure 3.4.	32
Table 4.1 – List of reference parameters values used in the simulations.	45
Table 6.1 – Overview of kidney cadherin expression in development, healthy adults and PKD.	96

ACRONYMS

AER – Apical Ectodermal Ridge

AP – Anterior-Posterior axis

ADPKD – Autosomal Dominant Polycystic Kidney Disease

CC3D – CompuCell3D

CE – Convergent-Extension

CI – Contact-Inhibition

CPM – Cellular Potts Model

DV – Dorso-Ventral axis

ECM – Extra-Cellular Matrix

GGH – Glazier-Graner-Hogeweg model

GRN – Gene Regulatory Network

MCI – Molecular-Cell Integration model

MCS – Monte Carlo Step

ML – Medio-Lateral axis

MTE – Mesenchymal to Epithelial Transition

ODE – Ordinary Differential Equation

OPT – Optical Projection Tomography

PCP – Planar Cell Polarity

PD – Proximo-Distal axis

PDE – Partial Differential Equation

PS – Primitive Streak

PSM – Pre-Somitic Mesoderm

CHAPTER 1 – INTRODUCTION

The development of all complex multi-cellular organisms involves a controlled sequence of symmetry breakings. That is an essential step in the formation of any pattern. The trigger may be an internal event, such as the first division of the fertilized egg, some external factor as an environmental cue, or an inherited bias from the mother. Different species evolved to take advantage of different cues to define their primary spatial differentiation, but during the development of all metazoan eukaryotes many other symmetry breaking events are required.

As an organism develops, the pattern gained by the successive symmetry breaking events – the form – must be maintained against the entropic forces of uncontrolled cell growth, movement and death. The balance between growth and form, and the mechanisms used for such an end is what characterizes and defines each species.

Symmetry breaking happens at least at two distinct scales: at the cell-scale, when individual cells lose their spatial, or functional, spherical symmetry; and at the tissue-scale, when a homogeneous group of cells rearrange, differentiate, grow and/or change shape in a specific way to form a more complex structure.

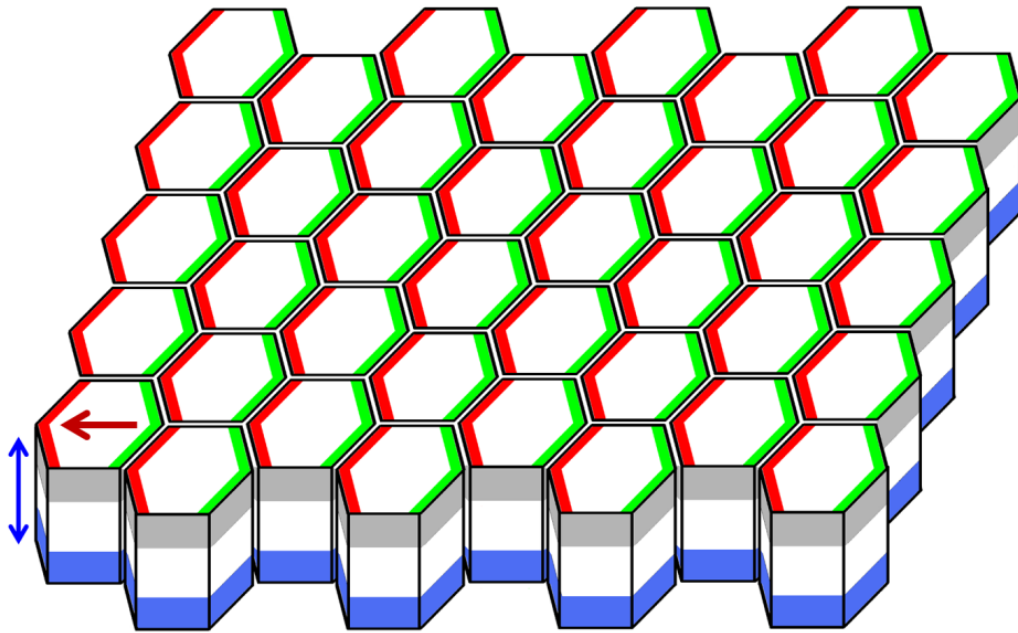


Figure 1.1 - Cell Polarity

Red and green stripes show cells' proximal and distal domains of PCP, respectively. The red arrow shows PCP orientation. Grey and blue stripes show respectively the apical and basal domains of cells which also have Apico-basal polarity. The blue arrow indicates the Apico-Basal orientation.

Cell asymmetry results from the spatial compartmentalization of molecular complexes and cytoskeletal rearrangement, a process called *polarization*. There are many types of polar cells: neurons, leukocytes, fibroblasts etc. Here I will focus on epithelial cells, which has two basic kinds of cell polarization: *Apical-Basal* polarity, where an cell have a defined basal surface that secretes and preferably abuts an *extra-cellular matrix (ECM)*, and an apical surface on the opposing side that usually faces a lumen-filled cavity (Figure 1.1,

blue arrow); and *Planar Cell Polarity (PCP)*, where the cells on an epithelium sheet are polarized *parallel* to the plane of the sheet and orthogonal to the Apical-Basal polarity axis (Figure 1.1, red arrow).

At the tissue scale, loss of tissue symmetry can result from external cues, such as morphogen gradients and boundary signals, or from a self-organizing process emerging from changes in properties of their constituent cells – an asymmetry at the cell level propagating up in scale.

The general problem of development

Modern molecular biology has decoded and mapped much of the molecular pathways active during development at the expense of the study of cell-scale and tissue-scale morphological mechanisms, which dominated developmental biology before WWII. Experiments that relate cell-scale to tissue-scale behaviors are challenging both because the cell behaviors that drive development are hard to control and because the development of appropriate tools to measure cell shapes, ECM properties, chemical concentrations, and force generation have lagged the development of molecular assays.

Another approach is to use mathematical models and computer simulations to understand how specific sets of cell behaviors can lead to the robust self-organization of a tissue. All experimental work should lead or contribute to the formation of a theory or theoretical description of the object of study, be in mathematical form or not. Just like

experimental molecular biology feeds into theoretical systems biology and computational bioinformatics, which, in turn guide future experiments in that area, cell- and tissue-level developmental biology should feed into and be guided by a similar theoretical framework. Unfortunately, we still lack a proper theoretical framework to describe developmental processes and the enormous heterogeneity of developmental patterns may never be unified within a single mathematical formulation. Nevertheless, modeling of developmental processes at the cellular and tissue level is a growing trend and is getting increasing attention among experimental developmental biologists.

Most of these models, however, are limited in scope. Often they rely on an external morphogens or are single scaled, *i.e.*, they assume that the cells are already differentiated and explore how a tissue changes/develops given pre-defined set of cell behaviors. These two methodologies, while valid within certain contexts and necessary as a first approach, are limited for two reasons: i) it is unlikely that morphogens are the main patterning mechanism operating during development as the length scales are much bigger than the typical diffusion length of the secreted molecules¹; ii) they ignore the fact that most patterning arises as emergent processes from the cell level – again, an initial asymmetry propagating up in scale.

¹ A possible solution is the use of morphogen patterning on a growing domain, which not only solves the diffusion length problem, but proves to be a very robust mechanism.

The object of my thesis

This thesis deals with the last objection: symmetry breaking, or patterning, at the tissue level is in many cases a reflection or consequence of a break of symmetry of the cells. Because the cells acquire a new behavior that is spatially asymmetric – or increase/decrease a pre-existing activity along an axis –, they self-organize and a global pattern emerges. Growth in this context can either be absent, irrelevant or an outcome of patterning.

Because many sets of mechanisms can yield the same final pattern, models that ignore this first step – a symmetry breaking at the cell level – may produce the correct pattern through the wrong mechanism. Chapter 6, *Limb Bud Growth*, provides a good example of this situation. While most modelers that I know agree that most tissue scale patterns are self-organized, there are but just a few models where the final patterns arise from an intrinsic property of the cells. Reasons to the scarcity of such models include the lack of quantitative biological data, greater complexity of models coupling cell polarization to tissue scale and the lack of convenient ways to simulate emergent polarization.

As part of my PhD research, I developed such techniques while I was modeling different developmental processes. While these mathematical techniques are derived from classical statistical physics methods, their biological application to model changing chemical distribution in cells during dynamic, self-organizing polarization is novel and required generalization and modification of classical statistical approaches. Similarly, I have extended the classic finite element spring approach, often used to model forces between cells, by controlling the springs dynamically in response to cell polarity.

I demonstrate the usefulness of these new modeling techniques to explain developmental phenomena in the second part of this thesis. I hope that these few examples will inspire others to apply them to build multi-cell, mechanistic models of the many other developmental, homeostatic and disease contexts where a tissue pattern emerges from interacting polarized cells.

Outline

This thesis is divided in two main parts: Methods and Applications. The first part is subdivided in the following three chapters:

- In *Chapter 2 – The Cellular Potts/GGH Model*, I review this modeling technique, compare it with other model methods and discuss in which ways to improve it.
- In *Chapter 3 – Cell Polarity and the Subcellular Potts/GGH Model*, I develop a method to model the two basic kinds of cell polarization (Apical-Basal and PCP).
- In *Chapter 4 – Convergent-Extension*, I develop and explore a method to model the generation of pulling forces between cells due to filopodia.

In the second part of this thesis I apply the developed methods to model specific biological processes. This part is subdivided in the following three chapters:

- In *Chapter 5 – Limb Bud Growth*, I use anisotropic pulling forces between cells to model the development of chicken limb bud.

- In *Chapter 6 – Polycystic Kidney Disease*, I use the polarization model to explore the possible causes for the onset of a human disease
- And in *Chapter 7 – Somites With and Without a Clock*, I use the polarization model and pulling forces between cells to model chick somitogenesis.

Parts of chapters 4-7 have been, or are currently being, published in scientific journals [1, 2] – although in a slightly different form, with more emphasis on the experimental work of our collaborators. The work on convergent-extension (Chapter 4) provides the first mathematical/computational formulation of a model for the driving force in active cell intercalation. Chapters 5 and 7 propose novel mechanical explanations to two developmental processes which were widely believed to result from other mechanisms, while Chapter 6 provides the first mechanical model of how a single defective cell can lead to lethal cyst formation in the kidney.

PART I

METHODS

CHAPTER 2 – THE CELLULAR POTTS/GGH MODEL

When it comes to agent-based modeling of biological cells, *i.e.* discrete models where the cell is taken as the basic unit, there are four general choices: cellular automata, center models, mesh models and *cellular Potts models (CPM)*, also known as *Glazier-Graner-Hogeweg (GGH)* models (Figure 2.1). I will briefly review and discuss all four before focusing on the CPM/GGH for the remainder of the thesis.

Cell-based models

Cellular automata models [3, 4] represent each cell as a site, or pixel, in a fixed lattice and therefore lack any shape attribute (Figure 2.1b). **Cell**² dynamics – movement, death,

² From this point on I will denote models of biological entities such as cell, tissues etc with bold fonts to avoid confusion with references to biological entities.

duplication (growth), differentiation etc – are updated simultaneously for all lattice sites and define the basic time unit of the model. Usually, two cells cannot occupy the same site at the same time, but some variations represent a density of cells on each site or use multiple parallel lattices to model, for example, cell and virus populations [5].

Center models [6, 7] represent each cell as a point in a lattice-free space (Figure 2.1c). **Cells** usually interact with each other via a Lenard-Jones type potential, with a hard core radius representing the compressibility limit of the cells and a resting distance between neighboring **cells** (Figure 2.1c'). Neighborhood is usually determined by Voronoi tessellation, which also serves as a way to determine the effective shape of the **cells**.

Mesh models [8, 9] represent the cell membrane as a series of connected nodes/membranes in a lattice-free space (Figure 2.1d). **Cell** movement results from node/membrane movement. The nodes/membranes usually experience spring-like and viscous forces and may be subjected to extra constraints (usually in the form of square potentials) to maintain **cell** volume (or area, in 2D simulations), defined as the space the connected nodes enclose (Figure 2.1d'). The model evolves by either minimizing the energy, or cost function, resulting from all the constraints or moving the nodes in the direction of the net force. Extra rules are used to model T1 events (when **cells** exchange neighbors) [10].

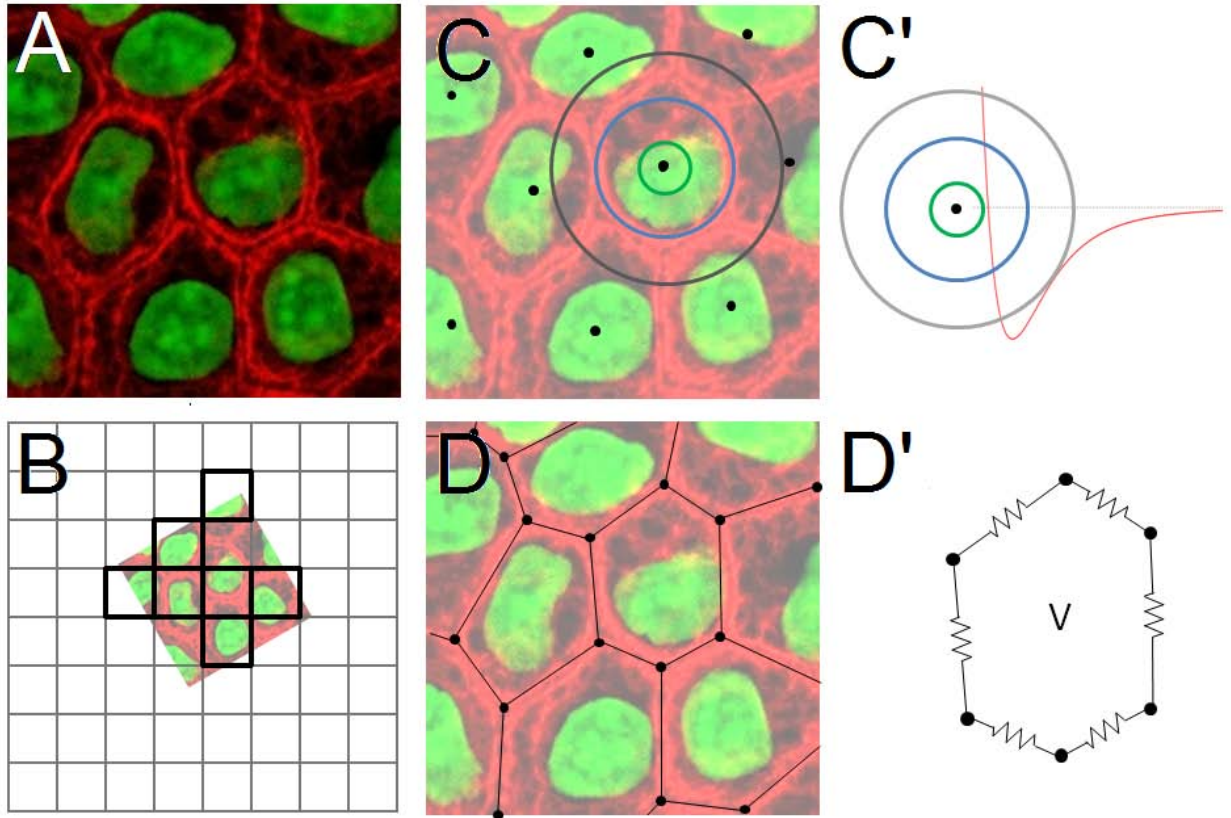


Figure 2.1 – Cell-based computational models

(A) Biological cells can be modeled by: (B) Cellular automata models, where each cell is a site on a regular lattice; (C-C') Center models, where each cell is a point in space (black dots on C) with an associate energetic potential (C'); (D-D') Mesh models, where the cell membranes are represented by connected nodes.

Cellular Potts model (CPM) [11-14], also known as *Glazier-Graner-Hogeweg (GGH)* model, represents each cell as a set of sites on a regular lattice (Figure 2.2). Assignments of lattice sites to **cells** changes stochastically, with probabilities governed by a cost function, where the **cells** properties are described. The time unit, called a *Monte Carlo Step (MCS)*, is defined as N update attempts, where N is the total number of lattice sites.

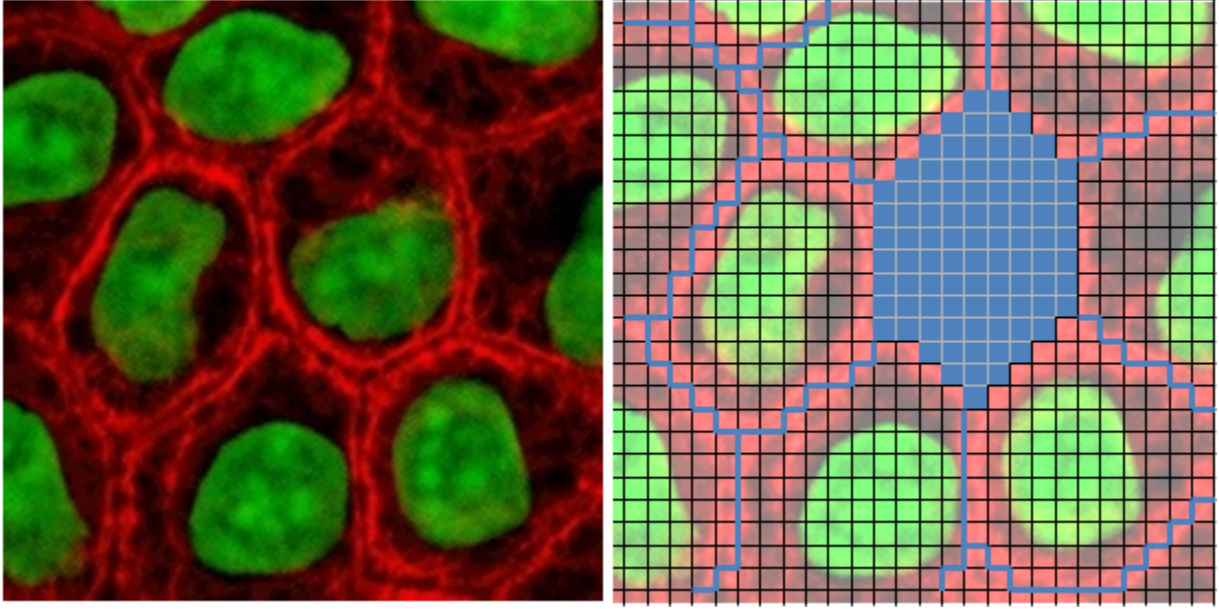


Figure 2.2 – Cellular Potts/GGH model

In CP/GGH models the cells are represented as a collection of sites on a lattice. The finer the grid, the better is the shape representation of the cells. Left: image of real epithelial cells. Right: a representation of the cells in a square lattice, with one of the cells highlighted.

Simple versions of cellular automata and center models assume that cells are radially symmetric. Although the latter admits some shape variations, the **cells** are still functionally symmetric. The two models can break the **cell** symmetry by associating a vector to each **cell**, so that some of their properties are biased in one direction, as in *boid/flock* models [15]. **Cells** in simple mesh and CP/GGH models are also functionally symmetric, but represent **cell** shapes explicitly. Specification of different edge properties (in mesh models), or oriented bias in the governing equations allows addition of functional/behavioral or shape anisotropies on each **cell**. For those reasons, those two models are usually chosen over the others when modeling epithelial tissues.

As pointed out on Chapter 1, polarized cells have surface domains with distinct properties and anisotropic internal structures. In both simple mesh and CP/GGH models, **cells** share contacting **edges**, which complicate representation of cell rotation and cell rearrangement. Mesh models can be adapted to the description of polarized cells by assigning different properties to each **cell edge** and/or by the use of double **edges**. In CP/GGH models representation of polarized cells can be done by the use of **cell compartments**, where the cell is represented by multiples sets of lattice sites, with each set corresponding to a different cellular region.

The Cellular Potts/GGH model

The CP/GGH model represents space as a regular *lattice of sites*, pixels or voxels, which are used to represent cells or other volume-excluding objects (Figure 2.2). Each lattice site has at least two attributes: its spatial localization in the lattice, \vec{i} ; and a *object- or domain-index* number, σ , which specifies which *object*, or *domain*, occupies that lattice site. A CPM/GGH *domain* may represent a biological cell, a subcellular compartment, a cluster of cells, a piece of non-cellular material, a fluid or the medium. The type of object that a domain represents is indicated by the *type index*, $\tau(\sigma)$. While each object/domain has a unique σ , many objects may share the same type index τ . For example, a simulation may involve hundreds of **cells** of type **mesenchyme**.

Each domain is spatially defined as the set of all lattice sites that share the same domain-index (σ). The movement of these domains results from a series of domain-index copies, where the domain-index σ of a particular lattice site \vec{i} ($\sigma_{\vec{i}}$) is copied to a neighboring site \vec{j} , which belongs to a different domain (*i.e.*, $\sigma_{\vec{i}} \neq \sigma_{\vec{j}}$). By definition, copies between lattice sites with the same domain-index do not change the state of the system.

This series of domain-index copies are regulated by an *effective energy*, or cost function (H). This effective energy reflects the state of the lattice at a particular time and is defined so that simulated **cells** and objects have the desired properties, behaviors and interactions, implemented via constraint terms in H . The effective energy in CPM/GGH simulations is not the actual energy of the biological cells and tissues being modeled but rather a phenomenological way to specify the factors that govern an object's properties, behaviors and dynamics in the model. In a typical CP/GGH model each cell is modeled as a single domain (σ) that has a defined volume and interacts via contact adhesion and/or repulsion with neighboring domains, so that H is given by the following equation:

$$(Eq. 2.1) \quad H = \overbrace{\sum_{\substack{\vec{i}, \vec{j} \\ \text{neighbors}}} J[\tau(\sigma_{\vec{i}}), \tau(\sigma_{\vec{j}})] \cdot [1 - \delta(\sigma_{\vec{i}}, \sigma_{\vec{j}})]}_{\text{contact energy}} + \overbrace{\sum_{\sigma} \lambda_{\text{vol}}(\sigma) \cdot [v(\sigma) - V_t(\sigma)]^2}_{\text{volume constraint}}$$

The first sum, over all pairs of neighboring lattice sites \vec{i} and \vec{j} , calculates the *boundary* or *contact energy* between all pairs of neighboring domains/cells $\sigma_{\vec{i}}$ and $\sigma_{\vec{j}}$.

$J[\tau(\sigma_{\vec{i}}), \tau(\sigma_{\vec{j}})]$ specifies the boundary energy per unit contact area for domains/cells of

types $\tau(\sigma_{\vec{i}})$ and $\tau(\sigma_{\vec{j}})$ occupying sites \vec{i} and \vec{j} , respectively, and the delta function restricts the contact energy contribution to domain-domain interfaces. Neighboring sites within the same domain are assumed to have zero contact energy. We specify J as a matrix indexed by the domain types. Higher (more positive) contact energies between domains/cells result in greater repulsion and lower (more negative) contact energies result in greater adhesion.

The second sum in (Eq. 2.1), over all domains/cells, calculates the effective energies due to a volume constraint. Deviations of the volume ($v(\sigma)$) of domain σ from its target value ($V_i(\sigma)$) increase the effective energy. On average, a domain/cell will occupy a number of sites in the lattice slightly smaller than its target volume due to surface tensions from the contact energies (J). The parameter λ_{vol} behaves as a Young's modulus, with higher values reducing the magnitude of fluctuations of a domain's volume about its target value.

Cell dynamics in the CP/GGH model provide a simplified representation of cytoskeletally-driven cell motility using a stochastic modified Metropolis algorithm consisting of a series of domain-index-copy attempts. Before each attempt, the algorithm randomly selects a target site, \vec{i} , and a neighboring source site \vec{i}' . If different domains occupy those sites the algorithm sets $\sigma_{\vec{i}} = \sigma_{\vec{i}'}$, with probability $P(\sigma_{\vec{i}} \rightarrow \sigma_{\vec{i}'})$, given by the Boltzmann acceptance function:

$$(Eq. 2.2) \quad P(\sigma_{\vec{i}} \rightarrow \sigma_{\vec{i}'}) = \begin{cases} 1 & : \Delta H \leq 0 \\ e^{-\frac{\Delta H}{T_m}} & : \Delta H > 0 \end{cases}$$

where ΔH is the change in the effective energy (Eq. 2.1) if the copy occurs and T_m is a global parameter describing the amplitude of boundary fluctuations.

The average value of the ratio $\Delta H/T_m$ for a given domain determines the amplitude of fluctuations in the domain's boundaries. High $\Delta H/T_m$ results in rigid, barely- or non-motile objects and little domain rearrangement. For low $\Delta H/T_m$, large fluctuations allow a high degree of domain motility and rearrangement. For extremely low $\Delta H/T_m$, domains may fragment in the absence of a constraint strong enough to maintain the integrity of the borders between them. Because $\Delta H/T_m$ is a ratio, we can achieve appropriate domain/cell motilities by varying either T_m or ΔH . Variations in T_m allow us to explore the impact of global changes in boundary fluctuations (*e.g.*, to mimic an experiment using cytochalasin-D, which influences cytoskeletal activity). By changing the H , we can influence the relative motility of the domain types or of individual domain by varying, for example, the parameter λ_{vol} or the contact energies (J) between domains.

The Metropolis algorithm gradually evolves the lattice configuration to simultaneously satisfy the constraints, to the extent to which they are compatible, with perfect damping (*i.e.*, average velocities are proportional to applied forces). A potential domain-index copy that increases the effective energy, *e.g.*, by increasing deviations from target values for domain volume or juxtaposing mutually repulsive domain types is improbable. Thus, the pattern evolves in a manner consistent with the biologically-relevant “guidelines” incorporated in the effective energy: domains/cells maintain volumes close to their target values, mutually adhesive domains/cells (with low cell-cell contact energies)

stick together, mutually repulsive domains/cells separate *etc...* Thus, the average time-evolution of the lattice corresponds to that achieved deterministically using finite-element or center-model methodologies with perfect damping. For a further introduction to CP/GGH modeling, see [12, 14].

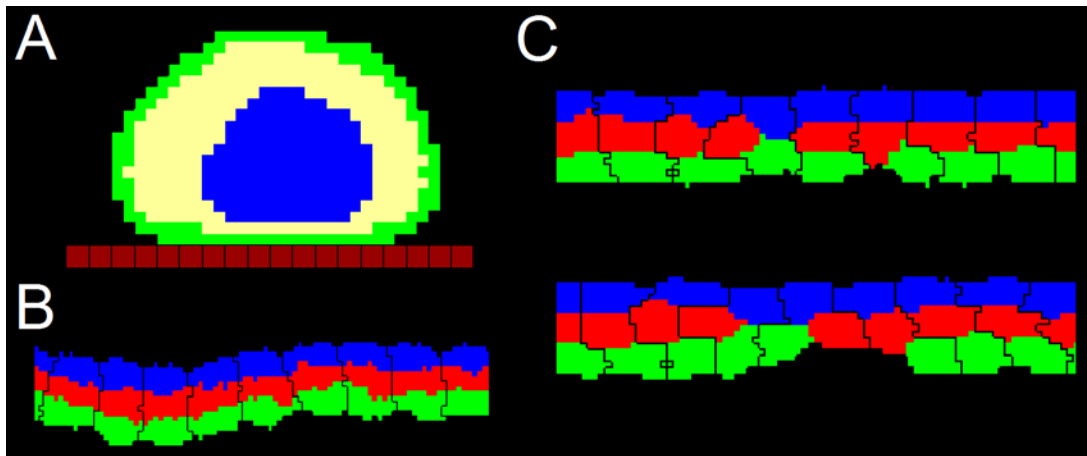


Figure 2.3 – Cell compartments

Use of cell compartments in CP/GGH models to represent (A) real sub-cellular structures: membrane (green), nucleus (blue); and (B) abstract cell regions: here apical (blue), basal (green) and central (red) regions of an epithelial cell. (C) Effect of not choosing proper contact energies for internal compartments.

Here the adhesion energies between internal and external compartments are the same.

Modeling of cell compartments using CPM/GGH

Most CP/GGH models use a single domain to represent an individual cell [16] or groups of cells [17]. A CPM/GGH domain can also represent an internal compartment of a cell, which can correspond to a distinguishable biological sub-cellular unit, like the cell membrane or nucleus [18] (Figure 2.3a), or to a conceptual compartment like the apical/basal sides of an epithelial cell (Figure 2.3b). In compartmentalized-cell models each

modeled biological **cell** is composed of two or more domains (referred from now on as *compartments*) that share a common *cell-index* θ , in addition to a domain-index σ . In this case, each domain/compartment has a unique index pair (θ, σ) .

The use of **cell** compartments requires a distinction in contact energies between domains belonging to the same **cell** versus contact energies between domains belonging to different **cells**. To ensure **cell** integrity, adhesion between internal compartments should generally be stronger than between compartments of different **cells** (Figure 2.3c). These differences require the use of two adhesion matrices (see Table 2.1 and Table 2.2). For internal contacts the adhesion of **cell** compartments with the **Medium** as well as adhesion between compartments of the same type (*e.g.*, **Apical-Apical**) need not to be specified, unless the **cell** contains two, or more, repeated compartments.

Domain Type	Medium	Apical	Central	Basal
Medium	0	10	10	10
Apical	-	5	10	15
Central	-	-	5	10
Basal	-	-	-	5

Table 2.1 – Contact energies between compartments of different **cells** (different *cell-index* θ) used in Figure 2.3b.

Domain Type	Apical	Central	Basal
Apical	-	2	5
Central	-	-	2
Basal	-	-	-

Table 2.2 – Contact energies between compartments of the same **cell** (same *cell-index* θ) used in Figure 2.3b.

The use of biological or conceptual **cell** compartments adds more realism and flexibility to CP/GGH modeling. For example, Scianna *et al.* demonstrated that cell morphology during chemotaxis is better described by the use of a **cell** with two compartments, corresponding to the cytoplasm and nucleus, versus a non-compartmentalized **cell** [18]. Similarly, Starruss *et al.* used a series of elastically linked compartments to model the morphology and dynamics of myxobacteria [19].

For the present purposes, the main advantage of including **cell** compartments in CP/GGH model is the ability to specify different surface properties within a **cell**, which is a characteristic of polarized cells. **Cell** compartments in CP/GGH models can also represent domains that do not localize to the **cell** surface, but have distinct mechanical or biochemical properties, as is done with models of real sub-cellular structures [18] (for example, see Figure 2.3a). Conversion of 2D CP/GGH models into 3D requires only recalculations of parameter values, rather than the postulation of additional rules – a convenience not affected by the use of **cell** compartments.

While the use of **cell** compartments in the CP/GGH model clearly suits the representation of already polarized cells in an epithelial tissue, it is not evident that this mathematical framework is suited to describe the polarization process of the cell, or the behaviors associated with them, such as biased motility, cell intercalation during convergent-extension or the self-ordering of tissues. Modeling of these processes requires additional modifications of the basic CP/GGH model that I will present in the next two chapters. In Chapter 3 I introduce a slight change in the CP/GGH model that supports

modeling of cell polarization and illustrate its use in the context of tissue-level Apico-Basal polarization and planar cell polarity induction across an epithelial tissue. In Chapter 4 I extend the CP/GGH model to include polarized pulling forces between cells and apply it to model convergent-extension.

CHAPTER 3 – CELL POLARITY AND THE *SUBCELLULAR POTTS/GGH* MODEL

The CPM/GGH compartmentalized **cell** concept allows for an easy way to represent polarized cells, especially epithelial cells. However, in its current format, it assumes that the cell is already polarized and stable, *i.e.*, the sizes and relative positions of the **cell** compartments are fixed and the **cells** do not move around too much during the course of the simulation.

Furthermore, the current implementation of cell division of compartmentalized **cells** in CP/GHH does not adequately reflect the complex behavior of polarized cells during division. The CP/GGH model cell division algorithm slices **cells** along a particular plane (usually along the axis of polarization) and replicates the relative positions of the **cell** compartments in each daughter **cell**. In reality, division of an epithelial cell usually involves

the following steps: loss of polarity, detachment from the epithelial layer, rounding up, division, repolarization and reattachment to the layer.

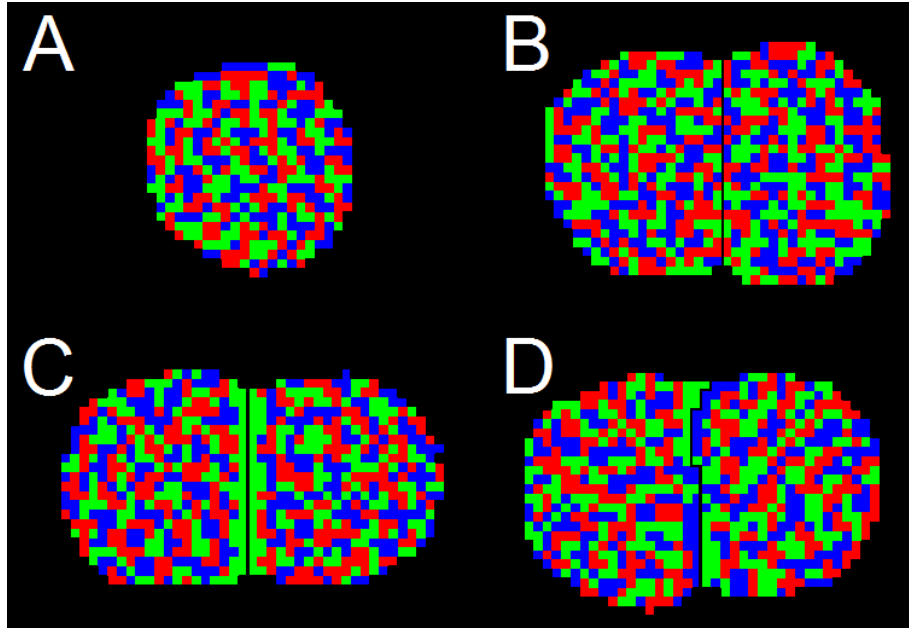


Figure 3.1 – Dynamic domains models

(A) Example of a modeled cell using the dynamic domains technique. All 3 compartments (Blue, Red and Green) coexist inside the cell in a mixed state. (B) Two cells with homogeneous external contact preferences do not sort their compartments upon contact. (C) Two cells with preferred Green-Green external contacts localize part of their Green compartments to the cell-cell surface. (D) Two cells with preferred Green-Blue contacts localize part of their Green and Blue compartments to the cell-cell surface. Note the alternated Green-Blue connections along the membrane.

Dynamic domains model

To properly model cell polarization in the CP/GGH model, the compartment concept must be adapted to the coarse-grained spatial representation of membranes and intracellular molecules rather than sub-cellular units or conceptual domains. Defining domains with positive (repulsive) contact energies between different cells and negative (attractive) contact

energies inside the same **cell** leads the domains within a **cell** to mix instead of segregating spatially (compare Figure 3.1a with Figure 2.3a-b). The distinction between positive and negative contact energies comes from the Potts/GGH formalism, where **domains** (or **cells**) have by default zero contact energy between their sites, due to the delta function on the first term of (Eq. 2.1).

If all **cell** compartments, or domains, have identical internal and external contact energies the **cell** is functionally identical to a non-compartmental **cell**. The method starts to display its usefulness when there is a break of symmetry between contact energies. Figure 3.1a shows a single **cell** composed of three compartments with identical negative internal contact energies, as in Table 3.1. If the domains also have identical external contact energies, then two such **cells** in contact would remain with a mixed internal state (Figure 3.1b). However, if the external contact energies are unequal the two **cells** may segregate some of their compartments upon contact. For example, if a **cell**'s **Green** compartment has low contact energy with an *external* **Green** domain than with external **Blue** and **Red** domains (see Table 3.2), then contact between the two **cells** will lead to accumulation of **Green** domains along the shared surface between the **cells** (Figure 3.1c). This self-segregation resembles that of homophilic adheren molecules like N-Cadherin.

Domain Type	Blue	Red	Green
Blue	-	-5	-5
Red	-	-	-5
Green	-	-	-

Table 3.1 – Internal contact energies between domains of the same cell (same cluster index θ) used for models shown in Figure 3.1.

Domain Type	Medium	Blue	Red	Green
Medium	15	15	15	15
Blue	-	10	10	10
Red	-	-	10	10
Green	-	-	-	2

Table 3.2 – External contact energies between domains of different cells (distinct cluster indexes θ) used in Figure 3.1d.

Such compartments/domains can therefore function as a coarse-grained representation of the spatial distribution of a protein, or set of proteins, that have internal and external contact preferences. For example, the **Green** domains on the last model (Figure 3.1c) can represent two proteins establish cell-cell homophilic adhesive links, like those between N-cadherins. Similarly, heterophilic cell-cell adhesive links, like those between Ephs and ephrins or Delta and Notch, can be represented by a break of symmetry between external contacts of the different domains (**Green** and **Blue** domains in Figure 3.1d).

Membrane restriction

In the examples shown in Figure 3.1 , the modeled species can freely diffuse in both the membrane and the cytoplasm. However, some sets of molecules or complexes remain attached to the membrane, *e.g.* the molecular complexes that define the basolateral and apical surfaces of polarized epithelial cells localize almost exclusively to the cell membrane.

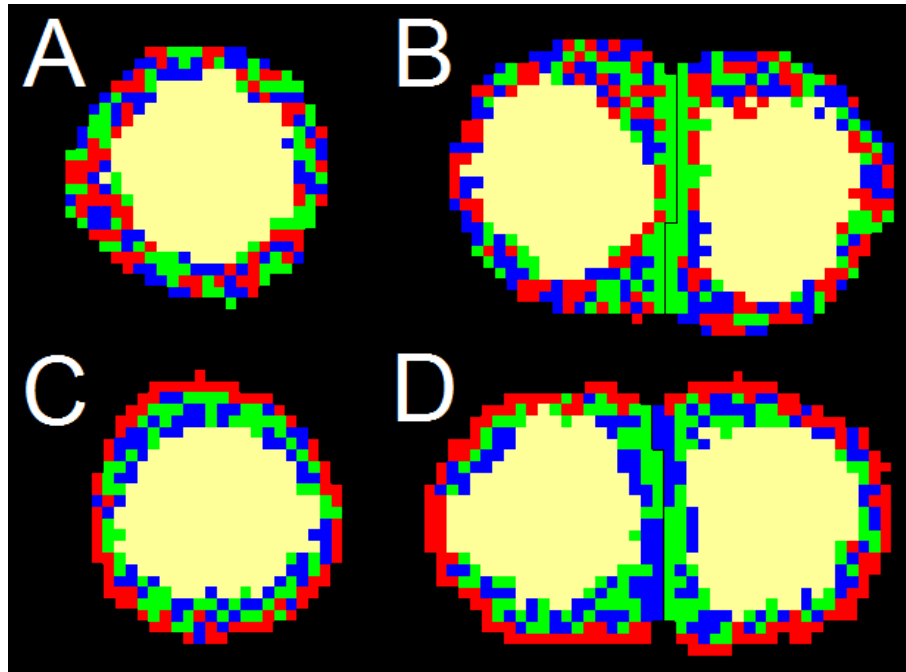


Figure 3.2 – Membrane restriction

(A) Cell compartments can be restricted to regions near the cell surface by addition of an extra compartment that occupies most of the internal volume of the cell. (B) Reproduction of Figure 2.3c. (C) Cell with preferred Red-Medium contact. (D) Simulation that combines features shown in (C) and in Figure 3.1d.

In those cases we can define a cytoplasmic or nuclear domain type that occupies most of the internal volume of the cell and has high contact energy with components of the external environment (be it **Medium** or other **cells**) so that the cell's other compartments stays at, or near the cell membrane (Figure 3.2). Figure 3.2b shows that the extra cytoplasmic domain does not affect the membrane segregation mechanisms shown before (compare to Figure 3.1c).

As before, when using a cytoplasmic or nuclear domain, appropriate choices of cell compartment contact energies can lead to internalization and mixing of domains in isolated cells and segregation to surface domains when the cell comes into contact with the right

environment. Figure 3.2c shows a simulated **cell** where the **Red** domains preferentially contacts the **Medium** and Figure 3.2d shows a simulation of two **cells** in contact with preferential **Blue-Green** external contacts and preferential **Red** and **Medium** external contacts (see Table 3.3 and Table 3.4 for contact energies).

Domain Type	Medium	Nucleus	Blue	Red	Green
Medium	0	30	10	2	10
Nucleus	-	30	30	30	30
Blue	-	-	10	10	2
Red	-	-	-	10	10
Green	-	-	-	-	10

Table 3.3 – External contact energies between domains of different cells shown in Figure 3.2c-d.

Domain Type	Nucleus	Blue	Red	Green
Nucleus	-	0	0	0
Blue	-	-	-5	-5
Red	-	-	-	-5
Green	-	-	-	-

Table 3.4 – Internal contact energies between domains of the same cell used shown in Figure 3.2.

CPM scope and the *sub*Cellular Potts/GGH

While the scope of the original CP/GGH model was cell-to-tissue length scales, the use of **cell** compartments with appropriate contact energies can also represent basic sub-cellular dynamic organization. Compartments are also compatible with two common ways to represent biochemical dynamics in the CP/GGH model.

To describe a specific *Gene-Regulatory Network* (GRN) or a metabolic pathway we can associate to each **cell**, or compartment, a set of *Ordinary Differential Equations* (ODEs)

[2, 20, 21]. Such *Reaction-Kinetics (RK)* models can describe complex molecule interactions in each cell. However, RK models treat their domain of action as a stirred vessel, which may not be appropriate in the complex spatially structuralized volume of the cell. Use of the reactions within a cell compartment can retain some of this spatial organization.

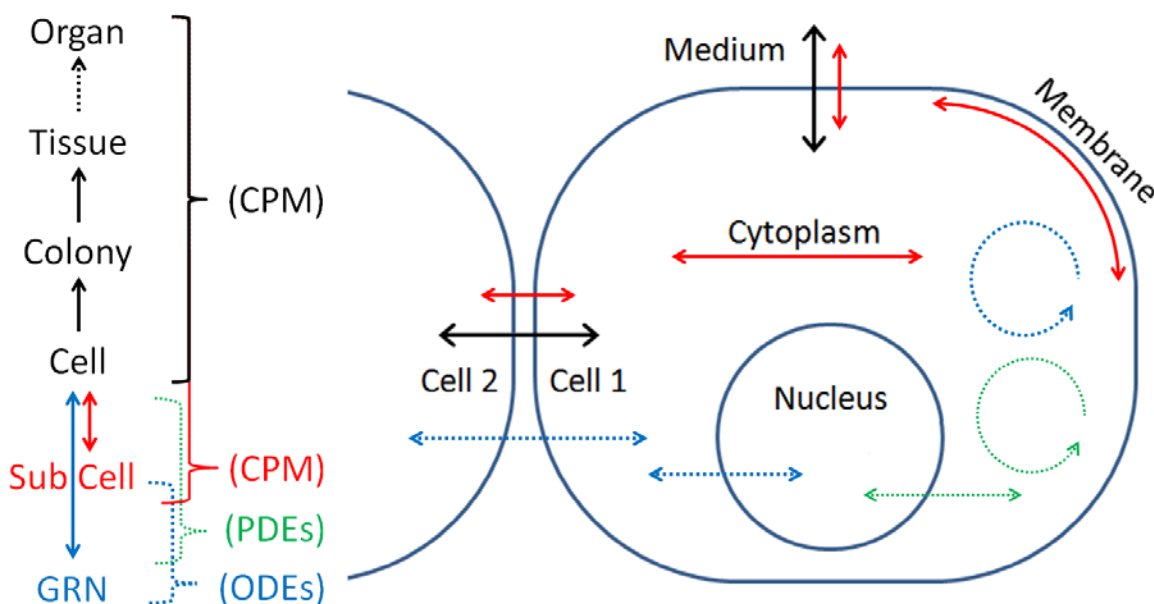


Figure 3.3 – CPM/GGH scope and extensions

Left: spatial scale of interactions/processes for different modeling techniques. Right: interactions within and between cells. The original CP/GGH model describes cell-cell and cell-medium interactions (black arrows) to model organization of cells into tissues. GRN and metabolic reactions, represented as ODEs, describes intra and intercellular molecular interactions (dashed blue arrows) but with only implicit spatial information. PDEs describe spatial distribution of species and their interactions at the sub-cellular and whole tissue scales (dash green arrows). The subCellular Potts/GGH model (red arrows) pursuit modeling of additional subcellular details.

Partial Differential Equations (PDEs) are an established way to represent chemical species outside of cells. Use of *Reaction-Diffusion (RD)* and *Reaction-Diffusion-Advection (RDA)* models inside a cell [22, 23] can describe the spatial complexity within a cell, but

that require the use of much larger lattices (each **cell** must be represented with a higher number of sites) and complicated rules about the reassignment of molecular concentrations as **cell** boundaries advance or retreat.

All this set of techniques offers different ways that sub-cellular processes can be incorporated into CPM, but only the dynamic domains technique is able to do it without any type of hybridization, *i.e.*, without the combination of two different mathematical frameworks. Instead, the use of dynamic **cell** compartments is done within the CPM formalism and requires no additional rules or constraints in the cost function, but only a careful choice of internal and external contact energies. For this reason, I call the dynamic domains method, the *subCellular* Potts/GGH model.

Note that despite the increased presence of domain borders – and, therefore, of eligible *spin flips* (site changes) – the computational cost of this technique is the same as the original one since the bottle neck is the random selection of pair of sites, which is blind to the number of **cells/domains** present in the lattice.

Molecular-Cell Integration (MCI) model

With the help of Dr. Mansoor Raza, of the University of Cambridge, I have developed the *Molecular-Cell Integration (MCI)* model to describe sub-cellular biochemical reactions inside the CP/GGH model. The MCI extends the *subCellular* Potts/GGH model by refining the site update rules to provide a more realistic description of chemical

reactions. When two (or more) sites from different domains (from the same **cell** or not) come into contact they induce, with a given probability, a change in the identity of one or both sites to reflect the formation of a new complex, a reaction or a change of configuration by the molecules at these sites.

The MCI is more expensive computationally than the *sub*Cellular Potts/GGH model, but provide a more detailed representation of the molecular interactions taking place inside and at the interfaces of **cells**. In this sense, this method is similar to the use of PDEs, with the PDEs' diffusion term corresponding to the stochastic dislocation of the domain sites and the PDEs' reaction terms corresponding to the extra site-change rules. Unlike RD models, the MCI handles advection of chemical concentrations by the movement of **cell** boundaries.

Cell polarity models – Apico-basal polarity

The dynamic domains model can model the two main types of cell polarity: Apico-Basal polarity and *Planar Cell Polarity (PCP)* (see Figure 1.1). In both cases I will use a cytoplasmic domain to restrict the polarity domains to the near-membrane regions, so the **cells** will have the **Cytoplasm** (or **Cyto**), and three surface domains.

To model Apico-Basal polarity I defined **cells** composed of **Basal**, **Lateral** and **Apical** surface compartments and one core compartment (**Cyto**) and two types of external domains: **Lumen** and **Medium** (representing the difference in extra cellular matrix across

an epithelium). I specify internal domain contact energies so that the 3 surface domains tend to mix within an isolated cell, with a slight repulsion between **Apical** and **Basal** compartments (Table 3.5). The external contact energies favor **Lateral-Lateral**, **Basal-Medium** and **Apical-Lumen** contacts over heterotopic contacts. I also define strong repulsive external contact energies between **Apical** and any cell compartment type that is not **Apical** or **Lumen** (Table 3.6).

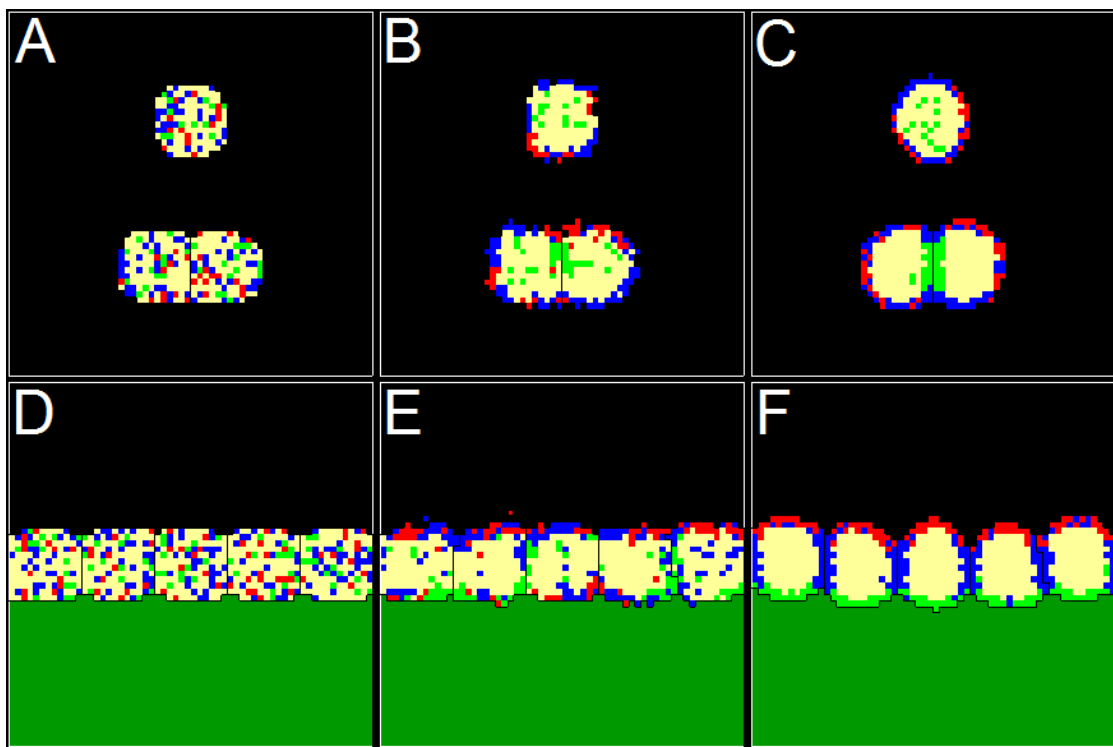


Figure 3.4 - Apico-Basal polarity model

*The surface compartments are initially randomly distributed inside cells (A,D) and self-organize in response to their environment. Panels (A-C) show an isolated unpolarized cell (top) and a pair of polarized cells (bottom). In both cases, the **Lateral** and **Basal** domains localize to cell-Medium interfaces, while the **Apical** domains co-localize to the cell-cell interface (bottom) or remain inside the isolated cell (top). (D-E) Cells in an epithelial layer with **Medium** above and **Lumen** below segregate and localize their compartments according to their contact preferences: **Basal-Medium**, **Lateral-Lateral** and **Apical-Lumen**.*

From random initial compartment site distribution, this set of contact preferences leads to localization of **Apical**, **Basal** and **Lateral** domains to their correct locations in each cell in the **epithelial layer** (see Figure 3.4d-f). The **cells'** ability to self-organize polarized surface compartments provides a convenient way to model epithelial layers in 2D and 3D.

Domain Type	Cyto	Apical	Basal	Lateral
Cyto	-	0	0	0
Apical	-	-	-5	-5
Basal	-	-	-	-5
Lateral	-	-	-	-

Table 3.5 – Internal contact energies between domains of the same cell used on Figure 3.4.

Domain Type	Medium	Lumen	Cyto	Apical	Basal	Lateral
Medium	0	60	60	60	3	8
Lumen		0	60	15	20	20
Cyto	-	-	60	60	60	60
Apical	-	-	-	15	20	20
Basal	-	-	-	-	15	20
Lateral	-	-	-	-	-	5

Table 3.6 – External contact energies between domains of different cells used on Figure 3.4.

Cell polarity models – PCP

To model PCP, I define **cells** with a cytoplasmic compartment (**Cyto**) and **Proximal**, **Distal** and **Lateral** surface compartment. The **Proximal** domain corresponds to cell regions containing the Flamingo-VanGogh-Prickle protein complex and the **Distal** domain corresponds to cell regions containing the Flamingo-Frizzled-Diego-Dishevelled complex. These complexes segregate to opposite lateral sides of planar polarized cells and co-localize across intercellular surfaces.

During embryonic development, large-scale morphogen gradients might determine the orientation of these PCP complexes within each cell, with a secondary mechanism refining the alignment between neighboring cells. However, the identities of these global morphogens are unknown and the main mechanisms behind PCP are still subjects of investigation.

Domain Type	Cyto	Proximal	Distal	Lateral
Cyto	-	0	0	0
Proximal	-	-	10	0
Distal	-	-	-	0
Lateral	-	-	-	-

Table 3.7 – Internal contact energies between domains of the same cell used on Figure 3.4.

Domain Type	Medium	Cyto	Proximal	Distal	Lateral
Medium	0	40	10	8	10
Cyto		40	40	40	40
Proximal	-	-	12	3	10
Distal	-	-	-	12	10
Lateral	-	-	-	-	10

Table 3.8 – External contact energies between domains of different cells used on Figure 3.4.

To model the intercellular PCP mechanism I set the internal contact energies so that the 3 surface compartments (**Proximal**, **Distal** and **Lateral**) tend to mix within an isolated cell, with a slight repulsion between **Proximal** and **Distal** compartments (Table 3.7), and set the external contact energies to favor **Proximal-Distal** and **Lateral-Lateral** contacts (Table 3.8). In a simple simulation of this *polar PCP model*, I defined a 2D periodic-boundary lattice filled with cells, and, as in the Apico-Basal model (Figure 3.4), randomly distributed the compartment sites inside each cell (Figure 3.5a). To check whenever the

cells can polarize properly and how the polarization of the tissue as a whole depends on the lattice size, I define a *polarization vector* for each **cell** as the vector from the **Distal** to the **Proximal** compartment:

$$(Eq. 3.1) \quad \vec{v}(\theta) \equiv \frac{\bar{x}(\sigma_{\text{Proximal}}) - \bar{x}(\sigma_{\text{Distal}})}{|\bar{x}(\sigma_{\text{Proximal}}) - \bar{x}(\sigma_{\text{Distal}})|}.$$

I then define a global **tissue alignment** to be:

$$(Eq. 3.2) \quad \phi \equiv \frac{1}{N} \left| \sum_{\theta} \vec{v}(\theta) \right| = \begin{cases} 0 & \text{random alignment} \\ 1 & \text{global alignment} \end{cases}.$$

Figure 3.5a-d shows snapshots of the dynamics of the polar PCP model for a **tissue** with 36 **cells**. Initially the domains are randomly distributed and the polarization vectors are misaligned (Figure 3.5a'). The **cells** gradually develop PCP and their polarization vectors align (Figure 3.5d-d'). For a single set of parameters, not all replicas reach global alignment of their polarization vectors, and the percentage of replicas reaching a single global tissue alignment decreases as the square root of the number of **cells** in the **tissue** (Figure 3.5e).

For the set of parameters used (Table 3.7 and Table 3.8), the previous results show the existence of an upper limit on the number of **cells** after which global polarization becomes almost impossible (around 600 **cells**). To test how the **tissue** PCP develops in the presence of a boundary signal that biases global **tissue** PCP alignment in a certain direction, I constructed a lattice with periodic boundary conditions containing a vertical column of 10 **cell** diameters with the same external contact properties as the **Proximal** domain (Figure

3.6a). The number of **cells** (or columns of **cells**) to the right of the boundary was varied to check at which point global **tissue** PCP polarization fails.

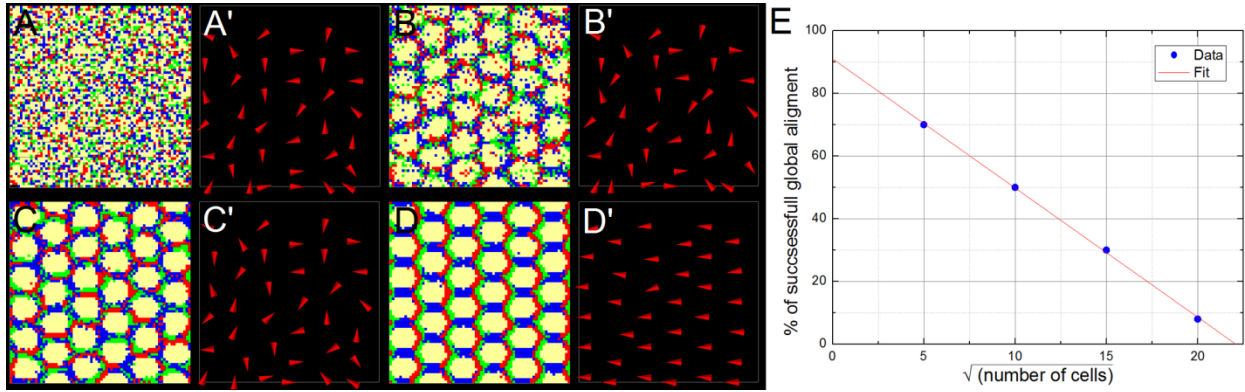


Figure 3.5 – Polar PCP model results

*Panels (A-D) show the dynamics of the domain segregation and localization in a **tissue** of 36 **cells** with periodic-boundary conditions. Panels (A'-D') show the corresponding polarization vectors for each **cell**. (E) The percentage of **tissues** reaching a global alignment decreases as the square root of the number of **cells**.*

Proximal domains in green, Distal domains in red and Lateral domains in blue.

In the presence of a boundary inducing PCP, the successful rate of global **tissue** PCP alignment do not depend on the number of columns/**cells**, with 80% of replicas reaching a single global **tissue** alignment. However, the time taken for the **tissue** to reach global alignment, defined as the time it takes for φ to be equal or higher than 0.995, increases exponentially with the number of columns/**cells** (Figure 3.6c).

Extensions of cell polarity models

The PCP model could be further explored to check another theory proposed by Gary Struhl where the main PCP mechanism lies in the Fat-Dachsous pathway and works by a cascade of intercellular domain activation, that is, cells become polarized only after being in

contact with another polarized cell [24, 25]. My preliminary models of this mechanism (called feed-forward PCP) proved successful but a full exploration of that will be left for the future.

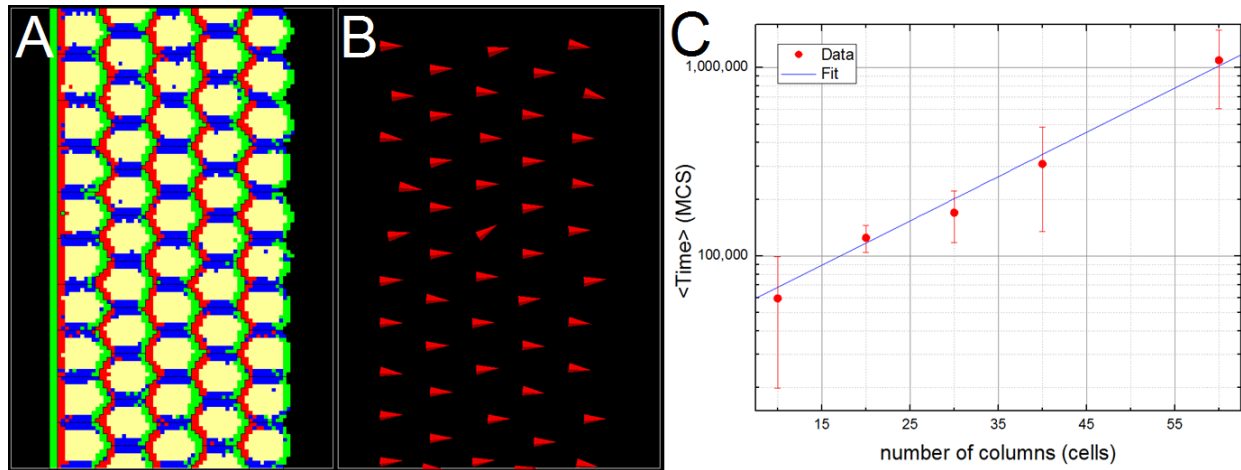


Figure 3.6 - Boundary PCP model

Panels (A-B) show a simulated tissue with a inducing stripe to the left (green) and 10 × 5 cells after global PCP alignment has reached $\varphi=0.995$. (C) The average time for the tissue to reach global alignment ($\varphi>0.995$) increases exponentially with the number of cells in the tissue.

In Chapter 6 I apply the Apico-Basal polarization model to construct a stable cylindrical epithelial **tissue** segment to represent a renal tubule segment as the basis of a cyst-formation model. And in Chapter 7 I use the self-organizing Apico-Basal polarization model to explain how epithelial balls (or somites) can self-assemble without internal and external spatial cues.

CHAPTER 4 – CONVERGENT-EXTENSION

In the previous chapter I extended the CP/GGH model to replicate symmetry breaking and self-organization processes within cells during Apico-Basal and planar polarization. Those features, however, are somehow limited as they only reorganize the **cell** internal properties without necessarily leading to morphological changes in tissue architecture. In this chapter I extend the CP/GGH model to include pulling forces between cells which leads to the tissue-scale cell rearrangements observed in many developmental processes.

Pulling forces

Large-scale changes of tissue shape, such as gastrulation, limb formation and eye development, usually require substantial cell rearrangement. To rearrange, cells must exert

anisotropic forces on their surrounding environment, whether *extra cellular matrix* (ECM) or other cells. The main source of such forces is the interaction of the actin cytoskeleton with the motor myosin II. Because actin can organize in many ways within a cell, the pattern of force generation differs between cells. However, two types of contractile forces are particularly significant. Many cells stochastically extend long, narrow filopodia, which contain a narrow crosslinked actin core and a variety of motor proteins. Filopodia are typically only 0.1-0.3 μm in diameter, but can be several hundred microns long. Their tips contain adhesion molecules which can bind strongly to an appropriate transmembrane cellular domain or ECM target ligand. Both the filopodia and the target transmembrane cellular domain bind strongly to a cell's actin cortex, effectively transmitting the force of the filopodium to a substantial volume of the cell. Unbound filopodia rapidly retract into the cell. Bound filopodia exert a *linear tension* force on their targets, roughly independent of the length of the filopodia, leading either to their gradual shortening as the source and target are pulled together, or to detachment of the filopodium from the target. Epithelial cells, and migrating mesenchymal cells on a substrate can also form junctional adhesions with other cells and with ECM. These junctional adhesions connect to one or more bands of actin within the cytoplasm (*e.g.* in a cortical actin ring or a star of stress fibers). These actin bands can, in turn, associate with myosin II or other motors to generate contractile forces within the cell, leading to areal contraction of one or more of the cell's surfaces.

To model such forces, I extend the CP/GGH model with oriented traction forces. The right two terms in (Eq. 4.1) show two ways of representing such forces mathematically in the governing cell-behavior cost function:

$$(Eq. 4.1) \quad H = H_0 + \sum_{\substack{\vec{i}, \vec{j} \\ \text{neighbors}}} \lambda_{\text{force1}}(\sigma_{\vec{i}}) \vec{v}(\sigma_{\vec{i}}) \cdot (\vec{j} - \vec{i}) + \sum_{\sigma, \sigma'} \lambda_{\text{force2}}(\sigma, \sigma') (l_{\sigma, \sigma'} - L_{\sigma, \sigma'})^h,$$

where the term, H_0 , aggregates all the other cost-function terms.

The first option is to apply an external force to a **cell** (or **domain**) **boundary**, which biases all lattice-site copies involving it to favor movements of its boundary in a given direction. The middle term in (Eq. 4.1) implements such a force, where $\lambda_{\text{force1}}(\sigma_{\vec{i}})$ is the strength of the bias for **cell** $\sigma_{\vec{i}}$, \vec{i} is the source site, \vec{j} is the target site and $\vec{v}(\sigma_{\vec{i}})$ is the preferred direction of movement. If the **cell** or **domain** is pulling, or being pulled, in more than one direction or by multiple forces at once, the parameters can reflect the net pulling/pushing force on the cell or **domain**, or I can add a separate term for each force.

A second option is to apply a force which acts on **cell** or **domain centers**. The rightmost, third term in (Eq. 4.1), implements such a force, where $\lambda_{\text{force2}}(\sigma, \sigma')$ is the strength of the force between **cells** or **domains** σ and σ' , $l_{\sigma, \sigma'}$ is the actual distance between **cells** or **domains** σ and σ' , $L_{\sigma, \sigma'}$ is the target, or resting distance between them and h is a Hill exponent which is 2 for elastic spring-like connections like adhesion junctions and 1 for constant-force connections like filopodia. To emphasize the center-to-center linear nature of the terms in the sum, I will call them **links**.

While many different biological mechanism could generate forces of this type, a simple version of a **link** can conveniently represent the contractile force that a cell generates when it extends and attaches a filopodium to another cell. I will use this option in the CP/GGH model to model filopodial pulling forces which generate cell rearrangement during development. As usual, I may extend both the strength of the force, $\lambda_{\text{force2}}(\sigma, \sigma')$, and the resting distance of the link, $L_{\sigma, \sigma'}$, to be time dependent to model plastic materials and may employ more complex strain-rate-dependent forms to represent viscous forces.

Other uses of links in the CP/GGH model

Researchers have employed length, or distance, constraints between **cells** or **domains** in the CP/GGH model to model the rigidity of bacteria [19] and junctional adhesion between cells [26, 27]. However, both applications used such **links** to maintain the mechanical integrity of modeled **cells** or **tissues** rather than to implement active cell-generated forces. For the **links** to produce active forces driving significant cell rearrangement, the number, orientation and location of the **links** and their parameters (λ_{force} and L) must depend, explicitly or implicitly, on time and space.

As an application of the link-based contractile-force approach, consider a model of epithelial invagination and pinch off during early development of the eye placode by my colleague, Dr. Abbas Shirinifard. In this developmental mechanism, localized expression of Pax6 induces apical contraction in cells in a limited spatial region of an initially planar

epithelial sheet generates a local invagination which eventually pinches off to form a spherical vesicle [28].

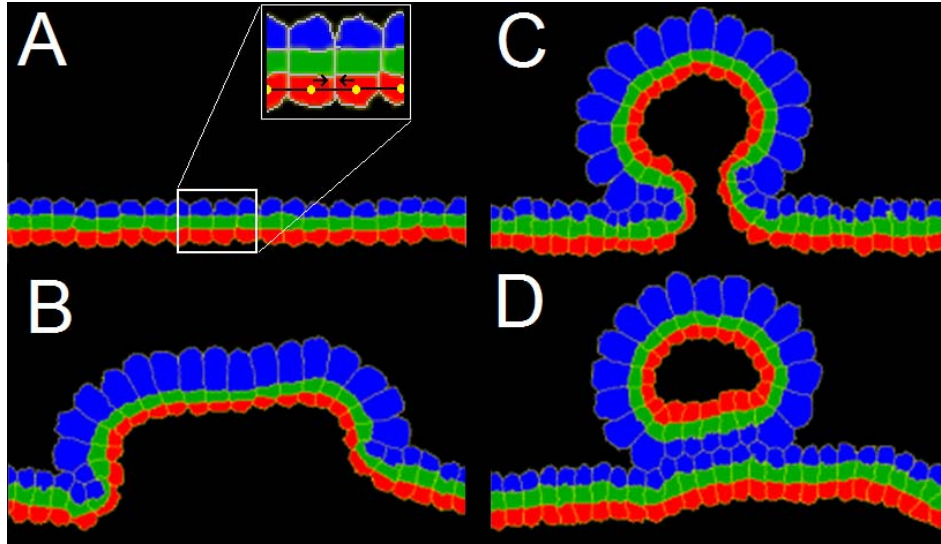


Figure 4.1 – Use of dynamic length constraints

*(A-D) Time series showing formation of an optic vesicle from an epithelial sheet through changes in the target length between **apical-apical** and **basal-basal** domains. (A) Inset: zoom showing apical constriction modeled as a force between adjacent apical compartments.*

Dr. Shirinifard used the CP/GGH **cell** compartment technique to represent a transverse section through an epithelial layer similar to the one shown in Figure 2.3. Each cell consisted of 3 compartments with cross **links** formed between pairs of compartments of the same type in neighboring **cells**, with the **link**'s initial target lengths set to the actual distance between the centers of the compartments (stress-free). He then selected a contiguous group of **cells** to represent the region experiencing apical contraction and gradually reduced their inter-**apical** target lengths, while increasing their inter-**basal** target lengths. The model includes cell division to maintain the net tension in the epithelium at a reasonable level and adjusts the volumes of domains to be compatible with the lengths of

their links. The resulting differential stress between the apical and basal layers of the epithelium drove invagination of a circular epithelial structure, which then pinched off to form a roughly spherical vesicle (Figure 4.1A-D), as in the developing eye placode.

The purpose of this chapter

This chapter focuses on modeling the traction between cells as a result of their planar polarization. While the previous chapter presented methods to model the development of cell polarization, in this chapter I will *assume* that cells are polarized and extend links in an anisotropic fashion, then model the resulting anisotropic tension forces and their effects on tissue morphodynamics.

Cell polarization could modulate traction between **cells** in many ways, both biologically and mathematically. Here, instead, I create **cell-cell** links with alignments around the axis (or plane) perpendicular to the **cell's** polarity vector. If a group of **cells'** polarity vectors are aligned, the resulting forces will cause the cells to intercalate and the tissue to contract along the preferred axis/axes and extend perpendicular to the axis/axes in *convergent-extension* (CE).

Convergent-extension

CE is an important morphological movement in the development of most multicellular organisms, during which cells rearrange their positions and shapes inside a

tissue, usually a epithelial monolayer sheet, so that the tissue narrows (converges) along one axis while it lengthens (extends) along the perpendicular axis (Figure 4.3A). Such CE restricted to a plane, is known as *medio-lateral intercalation* (I discuss 3D CE below). CE of a tissue can be either *active* or *passive*. In passive CE, the tissue deforms in response to an external force, while in active CE, the tissue elongates autonomously, without, or even in opposition to, external deforming forces, with cells continuously rearranging their relative positions (*cell intercalation*).

Two different cellular mechanisms may generate active CE. Spatial differences in cortical tension/contractility *within cells* can lead to intercalation and convergent extension, as during *Drosophila* germ-band extension. Anisotropic traction forces *between cells* can also lead to intercalation and convergent extension, as during *Xenopus* notochord formation, where cells extend contractile filopodia preferentially along the converging axis of the tissue.

Theoretical and mathematical models of CE have hypothesized mechanisms including anisotropic cell-edge/actin contraction [29, 30], anisotropic cell adhesion and elongation [31, 32], cell shape extension/retraction [29] and combinations of a constraining boundary with cell elongation [33] and contractile edges [34]. Most of those models, however, only work on 2D surfaces and either assume a globally-imposed bias or neglect the individual stochastic nature of the cell movements during CE.

None of these models specifically represents the increased filopodial activity perpendicular to the extending axis, which may be the main source of traction between cells

or between cells and the ECM [35]. Using dynamic links I can test whether observed patterns of filopodial activity suffice to drive CE.

In the following sections I develop a cell intercalation model in based on filopodial extension and retraction and explore its features. In Chapter 5 I use a 3D version of the cell intercalation model to model the development of the chicken limb bud.

Filopodial tension model

Based on the experimental observation of long oriented filopodia being continuously generated and retracted primarily along the direction of contraction during CE, I model cells which extend and retract links over a range of angles around a defined axis. These links generate a tension force between the cells they connect [35-37]. I then test whether this tension force is sufficient to explain observed local cell intercalation and global tissue CE.

In the filopodial tension model (Figure 4.2) **cells** form and eliminate links representing filopodia with a defined set of neighboring **cells**. Each **cell** carries a polarization vector (Figure 4.2, red arrow) that defines its preferred plane of filopodial protusion (Figure 4.2, blue horizontal line). The **cell** is competent to interact with all **cells** whose centers of mass lie within a distance r_{\max} from its center of mass and within a given angle θ_{\max} of its polarization plane (Figure 4.2, blue line). The **cell** attempts to link to at most n_{\max} randomly selected **cells** in this pool of **cells**. The actual number of links will depend on the size of this pool and whether the neighboring **cells** have less than n_{\max}

formed links. Each link then exerts a contractile force along the line connecting the cell centers of magnitude λ_{force} . To model the finite lifetimes of filopodia and their attachment to targets, after a relaxation time interval, t_{interval} I discard all current links create new ones based on the current neighborhood of the cell. If the links do not disappear the cells only rearrange a few microns (lattice sites) from their original locations and the tissue fails to converge/extend (see Figure 4.5a).

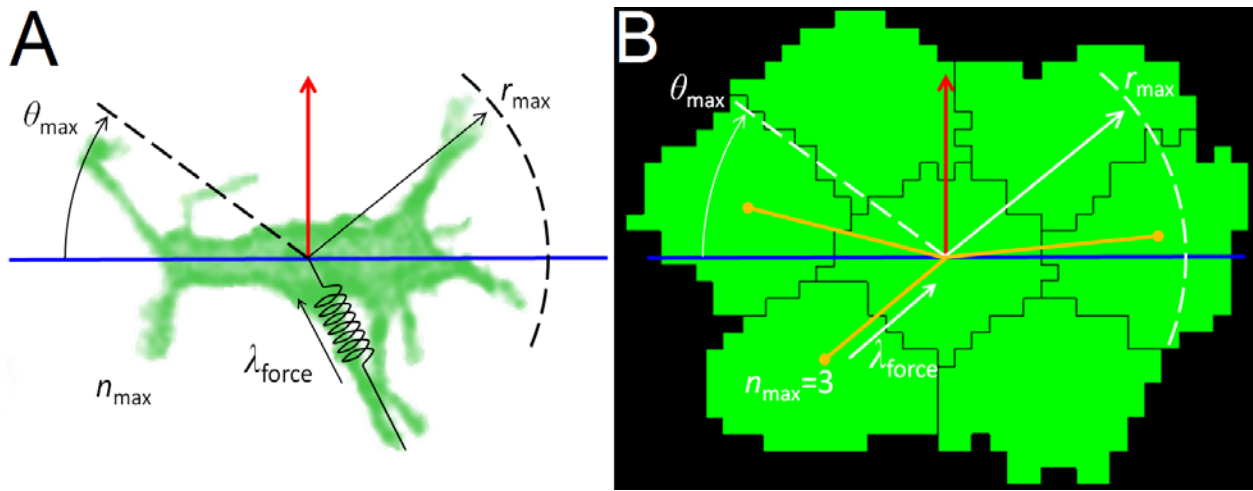


Figure 4.2 – Force-driven cell intercalation model

(A,B) Given an polarization vector (red), the cell pulls with some force λ_{force} a given set of neighboring cells (up to n_{max} cells) that lies inside a fixed interaction range r_{max} and within a critical angle θ_{max} (measured from the convergence plane/axis, shown in blue). (A) Image of a bipolar cell in the chicken limb bud mesenchyme overlayed with the model parameters. (B) Snapshot of a computer simulation overlayed with the model parameters. Dark yellow lines represent simulated filopodial interactions.

The pulling force between connected cells is modeled as a constant force between their center of masses. In the energy cost function, this has the following mathematical form:

$$(Eq. 4.2) \quad H = H_0 + \sum_{\sigma, \sigma'} \lambda_{\text{force}}(\sigma, \sigma')(l_{\sigma, \sigma'} - L_t),$$

where the sum is over all pairs of linked **cells**, λ_{force} is the strength of the pulling force between **cells** σ and σ' , $L_{\sigma,\sigma'}$ is the current distance between the **cells**, L_t is the resting distance between them, and the term H_0 aggregates all the other cost function terms.

The proposed model adds five core/intensive parameters and one spatial/extensive parameter to the CP/GGH model formalism (see Chapter 2), thus making a complete sensitivity analysis computationally costly. I therefore fixed all parameters to values that gave a biological plausible convergent-extension and studied the effects of varying individual parameters (the five core parameters of the intercalation model and the number and diameter of **cells**). The reference parameter values for the simulations can be found on Table 4.1.

Type of parameter	Cell intercalation model					Spatial	Cellular Potts/GGH model						
Parameter	λ_{force}	t_{interval}	r_{max}	n_{max}	θ_{max}	N	cd	L_t	T	λ_{volume}	n_{orders}	$J_{c,M}$	$J_{c,c}$
2D	50	20	2	3	$\pi/4$	109	10	cd/2	50	5	2, 4	10	10
3D	500	50	2	3	$\pi/4$	552	6	cd/2	80	5	2, 5	10	10

Table 4.1 – List of reference parameters values used in the simulations

Parameter sweeps vary one of the first 7 parameters while keeping all the others constant. Key: λ_{force} pulling strength; t_{interval} time interval between link formation/breakage (MCS); r_{max} maximum distance between **cells** (cell diameters); n_{max} maximum number of links per **cell**; θ_{max} maximum angle (radians); N , number of **cells**; cd , cell diameter (lattice sites); L_t target distance between pulling **cells**; T , temperature or level of noise in the simulations; λ_{volume} cell stiffness; n_{orders} neighboring orders for lattice site flip and contact energy; $J_{c,M}$ adhesion energy between **cells** and **medium**; $J_{c,c}$ adhesion energy between **cells**.

Metrics

All simulations start with a mass of identical **cells**, with the same direction of polarization vector and uniformly distributed inside a rough circle. To quantify the degree of tissue deformation I calculated the *inverse aspect ratio* between the length of the minor (L_-) and major (L_+) axes of the **tissue** (Figure 4.3b, green line). Initially the aspect ratio is close to 1 and decreases in time to a final value (κ , Figure 4.3b, dashed red line) that depends on the filopodial tension parameters, the number of **cells** and the surface tension of the **tissue** (defined below).

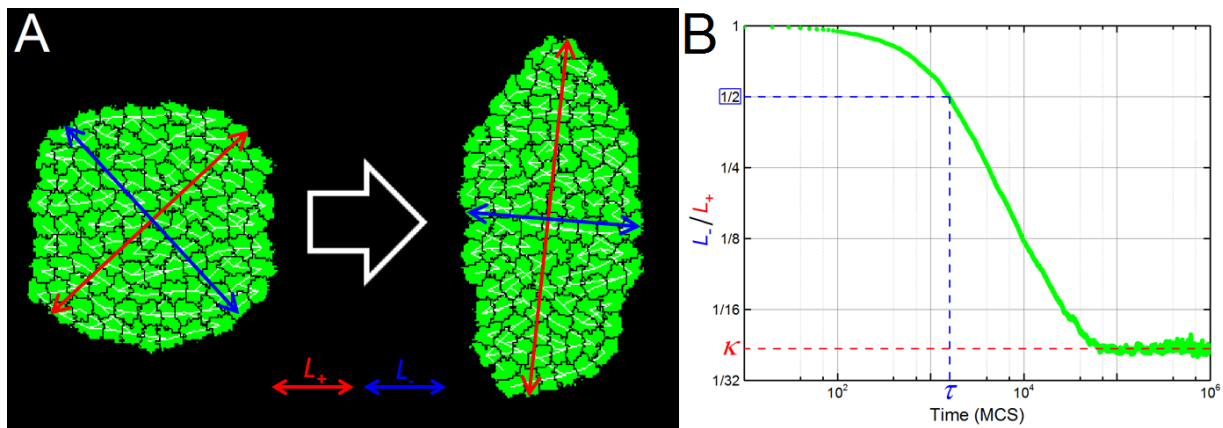


Figure 4.3 – *Simulation snapshots and measured metrics*

(A) Snapshots of the reference 2D simulation showing the beginning (left) and a later point in time when the length of the **tissue** major axis (L_+ , red lines) doubles the length of the minor axis (L_- , blue lines). The simulation contains 109 **cells** (in green) and the pulling forces are shown by the white segments connecting them. (B) Graph of L_-/L_+ versus time for the reference 2D simulation.

The final inverse aspect ratio quantifies the maximum degree of elongation/deformation of the **tissue**, but does not convey how fast the tissue elongates. To quantify the elongation rate, I define the *elongation time* (τ) as the time it takes for the length of the **tissue** major axis (L_+) to double the length of its minor axis (L_-), which is

equivalent to the time when the inverse aspect ratio first decreases to 0.5 (Figure 4.3b, dashed blue lines). I consider CE to fail if the **tissue** never reaches 0.5.

Surface tension

For weak filopodial forces ($\lambda_{\text{force}} < 0.1$), **cells** do not intercalate and the **tissue** fails to converge-extend. As the force applied between each **cell** increases, the time taken for the length of the major axis of the **tissue** to reach twice the length of its minor axis (τ) decreases with a power law ($\tau \propto \lambda_{\text{force}}^{-1.25 \pm 0.03}$) (Figure 4.4a, red line). The final elongation ratio (κ) decreases monotonically with increasing λ_{force} . The $\kappa \times \lambda_{\text{force}}$ curve is sigmoidal on a log-log scale (Figure 4.4b), because the **tissue** is relatively insensitive to weak pulling forces and because the total number of **cells** sets a maximum inverse aspect ratio for the **tissue** (see Figure 4.6a).

Around the inflection point of the curve, $\kappa \times \lambda_{\text{force}}$ is approximately a power law ($\kappa \propto \lambda_{\text{force}}^{-1.51 \pm 0.08}$), where the tension forces of the links (λ_{force}) balances the external forces that oppose **tissue** deformation. Here, the opposing force comes from the superficial tension (γ) between the **cells** and the external **medium**, defined as [12]:

$$(Eq. 4.3) \quad \gamma = J_{c,M} - \frac{J_{c,c}}{2},$$

where $J_{c,c}$ is the contact energy between **cells**, and $J_{c,M}$ is the contact energy between **cells** and **medium** (see Eq. 2.1).

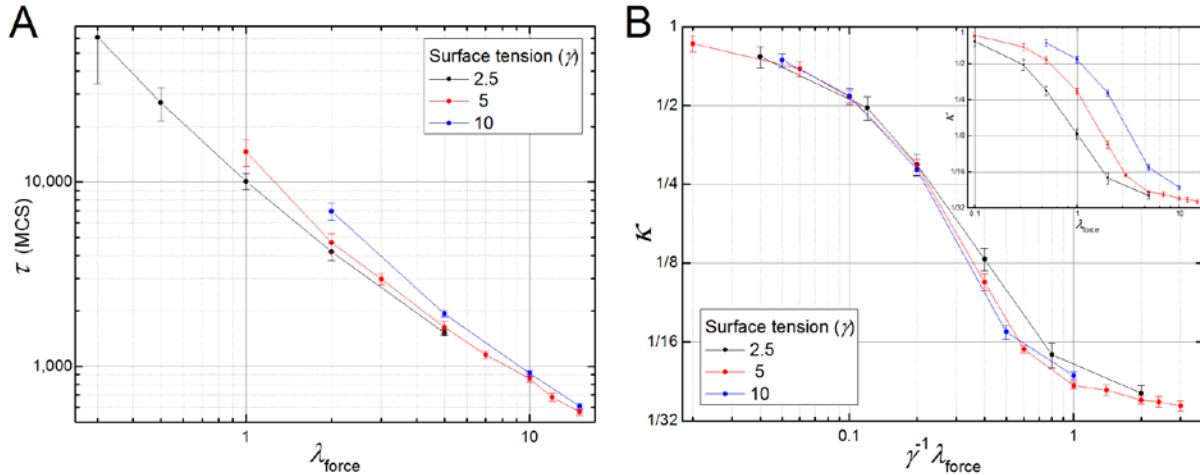


Figure 4.4 – Effects of force and surface tension on the 2D intercalation model

(A) Time (τ) it takes for the length of major axis of the **tissue** to double the length of the minor axis as a function of the pulling force (λ_{force}) of the **cells** for different surface tensions. (B) Insert: Degree of **tissue** deformation (κ) as a function of λ_{force} . An increase in the surface tension of the **tissue** reduces the final degree of convergent-extension leading to the right shift of the $\kappa \times \lambda_{\text{force}}$ curve. The opposite effect happens when the surface tension is decreased. Main: The curves collapse when the pulling force is rescaled with the inverse of the surface tension ($\lambda_{\text{force}}/\gamma$).

For small values of λ_{force} the surface tension forces dominates and the **cells** generate little **tissue** deformation. For higher λ_{force} , the **cells** are able to induce larger **tissue** deformations and at a faster rate (Figure 4.4a). Changing the surface tension of the **tissue** shifts the $\kappa \times \lambda_{\text{force}}$ curve to the right(left) as expected (Figure 4.4b, insert). Normalizing the intercalation forces by the surface tension ($\lambda_{\text{force}}/\gamma$) collapses the curves (Figure 4.4b), showing the linear relationship between λ_{force} and γ . While γ affects the maximal extension (κ), it has little effects on the rate of **cell** intercalation, as measured by τ , which remains relatively unchanged for different surface tensions (Figure 4.4a).

Parameter sensitivity analysis

Next I studied how other filopodial tension parameters affect CE in the model: the mean lifetime of the filopodia, modeled as the time interval between **link** formation and breakage (t_{interval}); the maximum extension of the filopodia, modeled as the maximum distance of interaction between the **cells'** center of mass (r_{max}); the maximum number of filopodia interactions per **cell** (n_{max}); and the maximum angle between filopodial direction and the **cells'** convergence axis (θ_{max}).

Figure 4.5a shows that the lifetime of filopodia, t_{interval} , has no effect on time or final inverse aspect ratio of the **tissue** for values lower than $t_{\text{interval}} \lesssim 200$ MCS. This value corresponds to the typical time of 200 MCS the **cells** require to rearrange their positions in response to a given set of **links** with their **neighbors**. Increasing filopodial lifetimes above 200 MCS slows **cell** intercalation (increasing the elongation time) and increases the **tissue's** final inverse aspect ratio (corresponding to less deformation).

The maximum range (r_{max}) of filopodia interaction has different effects on the final inverse aspect ratio and elongation time. κ first decreases as a power law ($\kappa \propto r_{\text{max}}^{-3.5 \pm 0.2}$), then saturates when r_{max} equals 2 **cell** diameters, while the elongation time always decreases with increasing r_{max} (Figure 4.5b). The same effect is seen with respect to the maximum number of links (n_{max}): κ decreases as a power law ($\kappa \propto n_{\text{max}}^{-1.5 \pm 0.03}$) and saturates when $n_{\text{max}} = 4$, (which is the typical number of **cells** in range for $r_{\text{max}} = 2$ and $\theta_{\text{max}} = 45^\circ$) while τ decreases monotonically with increasing n_{max} (Figure 4.5c). Thus r_{max} and n_{max} have stronger

effect on the rate of **cell** intercalation than on the final inverse aspect ratio, while the surface tension with the external **medium** affects only the final inverse aspect ratio and not the rate of **cell** intercalation (Figure 4.4).

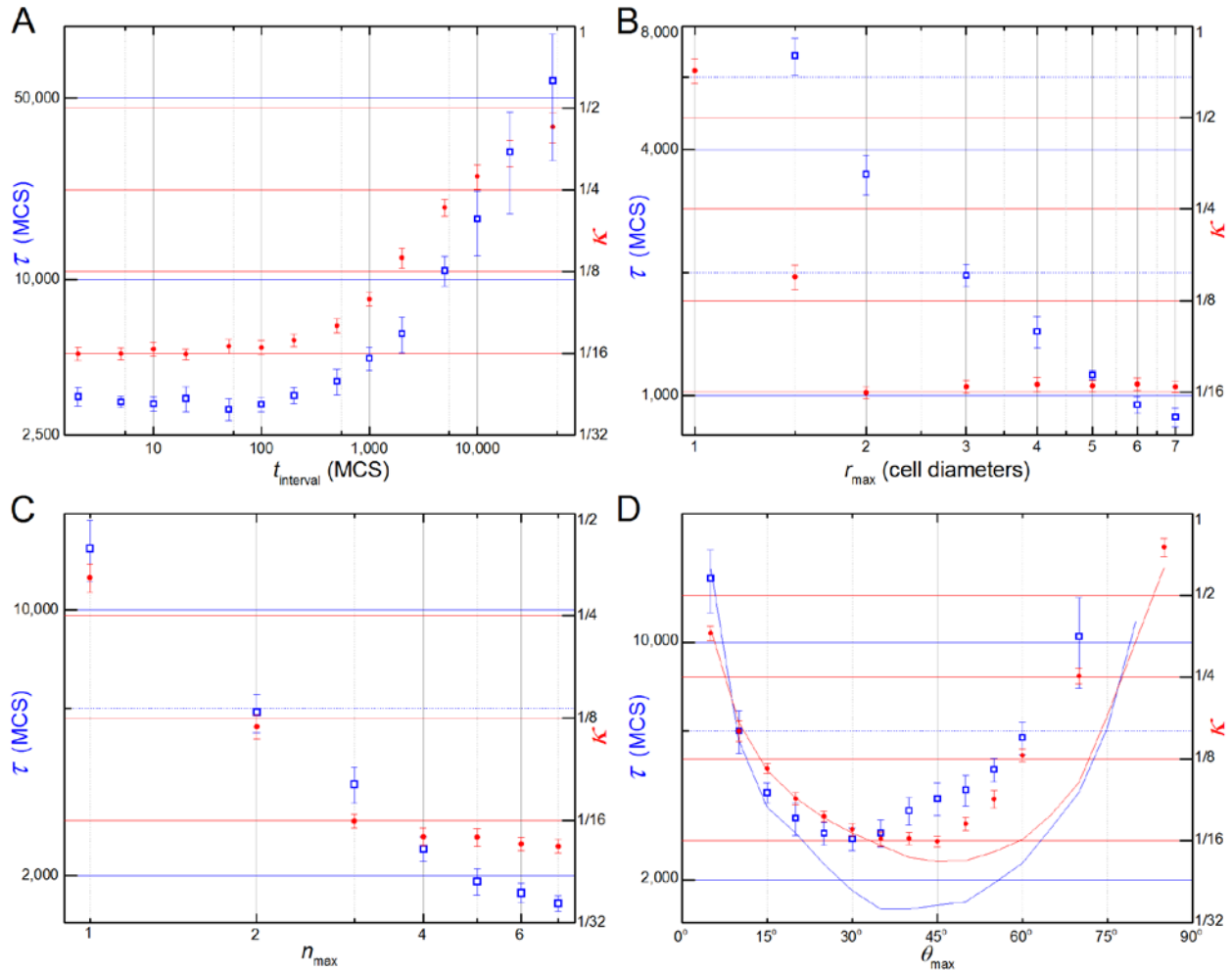


Figure 4.5 – Parameter sensitivity analysis

Left vertical axes and open blue squares correspond to τ values and right vertical axes and solid red dots corresponds to κ values. (A) Filopodial lifetime (t_{interval}) affects CE for time intervals higher than the typical time of **cell** rearrangement (200 MCS). (B) Increasing r_{max} after 2 **cell** diameters has no effects on κ , but τ continues to decrease. (C) Increasing n_{max} after 4 filopodial interactions per **cell** has little effect on κ , but τ continues to decrease. (D) Tissue converges more and faster at lower angles than at high angles, with the best result for κ at $\theta_{\text{max}}=40^\circ$ and for τ at $\theta_{\text{max}}=30^\circ$. Blue and red lines corresponds respectively to κ and τ values for simulations with increased maximum number of filopodial interactions per **cell** ($n_{\text{max}}=7$).

Both κ and τ are concave with respect to the maximum angle of filopodial protrusion (θ_{\max}), since for both $\theta_{\max} = 0^\circ$ and $\theta_{\max} = 90^\circ$ the forces on the **cell** are symmetric (for $\theta_{\max} = 0^\circ$ the **cell** does not extend any filopodia and for $\theta_{\max} = 90^\circ$ it extends filopodia uniformly in all directions) and CE fails (Figure 4.5d). Since the net intercalation force is the difference between the tension forces parallel and perpendicular to the convergence plane (roughly $\int_0^{\theta_{\max}} (\cos(\theta) - \sin(\theta)) d\theta$), we might expect the force to be greatest (and thus κ and τ to be smallest) when $\theta_{\max} \sim 45^\circ$ and for their values to increase symmetrically away from $\theta_{\max} \sim 45^\circ$. The curves, however, have different minima and are not symmetric: the smallest final inverse aspect ratio (κ) is around $\theta_{\max} = 40^\circ$ (Figure 4.5d, red dots) and the smallest elongation time (τ) is around $\theta_{\max} = 30^\circ$ (Figure 4.5d, blue squares).

This asymmetry is caused by the limited number of **neighbors** with which a **cell** can form a link. Both the maximum number of links per **cell** (n_{\max}) and the number of **cells** within the link interaction range (r_{\max}) can limit the actual number of links a **cell** forms. If the maximum number of links per **cell** is fewer than the number of **cell** neighbors within a range of r_{\max} with a small θ (e.g. $n_{\max} = 3$), larger θ_{\max} lead to fewer links with **cells** at small θ and more with cells at larger θ and thus reduce the net tension force in the direction of the convergence plane; for large n_{\max} , **links** form with all possible **cells** within the interaction range r_{\max} with small θ regardless of the value of θ_{\max} . Thus, for large n_{\max} (e.g. $n_{\max} = 7$), the κ and τ curves are roughly symmetrical around their minima at $\theta_{\max} \sim 45^\circ$ (see blue and red lines in Figure 4.5d).

Size effects on CE

The number of **cells** in the **tissue**, N , and the resolution of the model (the **cell** diameter, cd (in lattice sites), used in the CP/GGH representation of the **cell**) can also affect κ and τ (Figure 4.6). The number of **cells** in the deforming **tissue** limits the **tissue's** minimum final inverse aspect ratio to the value when all **cells** are stacked in a single column. Thus the minimum possible value of κ scales with N^{-1} , close to the measured slope of -0.9 ± 0.01 from Figure 4.6a. The time the **tissue** takes to elongate (τ), however increases as a power law ($\tau \propto N^{0.75 \pm 0.03}$), because in a larger **tissue** more **cells** must displace a greater distance in order to achieve the same degree of **tissue** elongation.

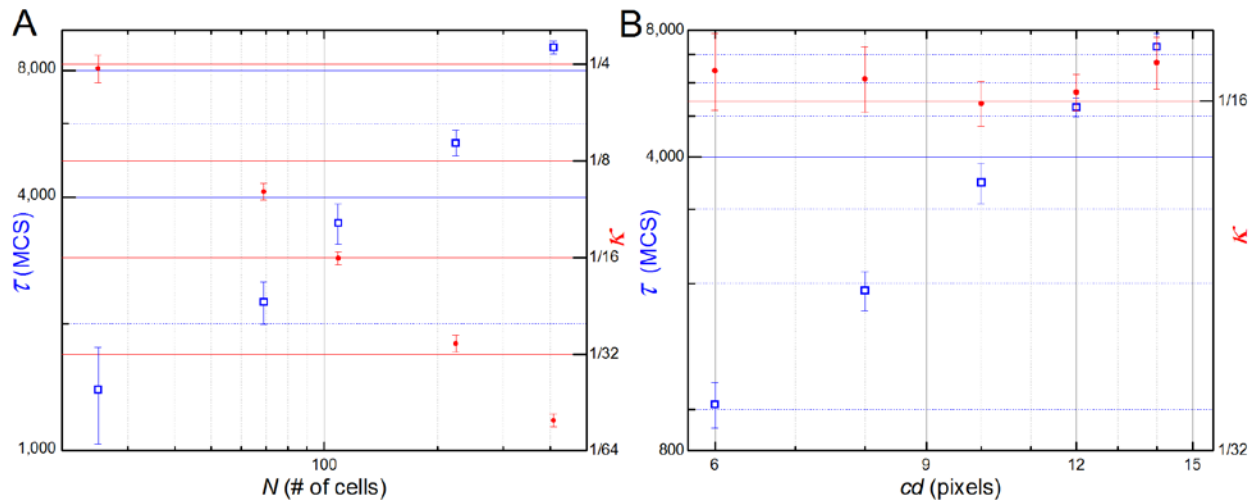


Figure 4.6 – Size effects on the simulation results

(A) Dependence of results on the number of cells (N): τ (blue open squares) increases with $N^{0.75 \pm 0.03}$, while κ (red dots) decreases with $N^{-0.9 \pm 0.01}$. (B) Dependence of results on the cell diameter (cd): τ (blue open squares) increases with $cd^{2.34 \pm 0.04}$, while κ (red dots) is invariant with respect to the size of the cells (note right vertical axis).

A power law for τ is also observed with respect to the **cell** diameter ($\tau \propto cd^{2.34 \pm 0.04}$), as the drag scales as the area of the **cell** (Figure 4.6b, blue open squares). The **tissue's** final

deformation ratio (κ), however, remains relatively unchanged, since the final inverse aspect ratio should correspond to an energy minimum, which depends only on the balance between the **link** tension forces and surface tension, both of which are independent of the **cell** diameter (Figure 4.6b, red dots).

Contact-mediated pulling

The filopodial tension model assumes that **cells** can extend filopodia, contact and pull other **cells** that lie within a given distance, even if they do not touch each other before filopodial extension. An example would be the formation of adhesion junctions between cells which coupled to a contractile stress fiber in both cells. To model these cases, I defined a *contact-mediated cell tension model*, which is identical to the filopodial tension model except that I replaced the maximum link length r_{\max} in the filopodial tension model with the condition that the **cells** must touch to pull on each other (Figure 4.7a).

The qualitative results for the contact-mediated cell tension model do not differ much from the filopodial tension model. The $\kappa \times \lambda_{\text{force}}$ curve is sigmoidal on a log scale and τ decreases with a power law ($\kappa \propto \lambda_{\text{force}}^{-1.18 \pm 0.06}$) (Figure 4.7b). The dependence of κ on the number of filopodial interactions (n_{\max}) is still a power law ($\kappa \propto n_{\max}^{-1.5 \pm 0.03}$) and saturates when $n_{\max} = 4$. The elongation time (τ), however, does not keep decreasing as it does for the filopodial tension model, but also saturates around $n_{\max} = 4$ links (Figure 4.7c), probably because few **cells** have more than 4 **neighbors** with centers near the convergence

plane. The $(\kappa, \tau) \times \theta_{\max}$ curves have minima at $\theta_{\max} = 40^\circ$ and $\theta_{\max} = 35^\circ$, respectively, but are less skewed than in the filopodial tension model (compare Figure 4.7d and Figure 4.5d).

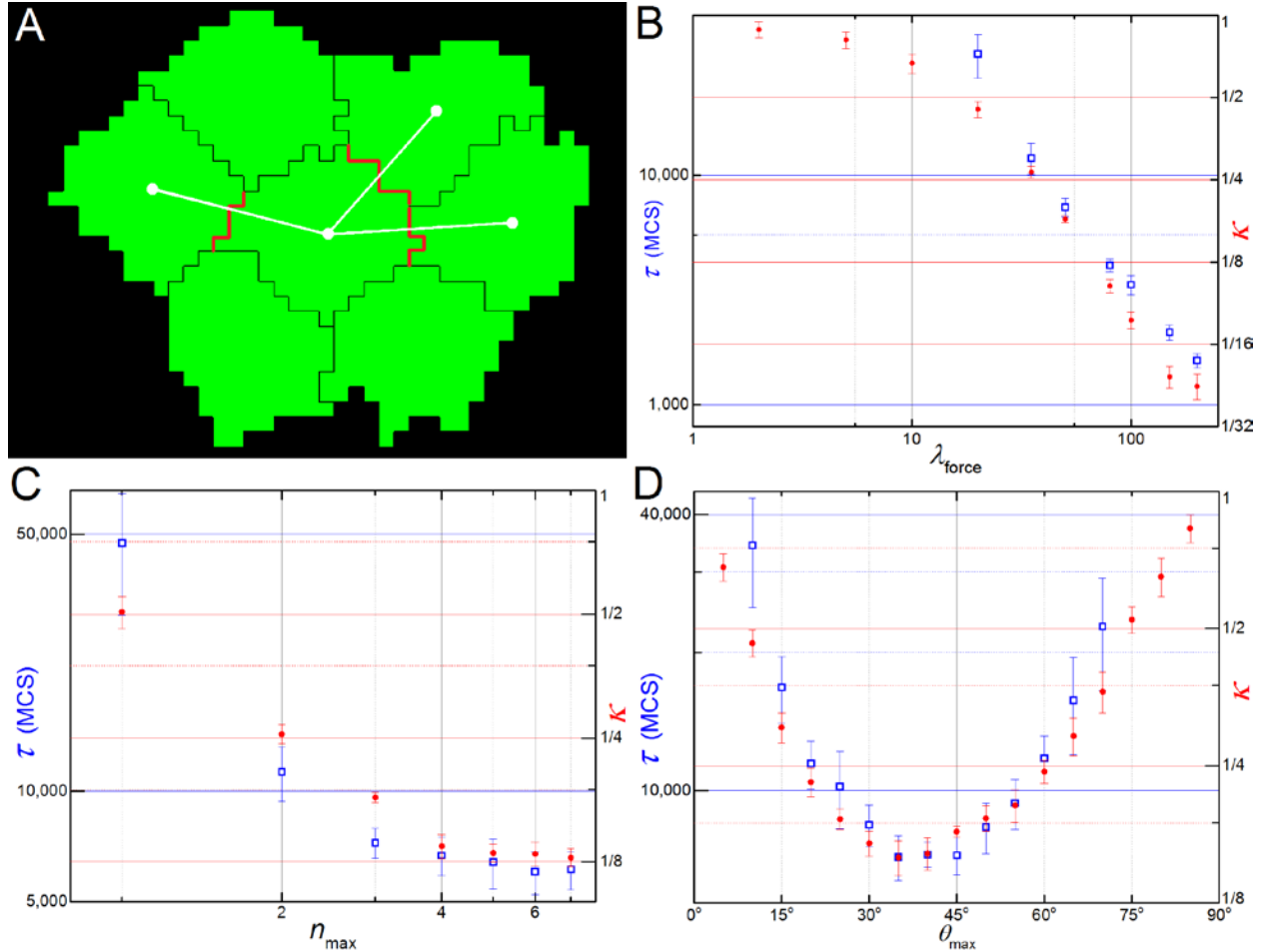


Figure 4.7 – Contact-mediated pulling

(A) Cells only pulls neighbors (here, 3) that share a common surface area (shown in red) and that lie inside a maximum angle with respect to the convergence plane (here the horizontal axis). (B) Dependence of τ and κ with λ_{force} is qualitatively the same as before (Figure 4.4). (C) Dependence with n_{max} is reversed, with the speed of intercalation (τ^{-1}) saturating after $n_{\text{max}}=3$ and κ still decreasing. (D) The $(\kappa, \tau) \times \theta_{\text{max}}$ curves are more symmetric, but the tissue still elongates more and faster at lower angles.

Polarization misalignment

Convergent-extension requires cells to have consistent planar polarity throughout an extensive region of tissue. This correlated orientation might result from a long-range bias from a morphogen gradient, cellular or intercellular differences in protein expression [38], or from a boundary-relay mechanism [24, 25]. In my previous simulations I assumed that all cells had perfectly aligned polarization vectors (Figure 4.2, red arrows), *i.e.*, they all pointed in the same direction with the same magnitude, and they maintained their internal orientation throughout the simulation. To study the effect of polarization misalignment on CE I added a zero-mean Gaussian distributed displacement angle to the cells' polarization vectors and varied the standard deviation of the distribution (σ) while keeping the mean direction (here, the vertical axis) constant.

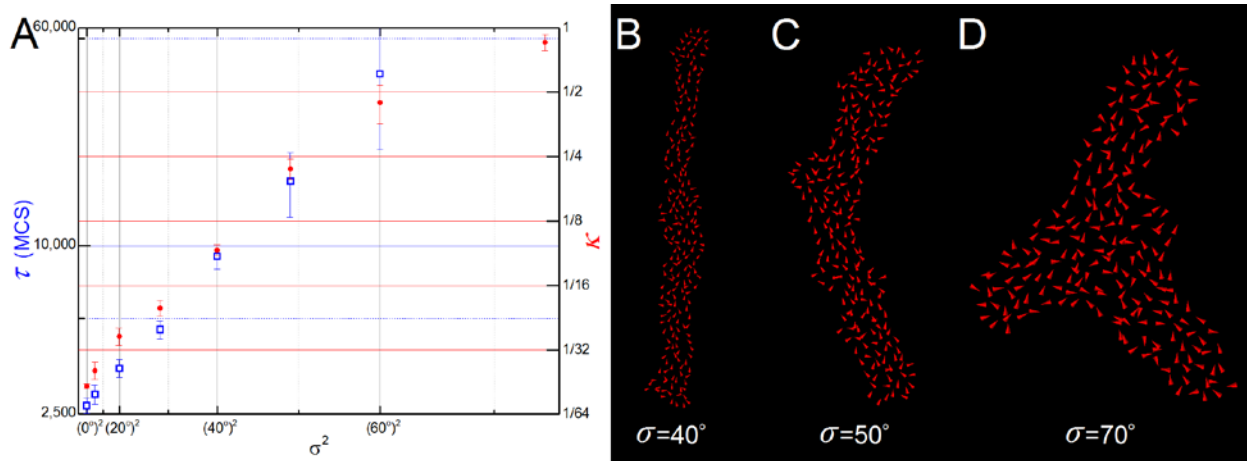


Figure 4.8 – Results for different levels of polarization misalignment

(A) Semi-log graph of τ and κ with the variance (σ^2). Both metrics are exponential functions of the variance. (B-D) Snapshots of 3 simulations with different levels of misalignment ($\sigma=40^\circ$, 50° and 70°). Each cell is represented by a red vector showing the direction of its polarization. The bigger vectors on (C) and (D) are due to zoom.

The filopodial tension model tolerated small polarization misalignments, with a **tissue** with a displacement angle of $\sigma = 10^\circ$ reaching the same final inverse aspect ratio as in the perfectly aligned case with little decrease in elongation rate (an 11% increase in τ). The **tissue** remained aligned with the mean direction of **cell** polarization (the vertical axis) for small misalignments ($\sigma < 40^\circ$, Figure 4.8b), but bent at around $\sigma=50^\circ$ (Figure 4.8c). For polarization misalignments with $\sigma > 60^\circ$, the **tissue** breaks its symmetry and acquires more complex shapes such as the caltrops (see Figure 4.8d). Both metrics are exponential functions of the variance σ^2 (Figure 4.8a).

Heterogeneous cultures

Next I determined the minimum fraction of **cells** extending contractile filopodia needed to drive CE and how this fraction changes **tissue** dynamics. I defined two types of **cells** without filopodia: *passive cells*, which lack filopodia but can be pulled by the filopodia of other **cells**; and non-responsive, or *refractory cells*, which cannot be pulled by the filopodia of other **cells**. The former would correspond to cells whose surface adhesion molecules were compatible with those of the cells extending filopodia and the latter to cells with incompatible adhesion molecules. The parameters for **cells** which produced filopodia were the same as in Table 1.

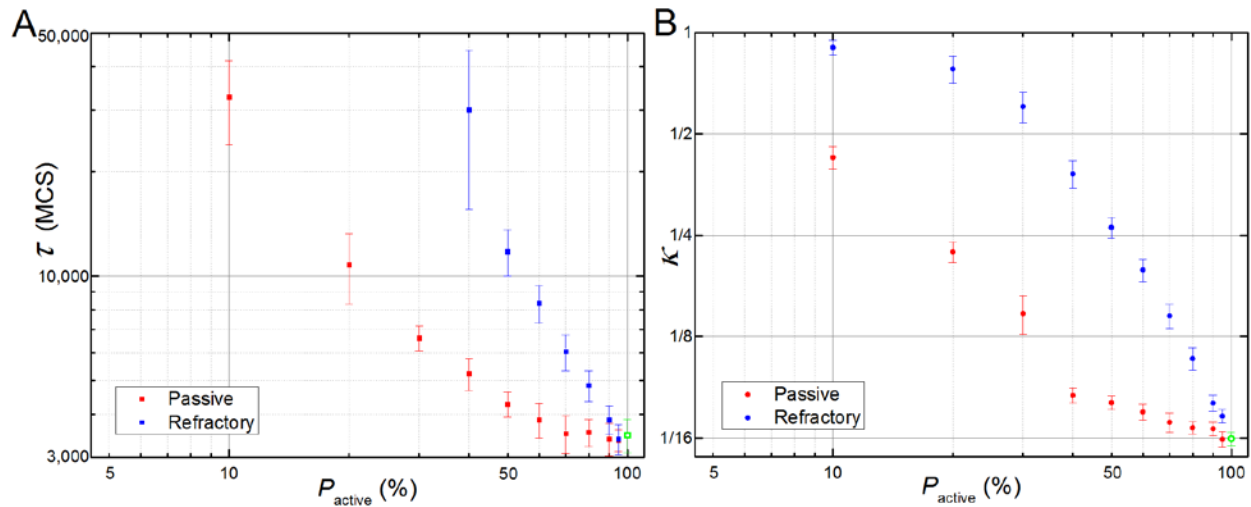


Figure 4.9 – Results for heterogeneous tissues

(A) Dependency of parameter κ (A) and τ (B) with the percentage of active cells in tissues with passive (red dots) and refractory (blue squares) cells. For both graphs, the measured value for the homogeneous tissue is represented by the green open square (A) or dot (B). Values of κ are measured for the whole tissue (active and non-active cells).

For tissues with a mixture of active and passive cells, both κ and τ decrease monotonically with the percentage of active cells in the tissue (Figure 4.9, red dots). However, even a fraction of active calls can drive CE. For 40% or more active cells, the tissue deforms almost as much as a tissue composed entirely of active cells (Figure 4.9b, red dots, and Figure 4.10a), though the elongation time increases with the percentage of passive cells up to twice that for a tissue of all active cells (Figure 4.9a, red dots). For higher fractions of passive cells the final inverse aspect ratio increases significantly with the fraction of passive cells (Figure 4.9a). *E.g.*, for 90% passive and 10% active cells, the tissue's final inverse aspect ratio never drops below 0.3 (Figure 4.9a) and the elongation time τ is more than ten times that for a tissue of all active cells (Figure 4.9b). In all

simulations, the active cells migrate towards the mid line of the elongating tissue, leaving the passive cells at the lateral margins (Figure 4.10b).

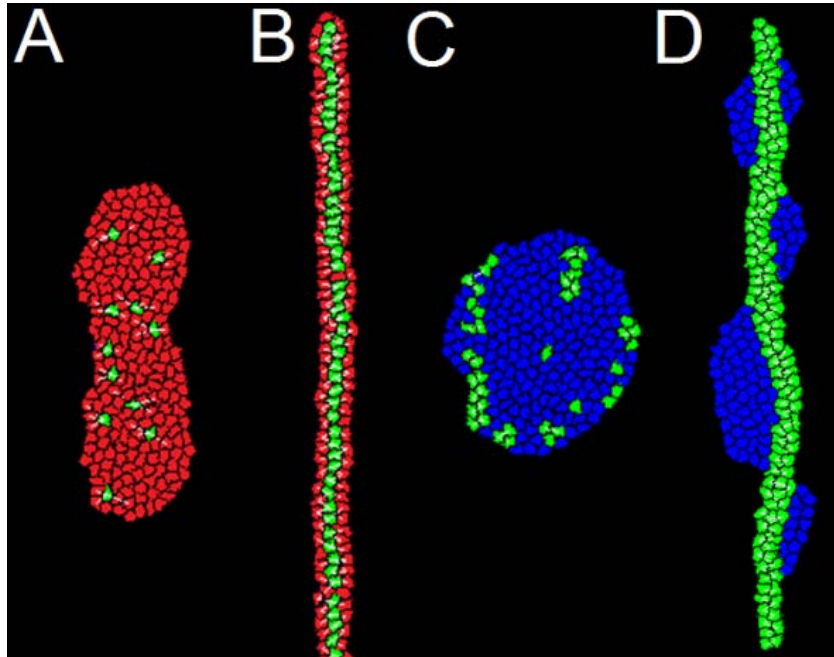


Figure 4.10 – Final shapes of simulations with heterogeneous tissues

Simulations with (A-B) active and passive cells; and with (C-D) active and refractory cells. (A) In a simulation with 95% passive cells (red) the remaining active cells (green) still drive limited CE. (B) In simulations with a higher percentage of active cells (here 33%) the active cells align along the center line of the extending tissue. (C) For less than 20% of active cells (82% of refractory cells, blue) CE fails. (D) For a percentage of active cells above 20% (here, 54%) the two populations sort out, with the active cells forming an elongated tissue and the refractory cells forming clusters on each side.

Refractory cells have a stronger effect on CE than passive cells. CE fails when the percentage of refractory cells is above 60% (Figure 4.9b, blue squares). For higher fractions of active cells, the two populations sort out, with the active cells extending normally and the refractory cells displaced to both sides of the elongating tissue (Figure 4.10d). Surface tension between the cells and the surrounding medium causes the

refractory **cells** to form droplet-like clusters which bend the extending active-**cell tissue** into a wavy bar (Figure 4.10d).

3D versions

The 2D filopodial tension model is a reasonable description of cells within epithelial sheets, where cell movement is confined to a plane. However, in many situations cell intercalation occurs in 3D. That is the case in *radial intercalation* during epiboly of the developing *Xenopus Laevis* embryo, where cells in a multilayered epithelium intercalate and converge perpendicular to the plane of the sheet [39].

The filopodial tension model can be easily extended to three dimensions, but due to the extra degree of freedom, it breaks in two versions, depending on which axis is rotated:

- i) In *equatorial* or *extensional* intercalation, obtained by rotating the 2D model around the polarization vector (the red arrow in Figure 4.2), the **cells** pull on all neighbors that lie in a *convergence plane* (Figure 4.11a). At the tissue level, equatorial intercalation results in the convergence of the **tissue** along the two directions perpendicular to the polarization vector and its extension along the polarization vector (Figure 4.11a²-a²).
- ii) In *bipolar* or *convergent* intercalation, obtained by rotating the 2D model around the convergence line (the blue line in Figure 4.2), the **cells** pull on all neighbors that lie along a *convergence axis* (Figure 4.11b). At the tissue level, the bipolar

intercalation results in the convergence of the **tissue** along the axis of convergence and its expansion in the other two directions (Figure 4.11b'-b'').

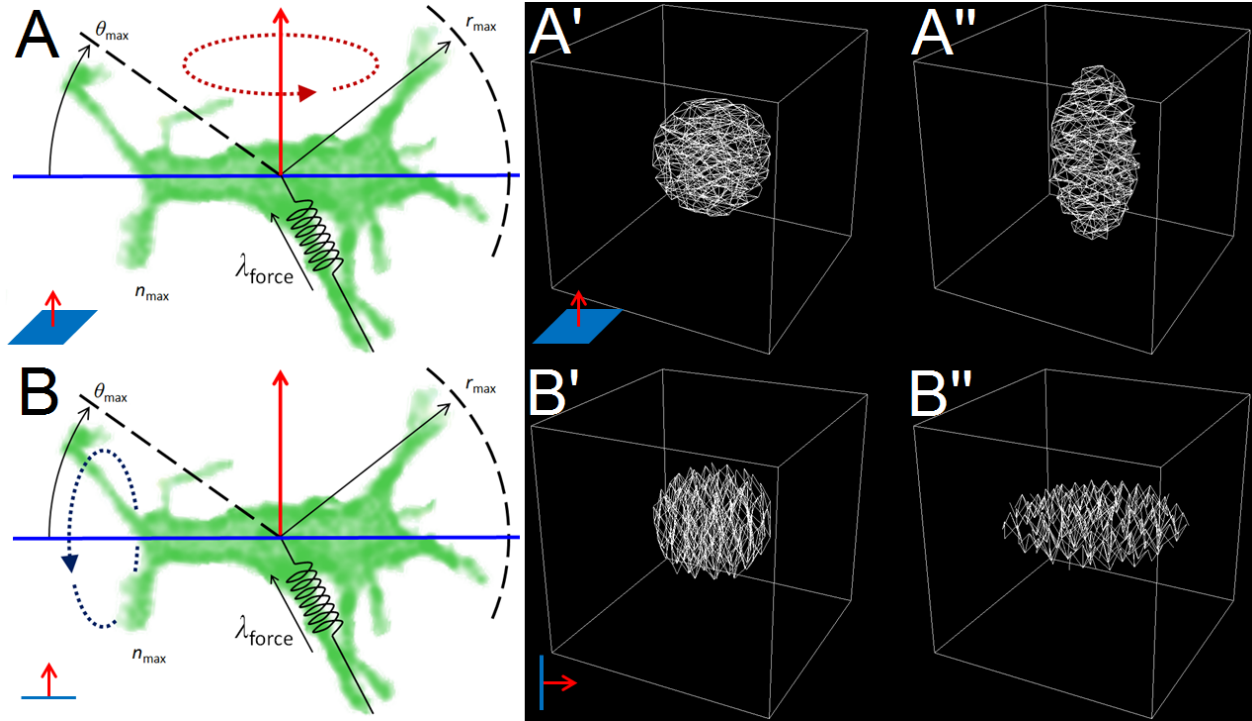


Figure 4.11 – 3D cell intercalation model versions

(A) Rotation around the polarization vector produces the 3D equatorial model. (B) Rotation around the convergence line results in the 3D bipolar model. (A'-A'') Initial and final states of a simulation of the equatorial model with all cells' polarization vectors pointing up. (B'-B'') Initial and final states of a simulation of the bipolar model with all cells' convergence axis lying vertically.

Beginning with a spherical **tissue** with all the **cells** polarized in the same vertical direction, the 3D equatorial model produces a **tissue** resembling a prolate spheroid (cigar shaped, Figure 4.11a''), while the bipolar model produces a **tissue** resembling an oblate spheroid (lentil shaped, Figure 4.11b'').

The bipolar model has more biological correspondence than the equatorial model: cells with unipolar or bipolar protrusive activity are much more common during

development than cells with equatorial protrusive activity³, and the resulting tissue shape from the 3D bipolar model corresponds to the *thinning and expansion* associated with radial intercalation.

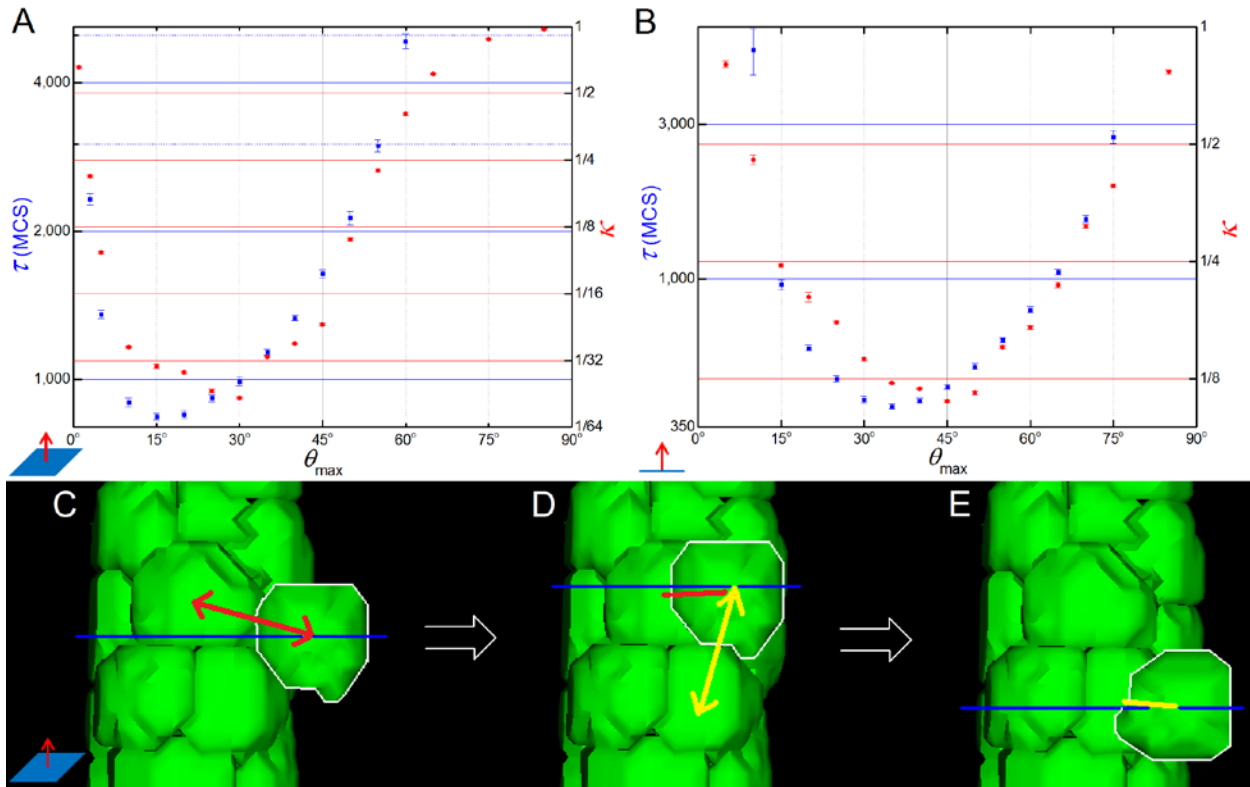


Figure 4.12 – Dependence of τ and κ with θ_{max} in the 3D versions

3D extension model (A) and 3D convergence model (B) dependence of κ and τ parameters with θ_{max} . The range of best values for both κ and τ lies at much shorter angles in the 3D extension model (A) than the 2D model (see Figure 4.5d), which in turn has a range of optimal values slightly lower than in the 3D convergence model (B). (C-D) In the 3D convergence model, pulling forces (red lines) between cells (green) at small angles from the convergence plane (blue line) favors the alignment of the cells perpendicular to the convergence plane, whereas (D-E) pulling forces at higher angles (yellow lines) from the convergence plane destabilize the alignment of the tissue.

³ I am talking about cells surrounded by other cells and not isolated cells lying on a 2D matrix, where cells often extend protrusions in all directions of the plane.

For both versions of the 3D model, the dependence of the parameters κ and τ with λ_{force} , r_{max} , n_{max} and t_{interval} are qualitatively the same as in the 2D model (Figure 4.6) and I choose to not to show it here. The results only differ qualitatively with respect to θ_{max} . For the same values of r_{max} and n_{max} , the 3D convergence model is slightly less skewed than the 2D version, with the best value for κ around $\theta_{\text{max}} = 45^\circ$ and the best value for τ around $\theta_{\text{max}} = 35^\circ$ (Figure 4.12b). The 3D extension model, however, presents a more drastic change in the (κ and τ) vs. θ_{max} curve when compared to the 2D. While the 3D convergence model was slightly more symmetrical around $\theta_{\text{max}} = 90^\circ$, the 3D extension model is very skewed towards small angles, with the best values for κ around $\theta_{\text{max}} = 30^\circ$ and the best value for τ around $\theta_{\text{max}} = 15^\circ$ (Figure 4.12a).

The reasons for the asymmetry is that the final shape of the tissue in the 3D extension model is of a two cell diameter tube orthogonal to the convergence plane, where most of the cells are on top of each other. While pulling forces at small angles from the convergence plane favors the development of such shape (Figure 4.12c-d), pulling forces at higher angles destabilize it (Figure 4.12d-e). In the simulations results shown in Figure 4.12a, the value of $\theta_{\text{max}} = 30^\circ$ represents the optimal maximum angle value where the pulling forces are still able to align the tissue without destabilizing it.

PART II

APPLICATIONS

CHAPTER 5 – LIMB BUD GROWTH

The next remaining chapters apply the new methods described earlier to simulate breaking of symmetry and maintenance of asymmetry in cells and tissues. Since the last covered method was the use of dynamic links to simulate cell-intercalation, I will start the second part of this thesis with a direct application of the dynamic links technique.

Here I will build a simulation of the chicken limb bud growth that relies on cell-intercalation rather than anisotropic growth as the main mechanism. The dynamics links methods is used to test not only if cell-intercalation can drive limb bud expansion, but also to show that direct migration of cells towards the tip of the limb is not a plausible mechanism to explain such process. The work present here was done in collaboration with Dr. James Sharpe and his PhD student, Ms. Gaja Lesnicar-Pucko, who performed all the experiments mentioned in this chapter.

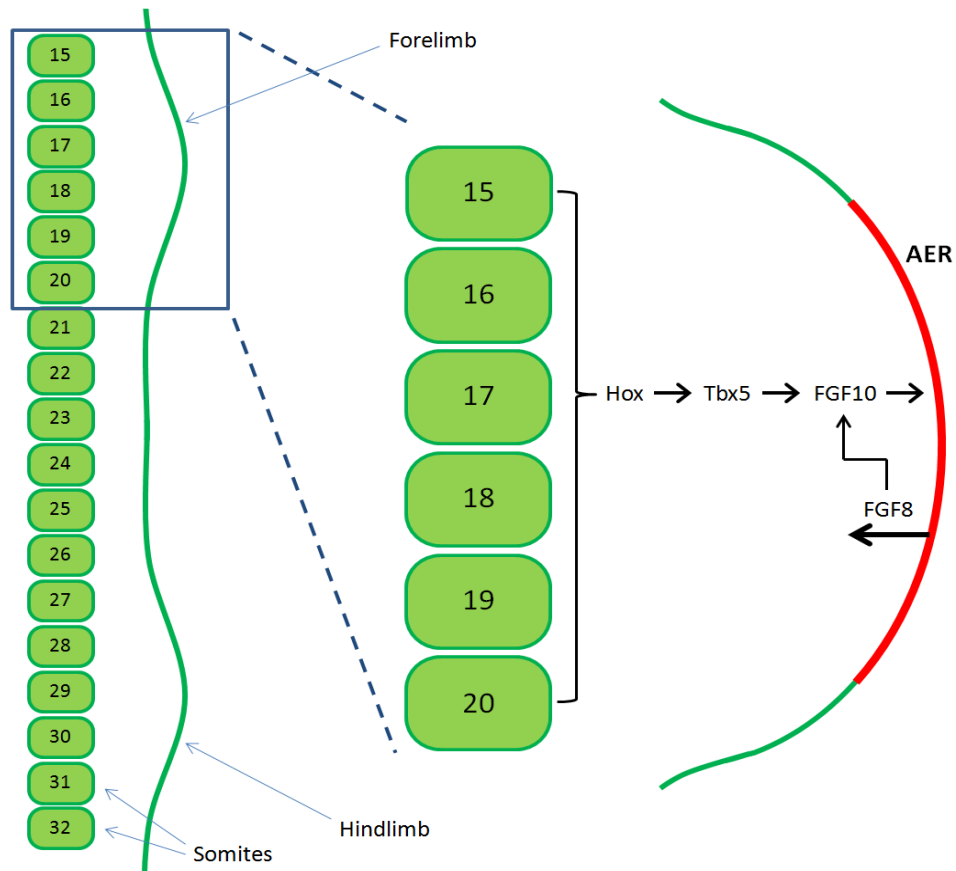


Figure 5.1 – Limb bud initiation in chick

*Forelimbs and hindlimbs form in the lateral plate mesoderm adjacent to somites 15-20 and 26-32, respectively. At those levels, *hox* gene induces *Tbx* gene expression, which in turn induces secretion of FGF10 by the mesenchymal cells on the lateral plate. FGF10 in turn induces the formation of the AER at the boundary of the dorsal and ventral ectoderm. AER is responsible for the secretion of FGF8, which is essential for the sustained secretion of FGF10 by the mesenchyme and limb outgrowth.*

Background

The limb bud is a classical model of organogenesis. In chicken, limb bud development starts about 1.5 days after fertilization, with the wings (forelimb) budding from the lateral plate mesoderm around somite levels 15-20 (where the gene *Tbx5* is

expressed) and the legs (hindlimbs) budding the lateral plate mesoderm around somite levels 26-32 (where *Tbx4* is expressed)(Figure 5.1). At those tissue levels, Hox genes induce the expression of the corresponding Tbx genes and secretion of FGF10 in the lateral plate mesoderm, which in turn induces the creation of the *Apical Ectodermal Ridge (AER)* at the distal margin of the lateral flank, between the *dorsal-ventral (DV)* ectodermal boundary (Figure 5.1).

The AER is a crucial component of the limb bud. Without it the limb fails to develop and becomes truncated, while grafting of the AER onto other *anterior-posterior (AP)* regions of the lateral mesoderm induces ectopic limbs. AER induces limb growth by secreting FGF8 (Figure 5.1), which induces proliferation of the lateral plate mesenchymal cells between the somites and the ectoderm. The length of the AER along the AP axis determines the AP width of the forming limb and its shape (long in the AP direction and thin in the DV direction) is responsible for the flatness of the budding limb in the DV direction.

How does a limb growth?

For many years the dominant hypothesis for the mechanical mechanism producing distal elongation was the proliferation gradient hypothesis, in which a higher proliferation rate in the distal end of the bud was deemed sufficient to explain elongation [40-42].

Numerical simulations of this hypothesis in 2D and in 3D established its plausibility⁴, but lacked rigorously quantitative checks against experimental data.

Recently, however, Boehm *et al.* revisited this theory and built a finite element model of the limb bud based on experimentally measured cell proliferation rates [43]. Under these conditions, the anisotropic growth hypothesis revealed itself insufficient to reproduce the normal limb bud development: replication of the correct shape could only be obtained with thousand-fold differences in cell proliferation rates, far from the almost uniform growth measured across the limb [43].

This suggested that other mechanisms must be behind limb bud development; if it is not growth rates, then cell behaviors in the limb bud mesenchyme are likely to be oriented. Dr. Sharpe and others subsequently found multiple signs of oriented cell activities: the cell shapes and positioning of Golgi show biases in orientation, and activities such as cell division and movement are non-random [43-47]. The molecular basis of these behaviors has also been explored, and strong evidence suggests that Wnt and PCP signaling are required for correct orientation of cellular activities. Fgf signaling is also believed to be important, and besides its proposed role as a mitogen [48], it has also been suggested to act as a chemoattractant [42], or to create a *proximal-distal* (*PD*) gradient of cellular motility [44]. However, the identity of the cellular mechanisms downstream of these molecules is less clear. In particular, three questions remain unanswered.

⁴ The exception being the work by Ede and Law from 1969, which concluded that correct limb growth could only be achieved by a combination of growth and distal migration.

First: to what extent does oriented cell division contribute to PD elongation? In a number of other systems (*eg.* drosophila and zebrafish) control of cell division cleavage plane orientation drives anisotropic tissue elongation [49, 50]. Gros *et al.* highlighted that at early stages of chick limb bud growth (HH19) the average cleavage plane orientation is biased along the PD axis, which may contribute to limb bud elongation [44]. In the mouse, knock-out of *Wnt5a* reduced the coherence of distally-oriented cell divisions and has a negative impact on limb bud elongation [44] (Figure 5.2a). However, in slightly later stages cell divisions are biased away from the PD axis. At stage HH26 a bias along the AP axis has been proposed to drive the widening of the handplate [47], and already by HH21 cell divisions in the dorsal and ventral regions are biased along the DV axis [43, 44], which would appear to work directly against PD elongation. Why does this not cause DV expansion of the bud?

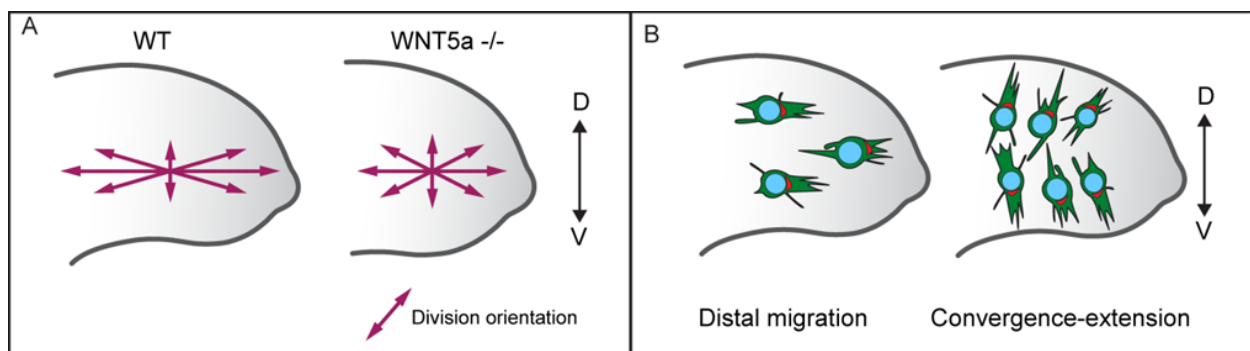


Figure 5.2 – Proposed limb bud behaviors

*(A) Schematic of proposed *Wnt5a* function in limb elongation. Division orientation is biased in PD direction in young limb buds. This bias is affected in *Wnt5a* $-/-$ mouse embryos. (B) Possible cellular behavior underlying limb elongation is distal-ward migration or cell intercalation in DV direction.*

Second: what is the role of directed cell migration in early limb bud elongation? Li and Muneoka suggested that at stages HH19 the average cell orientation is distally-directed, and therefore cells may actively migrate in the direction of elongation [48], since FGF can act as a chemoattractant [42] and mesenchymal cells can exhibit clear migratory behavior *in vitro*. However, if all mesenchymal cells were to migrate simultaneously in the same direction, it is unclear how they would gain traction. The observed average distalward movement of cells has only been documented by averaging cells across a wide region of the bud [44]. Analyzing the regions separately shows that cells in the dorsal and ventral regions of the bud coherently point away from the distal direction, with some cells apparently “migrating” directly towards the ectoderm, rather than distally [44].

Third: do mesenchymal cells in the limb bud perform actively intercalate to produce convergence-extension movement, similar to that seen in other model systems [51-53]? CE would require dramatically different cell orientations than those for a pure migratory hypothesis. Rather than pointing parallel to the direction of tissue elongation, cells might be oriented perpendicular to the primary PD axis, in the direction of intercalation (Figure 5.2b). Observations of cell orientation along the DV direction may support this idea, and intercalation of cells has been reported in the dorsal and ventral regions [44]. However, observed migratory behavior [45, 48] is problematic, as it is not clear how directional cell migration can contribute to convergent-extension. Additionally, the CE hypothesis would suggest that cells in the distal tip of the limb bud should also be DV oriented, but such orientation has not been found.

Project

More detailed analysis of molecular signaling pathways will not resolve these questions. Instead, it is a lack of basic information about individual cell behaviors (dynamic shape change, orientation and movement) that limits our understanding of normal limb bud development. The 3D structure of the limb bud mesenchyme makes cell behavior analysis more challenging. While cell migration, convergent-extension and PCP have been well-studied in quasi-2D epithelia, the relation between individual cell activities and resulting tissue movements in 3D are not well-understood. The lack of experimental data has also inhibited creation of 3D computational models of CE and cell intercalation. To The two models presented in the last chapter attempt to fill this gap.

The new computational model, however, needs to be fed and constrained by experimental data to be of any relevance. Vertebrate organogenesis is generally very sensitive to perturbations, meaning it is difficult to be sure whether cell behaviours remain developmentally-normal *in vitro*. To this end James Sharpe lab has developed a new in-ovo multiphoton time-lapse approach, which is sufficiently non-invasive that normal limb development can proceed after the imaging is finished. This technique made available the determination of the main features and orientations of active cell movements, including cell division, cell movements and intercalations.

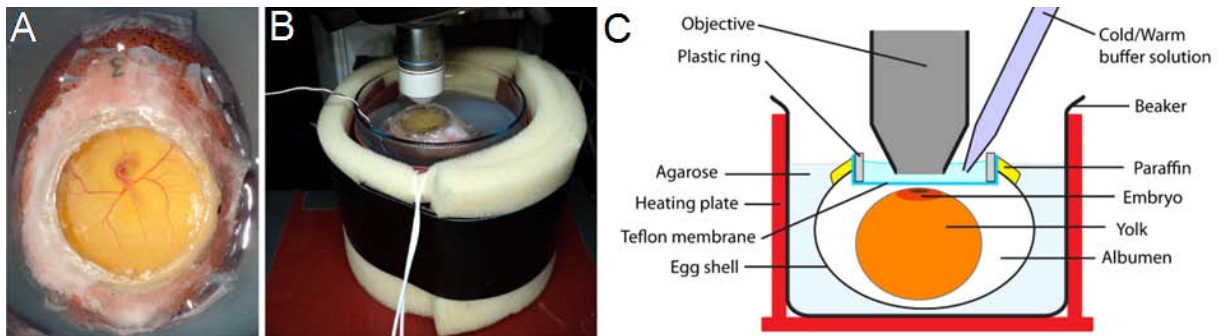


Figure 5.3 – *In ovo* imaging

(A) Chicken egg was windowed, resealed with a ring covered by Teflon membrane and embedded in agarose. (B) Beaker containing an egg, wrapped in a heating tape and insulating foam, and placed on an adapted microscope stage. (C) Applying cold or warm buffer solution to the windowed egg with a pipette allowed temporary stopping and resuming of the embryo heartbeat.

Experimental techniques

Because *in vitro* techniques are not suitable for study of limb bud elongation between stages 21HH and 23HH, when growth depends on blood flow, Dr. Sharpe, from CRG, developed an *in vivo* technique for later stage embryos that minimizes tissue damage and allows normal development after an in between imaging. The eggs are sealed with a plastic ring covered with a Teflon membrane, which allows normal gas exchange (Figure 5.3a). To damp external vibrations and temperature changes, the egg is submerged in a beaker filled with 1% agarose, wrapped in a flexible heating plate (Figure 5.3b). To reduce movement due to the strong heart beat present after stage 21HH, they added ice cold PBS onto the Teflon membrane to cool and stop the heart beat for a few minutes (Figure 5.3c). After imaging, they reheated the embryo with warm PBS and the heart spontaneously resumed beating. Although growth in imaged embryos was slower than by embryos kept in an

incubator, the embryos placed in an incubator after repeated cycles of imaging survived and their limbs developed normally.

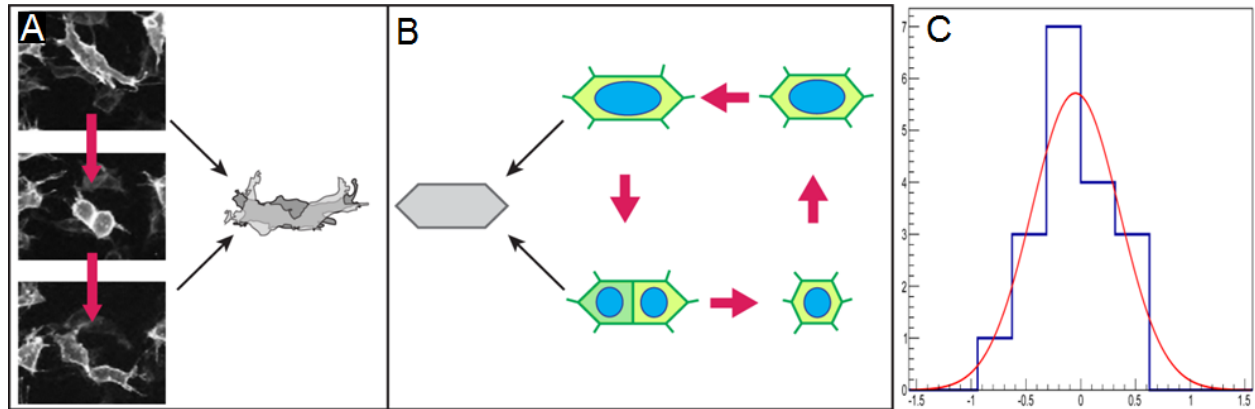


Figure 5.4 - Division orientation

(A) Time-lapse image sequence of limb bud mesenchymal cell division. Mother cell shape predicts the direction of daughter-cell separation and it matches the combined shape of daughter cells (overlaid grey silhouettes). (B) Mesenchymal and epithelial cells divide in a similar way. (C) Graph showing the high correlation between mother cell orientation and daughter cells angle separation ($n=18$).

Experimental Results

To track individual cell position and shapes in the chick embryo *in vivo*, Ms. Gaja Lesnicar-Pucko electroporated stage 15HH embryos with a membrane-targeted gpiEGFP that produced a salt and pepper distribution of labeled cells (Figure 5.5a) and allowed close monitoring of cells during their life cycle.

Cell-division orientation in early limb bud aligns toward the ectoderm; in much of the bud divisions are almost perpendicular to the PD axis of limb-bud elongation and so oppose elongation [43]. In other tissues, cell-division orientation aligns with the direction of tissue elongation and may promote elongation [49, 50]. Why does the ‘mis’-oriented

division not cause DV limb bud expansion? The numerous cell divisions during our *in ovo* time-lapse imaging allowed us to monitor individual cells' division patterns in detail. In the limb bud, the size and shape of a mother cell is usually very similar to the combined territories of the daughter cells after separation (Figure 5.4a,b). These mesenchymal cells usually have a clear long axis, which correlates closely with the positions of the two daughter cells after division (Figure 5.4c).

The salt and pepper distribution of electroporated cells also allows measurement of the very fine projecting filopodia. Analysis shows that all cells have filopodia, and cell shapes vary widely. About 10% of the cells are monopolar, with most filopodia extending from a wide lamellipodium on one side of the cell and just a trailing edge of cytoplasm on the other (Figure 5.5b). About 30% of cells are bipolar, with a clear elongated primary axis but without any obvious asymmetry to distinguish a possible front-end from a back-end (Figure 5.5c-d). The remaining 60% of cells (n=40) were neither monopolar or bipolar, with cell bodies of a wide variety of apparently arbitrary shapes, with complex arrays of filopodial protrusions of up to 3 cell diameters in length (Figure 5.5e-f). When observed in time-lapse movies, the filopodia were very dynamic, with an average of 0.46 filopodia being extended or retracted per hour (372 filopodia analyzed from 8 cells) (Figure 5.5g).

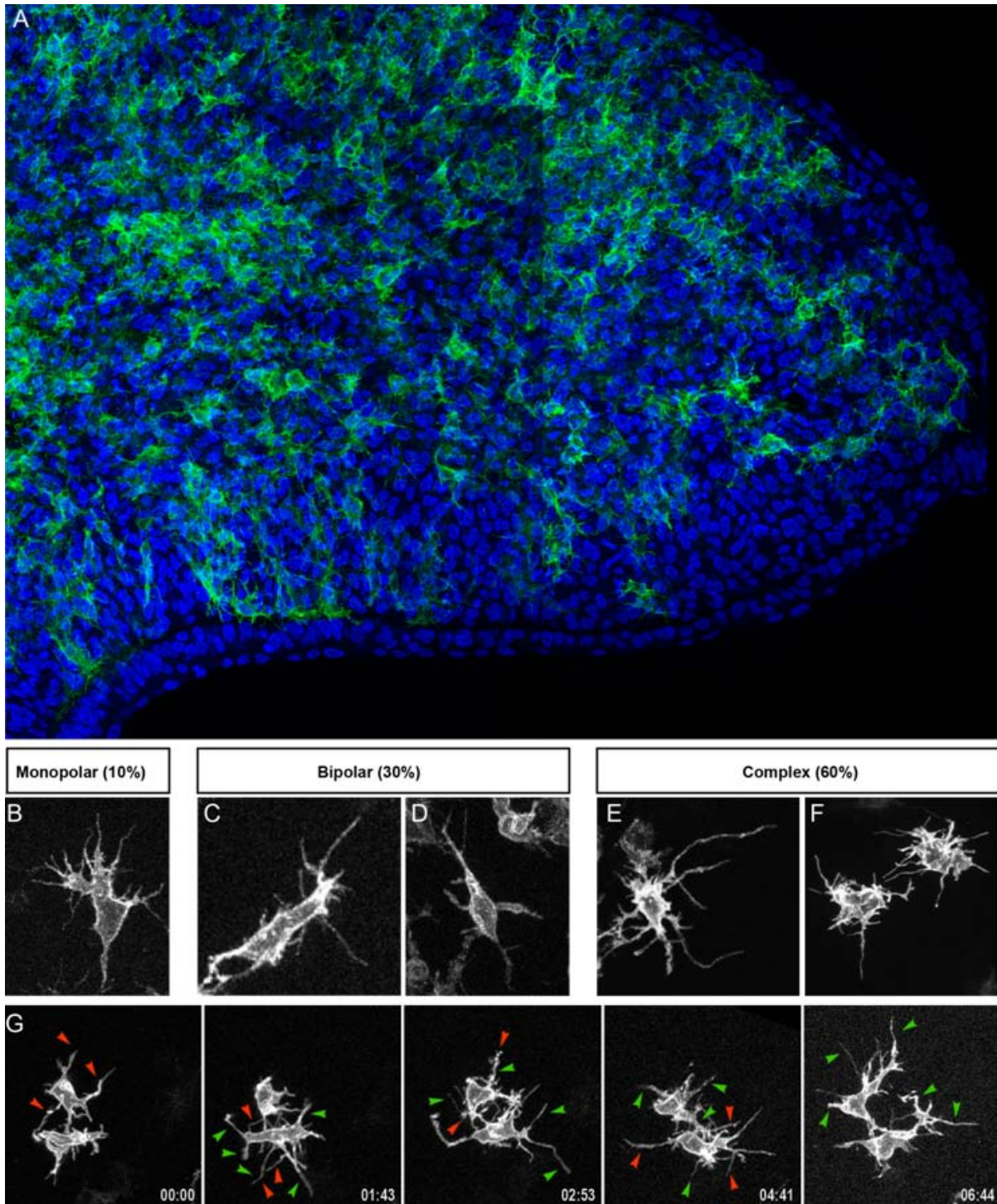


Figure 5.5 – Mesenchymal cell shapes

(A) A stage 22HH embryo limb was electroporated with *gpiEGFP*, incubated for 36 hours, fixed and immuno-stained against GFP (green) and stained with DAPI (blue). Cell shapes vary from monopolar (**B**), to bipolar (**C**, **D**), to spider-like multipolar (**E**, **F**). (**G**) Time-lapse sequence showing filopodial activity.

Arrows show positions where filopodia will form (green) or retract (red).

Although a this simple analysis of cell shapes provides little insight into the physical mechanisms of cell's force generation, the ensemble of labeled cells across the entire limb bud shows clear patterns of functional organization with more proximal cells having more DV-oriented filopodia (Figure 5.5a). However, more detailed monitoring of larger groups of cells over longer times will be necessary to understand the detailed role of filopodial geometry and dynamics in limb bud morphogenesis.

The distributions of mesenchymal cell orientations in the limb bud between stages 21HH and 23HH do not support the mass migration hypothesis for limb bud elongation [43, 44]. Nevertheless, signs of cell migration have been found. The *in vivo* time-lapse movie revealed some mesenchymal cells with very clear migratory behavior, as reported in chick and mouse limb bud [44, 45, 48]. Migrating cells differs from others both in their long range directed movement relative to their neighbors, and their monopolar morphology (Figure 5.6a-b). However, only around 6% of cells are migratory at any moment (n=200), and migration shows no clear bias in any direction. Furthermore, no migrating cells maintained their migratory activity throughout the entire 8-12 hours time-lapse sequence, instead relatively stationary cells occasionally became migratory, and vice-versa. Before or after a migratory period, a cell was indistinguishable from its neighbors. Cells also tend to migrate at specific points in the cell cycle: migration events just after cell division were 10 times more common than those just before cell division (48% of total migration events, versus 5%, n=44), with the two daughter cells always moving away from each other (Figure 5.6c). Together these observations suggest that individual cells in the mesenchymal

tissue are a relatively homogeneous population, switching between migratory and non-migratory behaviors.

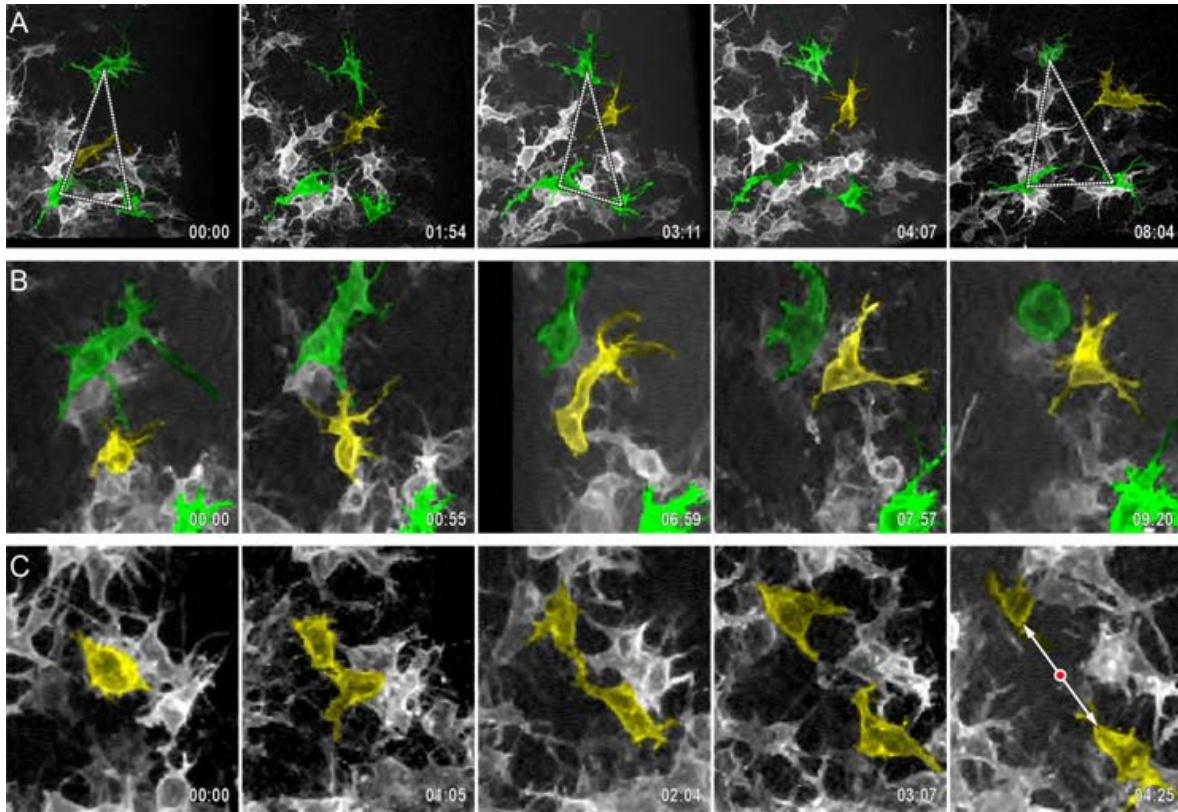


Figure 5.6 – Cell migration analysis

(A-C) Time lapse series showing gpiEGFP expressing mesenchymal cells over time. Yellow and green cells have been false-colored for better visualization. In all series, distal is to the right and proximal is to the left. (A,B) Time-lapse sequences showing cell migration. Yellow cell is migrating, green cells and the triangle are shown to serve as reference points to highlight relative displacement of the yellow cell. (C) After cell division, daughter cells often migrate in opposite direction.

The observed movement of any cell comprises three distinct components: passive movement, where cells are pushed and pulled by external forces; advection, which reflects the net flow of the tissue; and active movement, where the cells exert specific or directional forces on surrounding cells, causing an autonomous movement relative to its neighbors. To

separate these three components, Sharpe's student registered the positions of electroporated cells from the first time-point onto the last time-point (Figure 5.7).

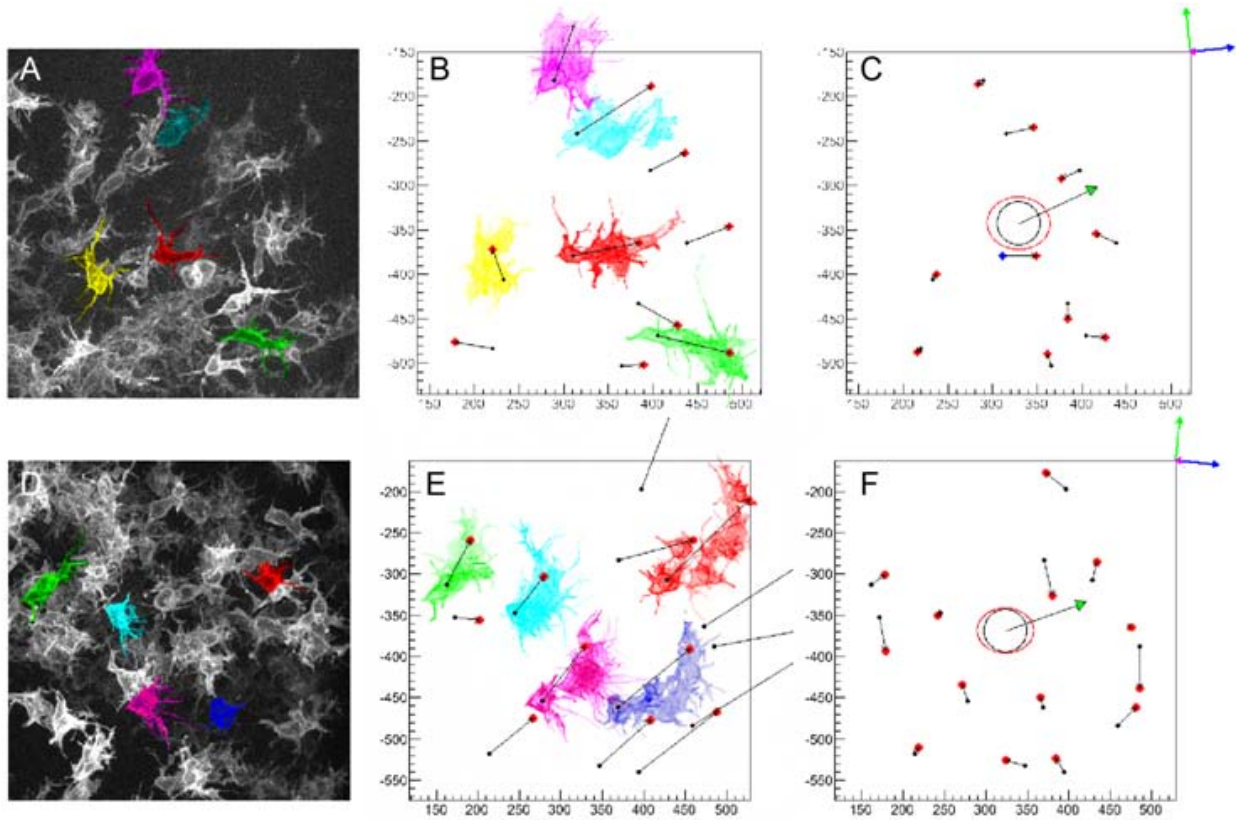


Figure 5.7 – Cell registration and time-lapse analysis

(A-F) Cell coordinates from initial (A, D) and last time point from time-lapse videos were measured and plotted on a graph (B, E). Initial and last time point were registered by translation, rotation and anisotropic scaling (red, green and blue arrows in the right upper corner) (C, F). Direction toward the nearest ectoderm (green headed arrow) is shown. The anisotropy of tissue expansion is represented as a red ellipse on black circle (initial size).

The results show that limb bud tissue expansion is anisotropic, with the direction of greatest growth direction usually oriented proximo-distally. In Figure 5.7c, the change in shape from the black circle to the red ellipse indicates anisotropic expansion during the time-lapse. In convergence-extension with no tissue growth, the expansion of tissue along

one axis balances the contraction along the other axis to keep the volume constant. This situation would result in a red oval of the same size area as the original circle; longer, but narrower. In the limb bud experiments the red oval was never narrower than the original circle. This suggests that the tissue movements result from a combination of general growth in all directions, and a counterbalancing convergence which restricts the expansion along a certain axis, but enhances expansion in the perpendicular direction. Since the direction of preferential expansion is substantially parallel to the PD axis, these observations are consistent with a hypothesis that limb bud elongation is driven by “growth-compensated convergent-extension” (Figure 5.13).

The convergence aspect of the tissue movements could be driven by active cellular intercalation which would imply neighboring cells moving in opposite direction. To check this, the global tissue movements were subtracted from the local relative cell movements. The individual cell movements appear negatively correlated with their neighbors, with cells routinely moving in opposite directions and usually along the axis of tissue convergence. These observations alone are compatible with both active cell-intercalation along the DV axis and cells moving distally in response to a chemoattractant. However, in the later scenario the cells' shapes should be monopolar, with the filopodia distally oriented. Together with the observation that the cells have DV oriented filopodia, the negatively correlated movements along the axis of tissue convergence suggests that there are genuine intercalation movements

3D limb bud model

Having defined the possible behaviors of individual mesenchymal cells, I created a 3D model of the limb bud to test a series of cell-level behavioral hypotheses, ranging from oriented divisions to pure distally-oriented migration and convergent-extension, for compatibility with normal limb growth. To achieve this, the virtual cells should be able to grow, divide at specific planes and extend dynamic filopodia which can pull on other cells to directly cause active cell movements. The latter has not been previously simulated within the Cellular Potts framework and this project is what inspired me to extend the cell intercalation model from 2D to 3D.

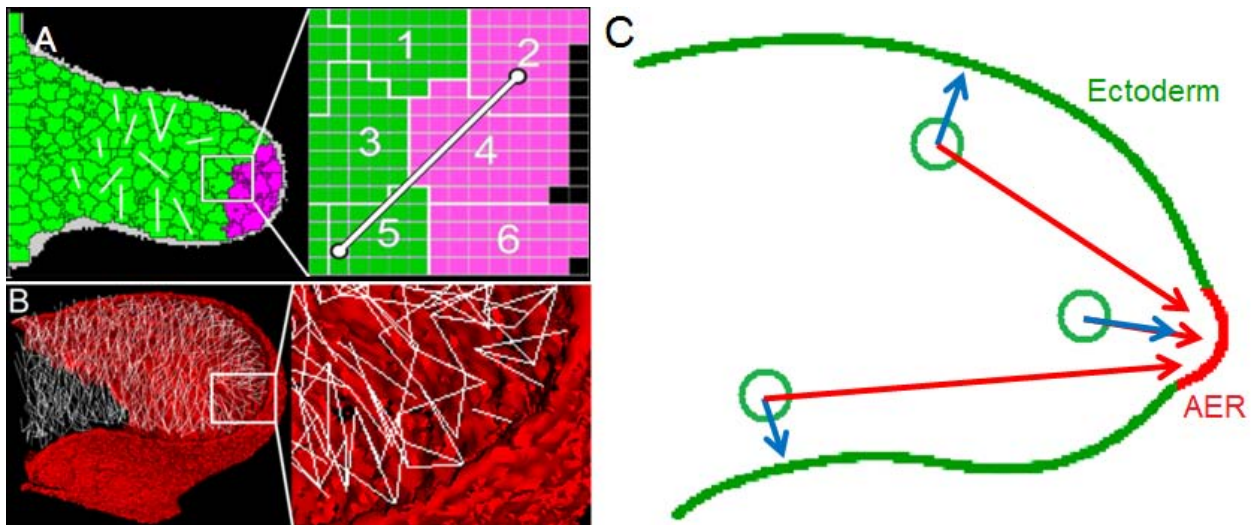


Figure 5.8 – 3D limb bud model

(A) Cells form links with their neighbors and pull on them. The distal-most cells in pink indicate the mesenchymal region affected by FGF8 and the white lines selected links between cells. (B) 3D view of intracellular links from (A) inside a simulated limb bud. (C) Schematic cross section of the limb showing the ectoderm (blue) and AER (red) vectors for 3 cells.

In the model, virtual filopodium pulls two **cells** together with a force acting on their centers (Figure 4.13a and Figure 5.8a-b). Since real filopodia in the limb bud extend multiple cell diameters, I set the maximum length of virtual filopodia to 2 **cell** diameters. The rate of filopodial creation, persistence, and bias in orientation were parameters of the model, as described Chapter 4. I considered two sources of orientation information – the **ectoderm** as a whole and the **AER**. The former forms an epithelial layer surrounding the mesenchymal **tissue**, and the virtual **AER** is defined as a narrow, distal strip of ectoderm with its AP extent adjusted to reflect the AP width of the AER. Rather than explicitly simulating diffusion gradients, each **cell** calculates 2 vectors: one from the **cell** center of mass to the nearest **ectoderm**, and the other from the **cell** center of mass to the nearest part of the **AER** (Figure 5.8c). All simulations were performed with a fixed uniform proliferation rate.

The model starts with the 3D geometry of a 21HH chick limb bud obtained from an *Optical Projection Tomography* (*OPT*) scanning of an embryo (Figure 5.9a). I populated this volume with virtual **cells** to define the initial conditions of the mesenchyme in the simulation. I defined the ectoderm as a monolayer of a flat type of cell completely covering the mesenchymal mass. Rules for **ectodermal cells** defined cell adhesion, growth and division so to maintain a contiguous **ectodermal** layer despite the growing **mesenchyme** underneath. To reduce computation time, **cells**' volumes were about 16 times larger than real ones (Figure 5.8a).

Random vs. oriented cell divisions

I first used the model to compare the effects of random and two types of oriented cell divisions on final limb bud shape (Figure 5.9). In oriented cell division, the division plane was either a) perpendicular to the vector connecting the **cell's** center of mass to the closest point in the **ectoderm** (Figure 5.9c), to simulate the observed cell divisions [43]; or b) perpendicular to the vector connecting the **cell's** center of mass and the closest point in the **AER**, to simulate a PD division preference which should result in distal elongation (Figure 5.9d). We would expect the cleavage plane perpendicular to the ectoderm, observed in the limb bud mesenchyme, to broaden the limb bud, while a cleavage plane perpendicular to the cell-AER axis should elongate the limb bud. The limb bud shape and growth pattern of both oriented division simulations are barely distinguishable from the random cleavage simulation (Figure 5.9b), showing that **cell** movement and shape relaxation after division effectively erase the effects of cleavage plane orientation.

Combined with Dr. Sharpe's time-lapse imaging results, we concluded that, in contrast to some other studied cases [49, 50], oriented cell division in the chicken limb bud is most likely a consequence of other morphogenetic activities, rather than a driver of morphogenesis. Thus to explain limb bud shape we must focus on other cell behaviors, in particular the various types of active movement cells perform between cell divisions.

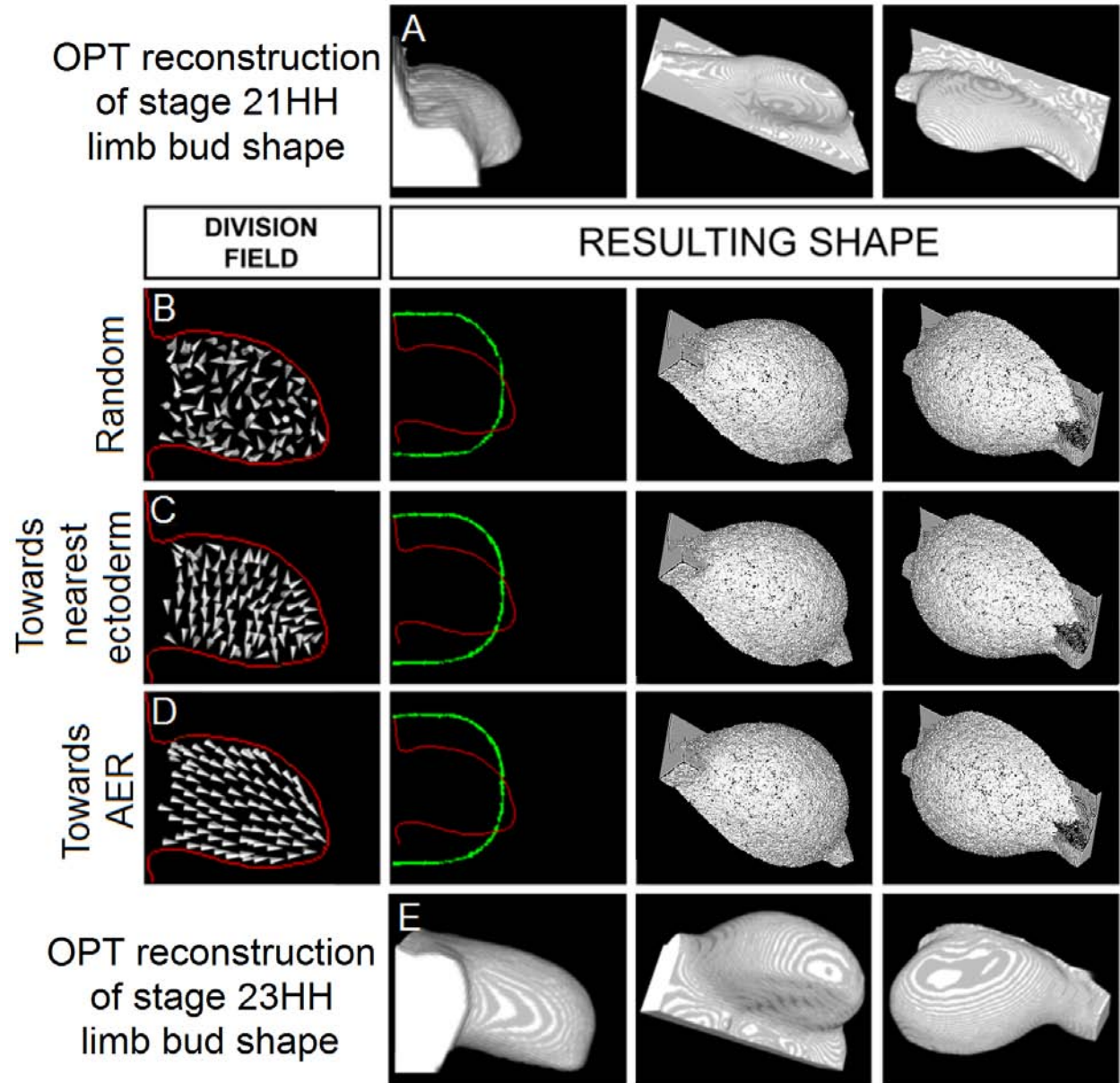


Figure 5.9 – Division orientations and limb bud shapes

(A,E) Three different views of the real shape of a (A) 21HH and (E) 23HH limb bud obtained with OPT.
 (B-D) Panels show division orientations; AP cross section view of the initial (red) and final shape of the limb bud; and 3D views of the final limb bud shape from ventral and dorsal sides. Cells divide at (B) random orientations or towards the (C) nearest ectoderm or (D) the AER.

Direct migration

In directed migration hypothesis, all cells migrate distally by extending filopodia towards their distal neighbors and then attempting to pull themselves forward (Figure 5.10b). In simulations of distal-directed cell migration, all **cells** extend contractile filopodia towards the nearest point in the **AER**, while **cell** divisions are randomly oriented. However, in these simulations the limb bud fails to elongate because, as each **cell** attempts to crawl distally, it pulls its **neighbors** proximally. The net result of these PD-oriented contraction forces is to shrink the bud along the PD axis, rounding up the limb rather than flattening it into a paddle shape.

Ectoderm-oriented cell intercalation

Intuitively it appeared that contractions perpendicular to the PD axis would lead to the convergent-extension movements seen in the time-lapse sequences. We therefore explored the effects on limb bud shape from filopodial orientations derived from combinations of ectodermal and AER influences. Surprisingly, even when **ectodermal** influence was strong compared to **AER** influence (Figure 5.10c), this the **limb bud** rounded into a ball of **tissue**. Only when the **AER** influence was extremely weak (or zero) and **cells** extended filopodia mostly towards the nearest **ectoderm** did the limb bud elongated in the PD direction (Figure 5.10d).

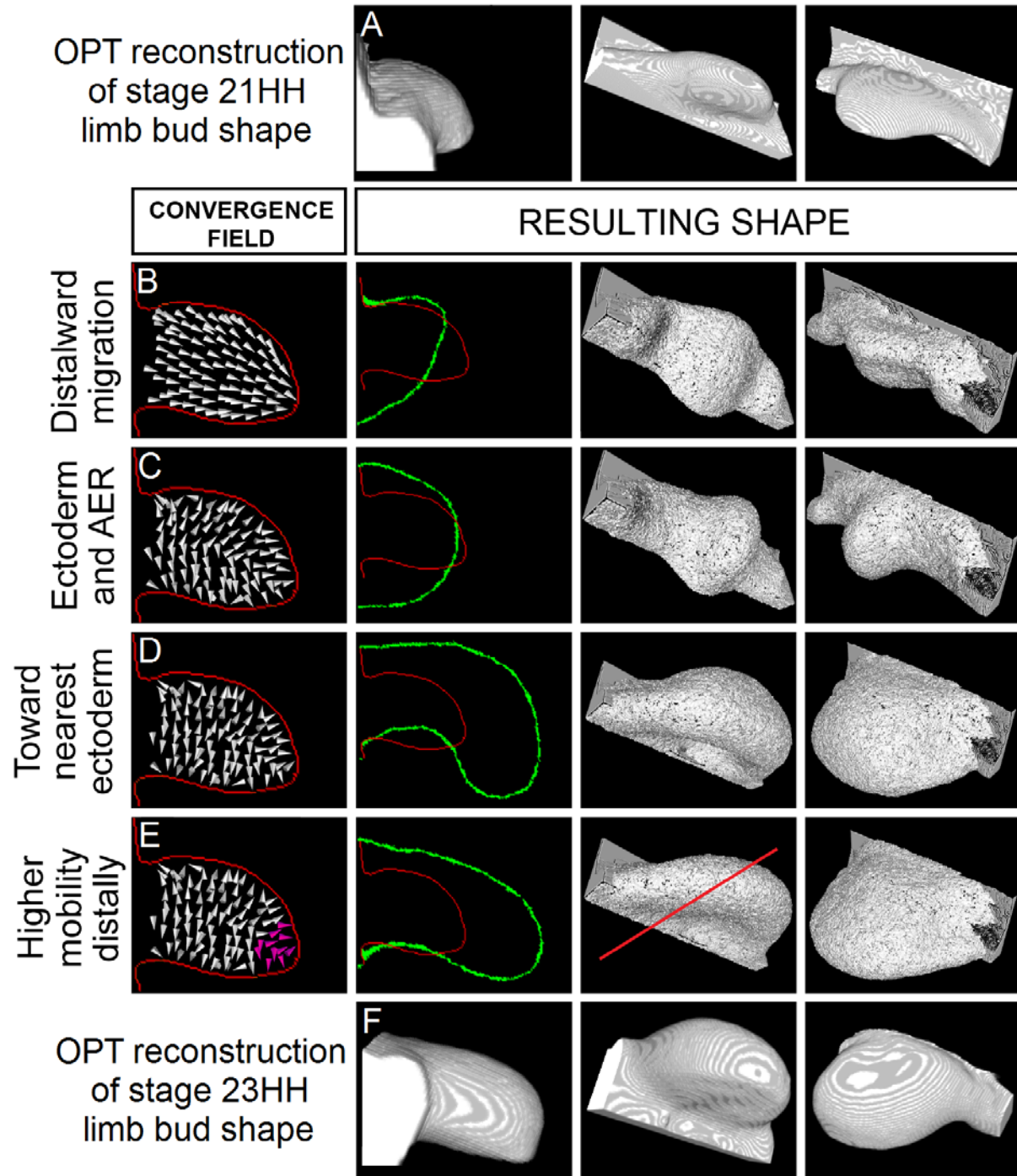


Figure 5.10 – Migration vs. cell intercalation

(A,F) Three views of the shape of a (A) 21HH and (F) 23HH limb bud. (B-E) Panels show (from left to right): AP limb bud midline with filopodial orientations; AP cross section of the initial (red) and final shape of the simulated limb bud; and 3D views of the final limb bud shape from ventral and dorsal sides. Cells extend filopodia towards the AER (B), towards the ectoderm and AER (C); and towards the ectoderm (D,E). In (E) cells close to the AER were softened, allowing better distal elongation.

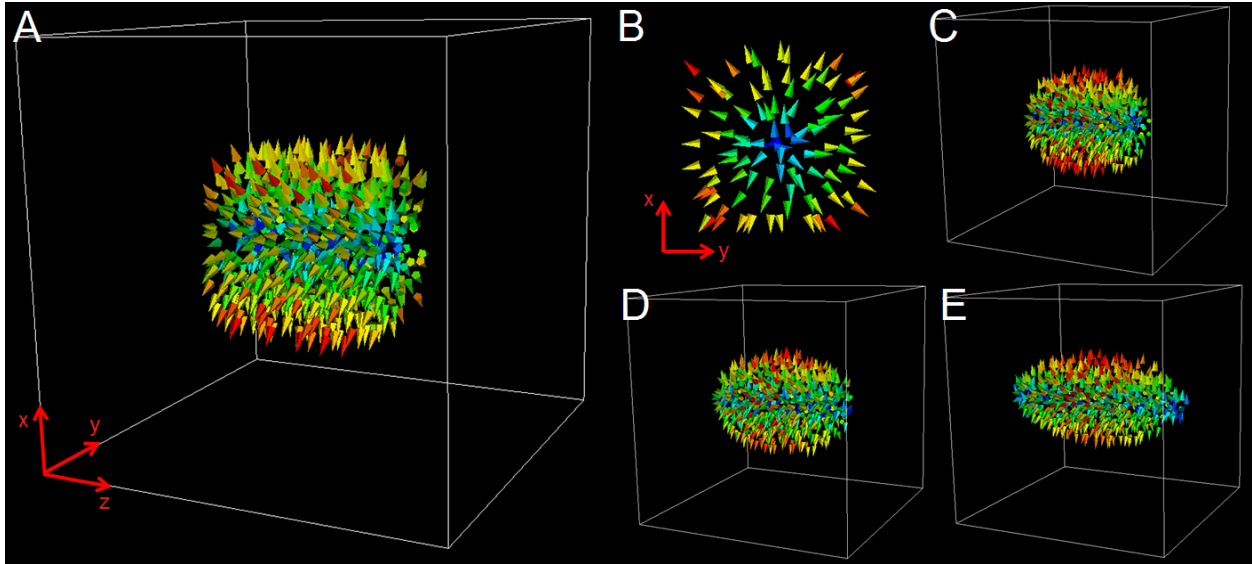


Figure 5.11 – Toy model for limb elongation

(A-B) Initial condition of the toy model, with all cells' filopodia pointing radially outward in the x-y plane.

(A) 3D view of the model visualizing cell orientations. (B) Cross section along the x-y plane. (C-E) As the cells intercalate, the tissue elongates in the z-direction.

The **ectoderm**-oriented filopodia case resulted in limb bud elongation because when **cells** in the bipolar 3D model (see Chapter 4) pull along a given direction, the **tissue** as a whole expands in the other two perpendicular directions. However, given the topology of the limb and the **cell** polarity distribution, expansion in the AP direction is canceled by **cells** lying anteriorly or posteriorly. Thus the **cells** squeeze out along the PD direction, causing strong distal elongation (Figure 5.10d). This is better illustrated by the toy model shown in Figure 5.11, where **cells** are distributed in a cylinder and **cell**'s filopodia orientations lie in the x-y plane and points radially outward from the cylinder axis, in a simplified caricature of the PD cross section of the limb bud. As the simulation proceeds, the tissue elongates in the z-direction due to the **cell** intercalation towards the cylinder midline in the x-y plane (Figure 5.11c-e).

The *in-silico* exploration above clearly predicts the cellular contraction orientations compatible with observed changes in limb bud shape: contractions should mostly be perpendicular to the ectoderm. To measure cellular orientations in the limb bud, Ms. Gaja Lesnicar-Pucko thick-sectioned HH21 limb buds that had been electroporated with the membrane-bound gpiEGFP protein as previously described [43]. She then measured the angles from the center of the nucleus to the ends of all filopodia, to the Golgi body, and to the nearest ectoderm. Dr. Musy (a postdoc in Dr. Sharpe's lab) then analyzed the frequency of filopodia in different directions through the whole limb and found no bias towards the ectoderm (Figure 5.12). However, the average filopodial direction for each cell (Figure 5.12d,e) showed that while many filopodia point away from the ectoderm, the majority of cells have most of their filopodia on the ectodermal side. Visualization of filopodial orientations requires electroporated cells to be well separated from other labeled cells, limiting the total number of analyzed cells in a tissue section. By contrast, Golgi and nucleus labeling and visualization can be done for hundreds of cells in a section, as can serve as a surrogate for filopodia orientation if the correlation between Golgi orientation (measured from the cell nucleus) and filopodial orientation is strong for each cell. Dr. Musy analyzed the relation between Golgi and ectodermal angles (Figure 5.12f), which when binned for different orientations showed a clear bias towards the ectoderm (Figure 5.12g). The correlation between Golgi orientation and average filopodial orientation was very strong (Figure 5.12h): 23 out of 33 analyzed cells had both directions towards the ectoderm, 6 had both features away from the ectoderm (Figure 5.12k), and 4 pointed in

other directions. Thus most cells have a general cellular orientation either towards or away from the ectoderm, and confirmed that the Golgi angle can be used as a good marker for general cell orientation.

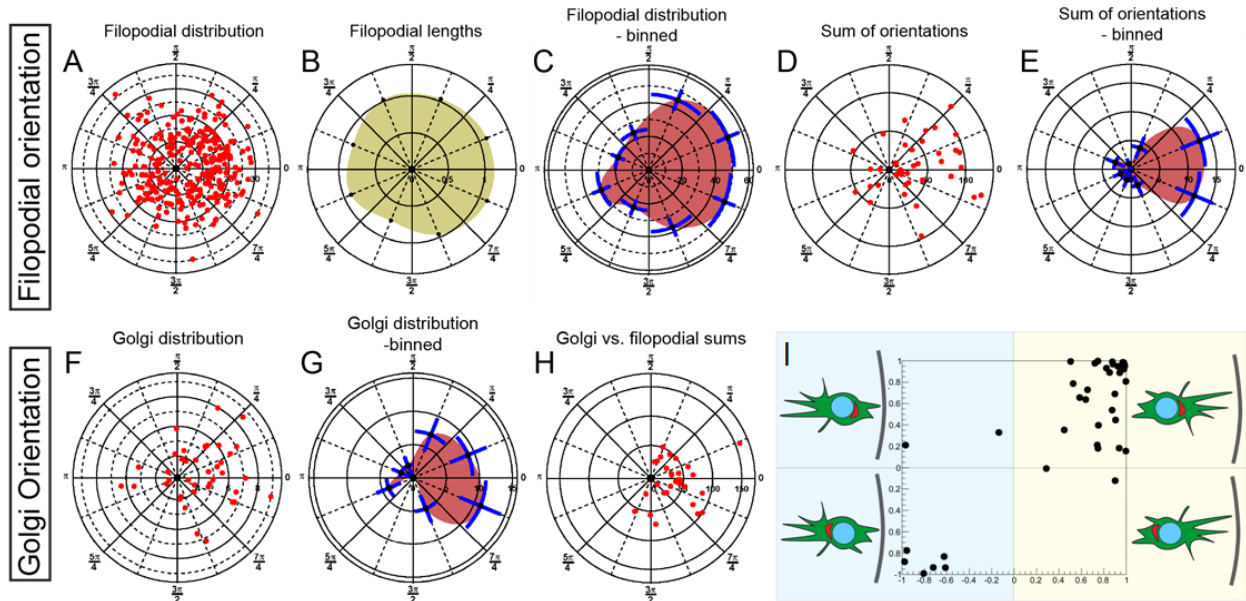


Figure 5.12 – Filopodia and Golgi orientations

(A-I) Angles between the cell nucleus and each filopodium, between the cell nucleus and nearest ectoderm and between the cell nucleus and Golgi (40 cells from 4 different specimens). Angle 0 represents the direction to the closest ectoderm. (A) Filopodia angles plotted in a polar dot-plot. (B) Filopodial lengths were binned in $4/\pi$ bins. (C) Filopodia from (A) represented in a binned polar plot. Filopodia points preferentially towards and away from the ectoderm. (D) Sums of filopodia. Angles of all filopodia in each cell were summed and plotted in a polar dot-plot to represent the general orientation of the cell. (E) Sums of filopodia. As in (D) in binned polar plot. Note the strong bias toward the ectoderm. (F) Golgi angles plotted in a polar dot-plot. (G) As in (F) in binned polar plot. Golgi angles points preferentially toward the ectoderm. (H) Polar dot-plot of Golgi angles. The absence of Golgis in the left two quadrants shows that Golgi angles align with filopodial orientation. (I) Dot-plot is showing correlations between filopodial orientation and Golgi orientation with ectoderm position.

Measurements of a very large number of Golgi orientations across 3 transverse sections of the dorsal, ventral and distal regions of the limb bud (n=1221 cells) confirmed

the predictions of the computer model regarding the cell filopodial orientations: cell orientations were strongly and consistently biased towards the nearest ectoderm. Dr. Sharpe also analyzed the cell division cleavage plane orientation (n=445 cells) and found a weaker but nevertheless consistent bias towards the ectoderm in the dorsal and ventral regions. Interestingly cell cleavage planes in the distal region were randomly oriented bias despite the consistent Golgi angle orientation.

While contractions along the cell **ectodermal** vector improved the shape of the simulated limb bud, it does not reproduce other features of the chick limb bud elongation, with the limb bud bending ventrally later in the simulation (Figure 5.10d).

A new role for the AER-FGF signaling?

In the **ectoderm**-oriented cell contraction simulation, filopodia in the proximal regions are oriented perpendicular to the PD axis, but the distal tip filopodia are oriented parallel to the PD axis. **Tissue** convergence in the PD direction works against the elongation of the bud, rounding it, rather than extending it (as seen in the simulation of distal migration, Figure 5.10b) and causes the limb to bend ventrally.

I therefore defined a *distal* zone of **mesenchyme**, consisting of all **cells** within a distance from the **AER** (pink arrows in Figure 5.10e). The **cells** within this zone have a reduced filopodial persistence, meaning that they only pull their neighbors for a shorter period of time. With this change the developing shape of the limb bud matched the 3D geometry of a HH23 limb bud remarkably well (Figure 5.10f). The model thus predicts

that the shape of the growing chick limb bud results from ectodermally-controlled intercalation, with reduced contraction forces near the distal tip. If the amplitude of contractile forces are uniform in the limb bud, the distal tip acts like a cap opposing extension of the bud. Instead, the tip mesenchyme must be “softer” than the rest of the tissue.

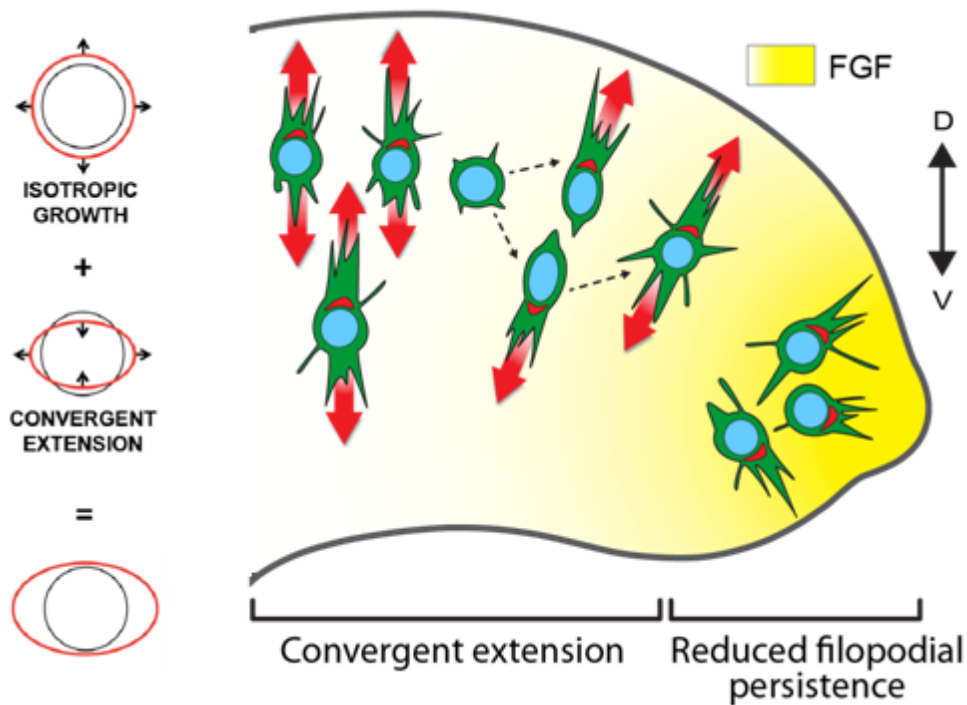


Figure 5.13 – New limb bud growth model

Mesenchymal cells orient toward the closest ectoderm and intercalate. Cell divisions lead to isotropic tissue growth, balancing convergence of the DV axis due to cell intercalation. As a result the limb bud DV extension remains constant while the PD axis elongates. More distal cells under the influence of FGF diffusing from the AER are highly active, with reduced filopodia persistence and exert reduced force on their environment. This allows the limb mesenchyme to be squeezed out and elongate distally.

Since one of the key differences between the tip mesenchyme and the rest of the limb bud is strong FGF signaling, Dr. Sharpe and Ms. Lesnicar-Pucko examined the impact on individual cell of reduced FGF signaling using *in ovo* time-lapse imaging. Cells in SU54020

treated limb buds had 30% less filopodial activity than in matched control cases (0.32 changes/hour rather than 0.46 changes/hour, averaged over 4 different time-lapse experiments). This suggests that filopodia of cells near the AER have shorter lifetime, so the mean number of filopodia exerting forces on their neighbors at any time may be smaller. This observation agrees with previous studies suggesting a PD gradient of cell mobility [44], in which the more dynamically active cells in the distal tip have a higher turn-over rate of transient filopodia.

In addition, as a part of the epithelial to mesenchymal transition program, FGFR1 signaling has been shown to inhibit E-cadherin expression during gastrulation in mice, which lowers adhesion strength and allows cells to become more motile [54]. Interestingly, FGFR1 mutant mice also exhibit limb buds that are shorter in PD direction and broader in DV and AP direction, all implying a role of FGF signaling in limb morphogenesis [55].

Discussion

By combining novel *in-ovo* multiphoton imaging, functional experiments, 3D scanning and a virtual tissue simulation of the developing chick limb bud, we have developed a new hypothesis for how cell level processes control limb bud elongation. The orientation of cell division cleavage plane appears to have little impact on tissue shape. Active migration by a small subset of cells is neither coordinated nor biased along the PD axis, and are therefore unlikely to be of any relevance for limb bud elongation. Instead we propose that oriented cell intercalation is the major driving force for elongation, which

combined with isotropic tissue growth produces growth-compensated convergent-extension (Figure 5.13). Virtual tissue simulations of different hypotheses for the spatial distribution of contractile orientations suggested that cell's intercalation axis should be oriented parallel to the line connecting the cell to the ectoderm. Detailed analysis of Golgi and filopodial orientations confirmed this prediction.

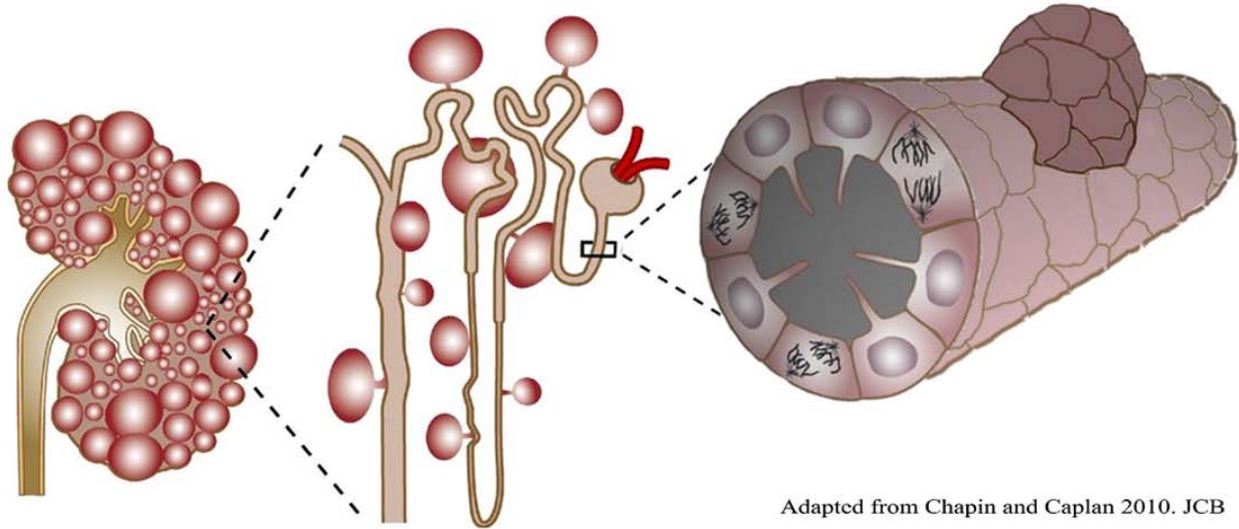
Most excitingly, our model proposes a new morphogenetic role for FGF signaling in the distal limb bud. Although cell intercalation oriented towards the ectoderm by most of cells promoted elongation along the PD axis, ectodermally-oriented convergence by cells in the distal tip would work against elongation – like a cap which is actively contracting the wrong way. The higher cellular motility and reduced persistence of filopodial extensions weakens this cap, allowing elongation to proceed. Intriguingly, our hypothesis agrees with previous suggestions that FGF acts to increase filopodial activity and thus higher cell motility. At the tissue level our hypothesis differs dramatically from previously suggested mechanism for the regulation of limb bud outgrowth. In both the tail bud and limb bud, higher distal motility has been hypothesized to drive elongation through a process of “mass action” of randomly moving cells [44, 56]. Instead we propose that the primary driving force for limb extension is convergent-extension behind the tip, and that distal tissue have reduced contractility to reduce PD tensional stress. In this respect, the mesenchymal tissue is similar to a fluid in which cells are the particles. The higher dynamic movements of cells and/or their lower adhesion ability are equivalent to a localized higher fluidity, or a lower viscosity, which “softens” the tissue.

Our analysis agrees with previous work that FGFs, Wnts and PCP are important molecular pathways controlling intercalation and random motility. However, we differ in their hypothesized role in morphogenesis/ We believe that FGFs loosens the distal tissue, to reduce the net PD contraction forces in the distal tip, and thereby allow the limb bud extend distally. This hypothesis agrees with the previous suggestion that FGFs do not provide directional information, but promote higher cell motility and reduce cell-cell adhesion [55]. Wnt signaling [57-60], specially by Wnt5a can induce cell polarity via non-canonical and canonical PCP pathway [61, 62]. Our experiments contradict the hypothesis that Wnts determine cell orientation in the chick limb bud. The Wnt5a gradient is parallel to PD axis everywhere, while cell orientations in proximal limb bud are essentially DV, except in the distal region where they are PD. For Wnt5a to specify these orientations would require cell in the distal tip to respond differently to Wnt gradients than cells in the proximal region of the limb bud. Instead a general ectodermal signal, such as Wnt3a [63, 64], may allow cells to align their contractile axis parallel to the signaling gradient – both in the dorsal/ventral regions and under the AER.

CHAPTER 6 – POLYCYSTIC KIDNEY DISEASE

While the last chapter provided a direct application of the dynamic links method without any subdivision of the cells into compartments, this chapter will make exclusive use of the dynamic domains methods (concurrent use of both techniques will be exemplified in the next chapter).

So far, most of this thesis dealt with developmental processes as they are observed in the classical model organisms, such as chicken (Chapters 5 and 7) and drosophila (end of Chapter 3), but here, instead, I will momentarily focus on a human disease. However, the basic mechanism underlying it, as my collaborators and I are proposing, share many similarities to developmental processes – and can be thought of as an adult cell retrogressing to a developmental stage – and are best modeled using the methods I have built in Chapter 3.



Adapted from Chapin and Caplan 2010. JCB

Figure 6.1 – Autosomal dominant polycystic kidney disease

Left: cross sectional cartoon of a polycystic kidney. Cyst are shown as red circles. Middle: renal tubule with cysts. Right: close view of the proximal part of the renal tubule with a forming cyst on its top. Image adapted from [65].

The disease

Autosomal dominant polycystic kidney disease (ADPKD) is a benign, but lethal tumor, where cysts accumulate and progressively impair renal function on the adult kidney (Figure 6.1). ADPKD is the prevalent cause of kidney failure in the United States caused by a single cell mutation and in the absence of a FDA approved treatment, the only therapeutic option for patients are dialysis or renal transplantation. All ADPKD cases are related to mutations in PKD1 (85%) or PKD2 (15%), which encode the transmembrane proteins polycystin-1 (PC1) and polycystin-2 (PC2). These mutations result in impairment of multiple signaling pathways including cAMP, mTOR, EGFR [66, 67], that through direct and indirect interactions, affect growth and differentiation of renal epithelial cells [68, 69]. How

ADPKD mutations effect these changes, however, is not understood. The most prevalent hypothesis among biologist/clinicians is that APKD arises from disruptions of ciliary and PCP signaling, but the complex nature of the disease has hampered efforts to define the mechanisms underlying its pathogenesis.

Recent findings

Recent experiments show that ADPKD initiation may involve changes in cell-cell adhesion: Annexin 5 has been shown to form a complex with polycystin-1 that disrupts E-cadherin assembly in the basolateral membrane [70], while primary cultured renal epithelial cells derived from ADPKD kidneys fail to assemble E-cadherin stably in the lateral membrane [71]. These results are consistent with the observation that renal epithelial cell de-differentiation in ADPKD is accompanied by profound changes in cadherin expression and localization (Table 6.1) and affects only a subset of renal epithelial cells. In normal kidney epithelial cells, PC1 and E-cadherin form a complex at the adherens junction, whereas in ADPKD cystic cells the complex is disrupted and both PC1 and E-cadherin remains cytoplasmic [72].

Further support for the role of cadherin disruptions was provided by the recent cadherin-8 experiments by Kher *et al.* [73]. While E-cadherin and N-cadherin are found in both healthy and cystic kidneys, cadherin-8, a transmembrane Type II cadherin, is normally expressed *only* during kidney development, when the renal tubule network is forming

(Table 6.1). Focal introduction of cadherin-8 expressing adenovirus into kidney tubule cultures was sufficient to initiate cyst development at the target sites [73], and the morphology of the cysts closely resembled simple renal cysts seen in microdissections of human nephrons [74]. All cells in the cysts expressed cadherin-8, while nearly none of the cadherin-8 cells remained in the renal tubule. Kher *et al.* proposed that cadherin-8 was downstream from polycystin-1 via PCP and ciliary signaling, but made no mechanistic hypothesis as to how it induces cyst.

	Cadherins in Kidney	Embryonic Kidney	Adult Kidney	Cystic Kidney Disease
Type I	cdh1 (E-cad)(L-cam)	UB[75, 76], DT progenitors[75] upper SSB[77]	DT[78, 79], CD[78]	present, <u>not at surface</u> [71] complexed with PC1[72]
	cdh2 (N-cad)(A-cam)	MM[77], RV[77], CSB[77], lower SSB ¹² , GM[77]	present ⁸ , ↑ in PT[77][80]	present[71], ↑[72]
	cdh3 (P-cad)	GM[75]	DT[80], CD[80], podocyte[81], low GM[75]	↑[82] in some cysts
	cdh4 (R-cad)	GM ^{6,83} , lower-SSB ⁶	GM[80]	slight ↑[84]
Type II	cdh6 (K-cad)	PT progenitors[75] ,mid SSB ⁶	PT[78]	present[82]
	cdh8	UB[85], SSB[85]	absent[73, 85] [73]	↑[73] in cysts
	cdh11 (VN-cad, OB-cad)	MM[75] ⁶	GM[80], mesenchyme[80]	↑[86][82]
7 D	cdh16 (Ksp-cad)	DT[87], CD[78]	tubules[88], DT[87], LH[87] [75]	↓[86]

Table 6.1 – Overview of kidney cadherin expression in development, healthy adults and PKD.

CSB, comma shaped body; DT, distal tubule; GM, glomerulus; MM, metanephric mesenchyme; PT, proximal tubule; RV, renal vesicle; SSB, S-shaped body; LH, loop of Henley; UB, ureteric bud.

Project

That was the situation when Dr. Robert Bacallao – one of the authors of the cadherin-8 experiment – contacted us to do a project together. The initial idea was that since ectopic expression of an extra cadherin was sufficient to cause cysts from tubules in

culture, the mechanism behind it probably involves some kind of change in adhesion properties, likely an increase in cell-cell adhesion. More specifically, we wanted to test if cadherin-8 could induce cysts by i) changes in cell-cell adhesion or ii) focal increase in cell proliferation.

To test these hypotheses we need a 3D multi-cell model of the renal tubule, where we can individually control macroscopic properties of the **cells**, including adhesion strength, cadherin localization, morphology and proliferation rate. In order to do this, a series of preconditions were required: First, we needed a good cyst formation model in the CPM, possibly using a subcellular ODE model for the flux of ions between the cells and the lumen/ECM. Secondly, we needed a good way to represent epithelial cells in the model that allows proper reproduction of cadherin disruptions. And thirdly, we needed a way to connect structural/adhesion changes to proliferation/cyst formation.

Of the listed requirements, only the latter two were ready at the time: the proper representation of the epithelial cells using the dynamic domains model (as presented in Chapter 3); and a *contact-inhibition* (CI) model for cell proliferation that was being developed by Dr. Srividhya Jeyaraman, and which would serve as the link to connect the adhesion/structural changes in the cells to cyst formation. The other requirement, a model for cyst formation, has already been developed in the CPM [89], but it was neither reproducible or compatible with the dynamic domains model, so I choose to build my own version.

3D renal tubule model

The basic unit of the human kidney is the nephron, consisting of a renal corpuscle, where blood plasma is initially filtered, and the renal tubule where nutrients are resorbed and waste is concentrated before being excreted as urine in the collecting duct system. The renal tubule is made of thin, distal and proximal segments, each with unique morphology and complement of transporters. In a shorter scale the distal and proximal tubules can be thought of as a series of short cylindrical segments enclosing a lumen (Figure 6.2a). Each tubule segment, regardless of position in the nephron, can be assumed to be in a quasi-homeostatic state where the influx of ions/liquids to/from the epithelial layer (dashed white arrows in Figure 6.2a) balances the flux of ions/liquids passing from each adjacent upstream tubule segment (solid blue arrows in Figure 6.2a), maintaining the diameter of the lumen roughly constant.

In CC3D I choose to reproduce the distal/proximal segments of renal tubule – which have a similar structure and more regular morphology than the thin segment – as a 15 **cell**-long tube segment with periodic boundary conditions along the **tubule** axis and a circumference of 10 **cells** enclosing a **lumen**, which is modeled as a separate cell type (Figure 6.2a). The quasi-homeostatic state of the lumen is reproduced by maintaining its average volume.

The epithelial cells that compose the renal tubule have well defined apical, basal and lateral surfaces characterized by its functionality and protein concentrations. Establishment and maintenance of apico-basal cell polarity is essential for proper function of the renal

tubule as transport epithelia, while layer integrity is mediated by interaction between opposing lateral cell surfaces, where cadherins and other junctional complex molecules co-localize.

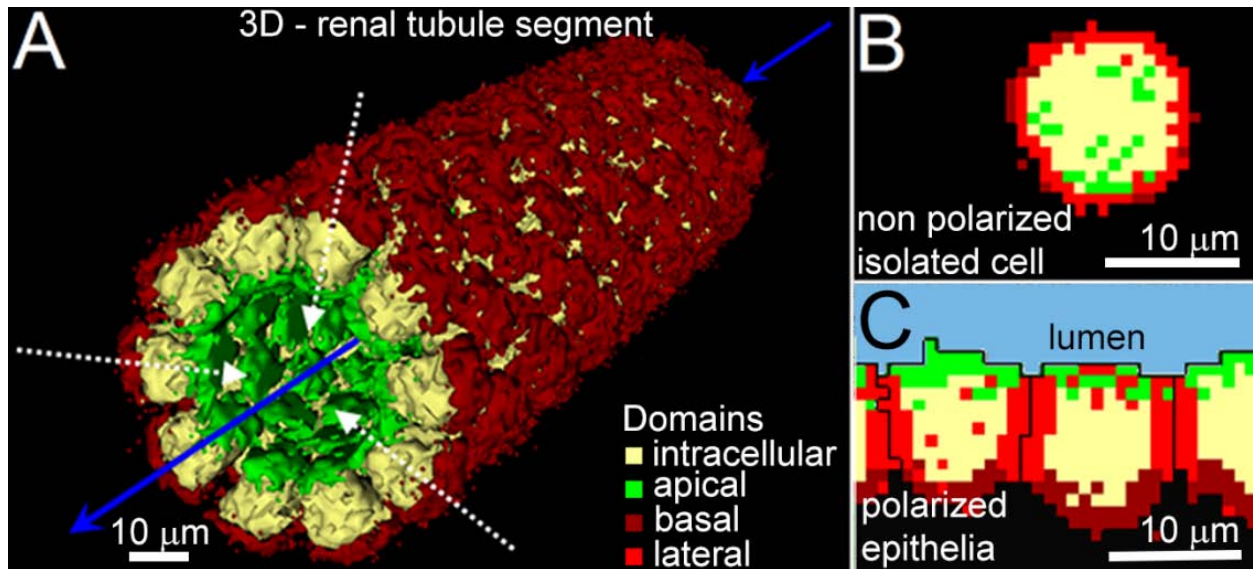


Figure 6.2 – Renal tubule and renal epithelial cell models

(A) Snapshot of our 3D renal tubule segment. Dashed white arrows represent active pumping of ions between the *epithelial* layer and the *lumen* and solid blue arrows represent *lumen* flow through the *tubule*. (B-C) Epithelial cells include 4 compartments representing their *basal* (dark red), *apical* (green), *lateral* (red) and *cytoplasmic* (light yellow) regions. (B) In the absence of any external cues, the surface compartments randomly distribute over the renal epithelial cell boundaries. (C) When the cells are in contact with other cells, *substrate* and/or *lumen* (light blue) the surface compartments arrange themselves accordingly to their adhesive affinities.

I modeled the renal epithelial cells with the dynamic domains model (Chapter 3), and represented them as being composed of three surface compartments, **apical**, **basal** and **lateral**, each representing the above mentioned regions; and one core compartment, the **cytosol**, representing the rest of the cell body. By doing this, I assumed that localization of the surface regions is partially guided by the external environment (Figure 6.2c) and that in

the absence of any external cue surface compartments are randomly distributed on the cell membrane (Figure 6.2b) in accordance with the observation that single cells fail to polarize if left alone [90].

Contact-inhibition of cell proliferation model

Three factors regulate proliferation of epithelial tissues: nutrient availability, growth factors and CI. Given the lack of evidence that growth factors are involved in ADPKD initiation and that *in vivo* and cultured kidney cells have sufficient nutrients, we can assume that CI is the only regulator of cell growth in the renal tubule.

Instead of creating my own CI model, I chose to borrow the one that my colleague, Dr. Srividhya Jeyaraman, was developing at the time. In her original model, which was aimed toward tissue growth in 2D cultures, **cell** proliferation is regulated by two factors: the fraction of **cell-cell** (α) and **cell-substrate** (β) surface contact:

$$(Eq. 6.1) \quad \frac{dV}{dt} = \frac{k}{2} \times \left(\frac{\alpha_c^n (1 - \alpha^n)}{\alpha_c^n + \alpha^n} + \frac{\beta^m}{\beta_c^m + \beta^m} \frac{\beta_c^m + 0.5^m}{0.5^m} \right),$$

where V is the total volume of the **cell**, κ is the maximum growth rate, α_c is the critical value of **cell-cell** contact for growth inhibition, β_c is the critical value of **cell-substrate** contact, and n and m are the hill coefficients that determine the steepness of the inhibition around α_c and β_c , respectively. The 0.5 value on the second term reflects the fact that those terms are normalized and that the model was originally developed for an epithelial cell layer, where

the cells only come into contact with the substrate in the “floor” of the *petri* dish and therefore have a maximum contact of 50% of cell surface. For a case where the cells were immersed on ECM, the numerical value of such factor would be 1.0 and the second term would have a similar form to the first.

Here, instead of using the full phenomenological CI model, I choose to focus only on the **cell-cell** contacts:

$$(Eq. 6.2) \quad \frac{dV}{dt} = k \times \frac{\alpha_c^n (1 - \alpha^n)}{\alpha_c^n + \alpha^n},$$

where V is the total volume of the **cell**, κ is the maximum growth rate, α_c is the critical value of **cell-cell** contact for growth inhibition and n is a hill coefficient.

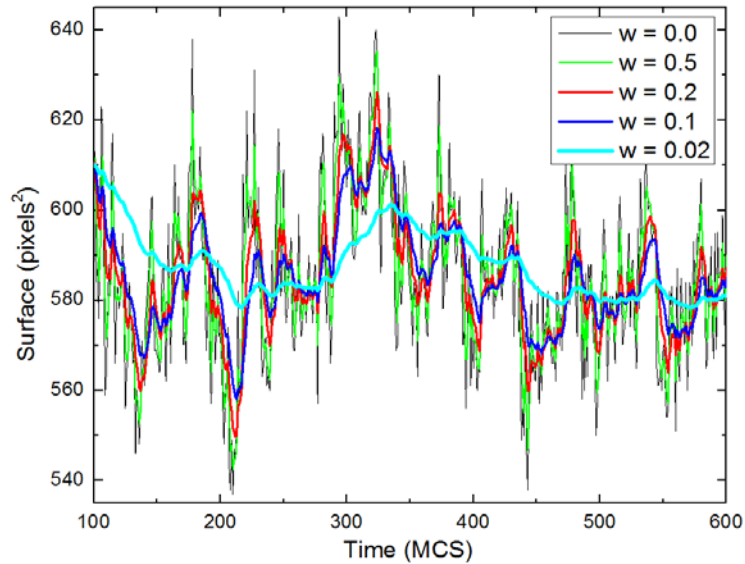


Figure 6.3 – Averaging cell surface measurements

In order to decrease susceptibility to membrane fluctuations the cell surfaces are averaged over time. The last value ($w=0.02$) was used in the simulations.

Due to the CPM formalism, the surface area of a **cell** varies a lot during the course of the simulation, even though its average volume remains constant. This means that a **cell**

whose proliferation is under control of (Eq. 6.2) can switch to back and forth between proliferative and non-proliferative states quite often. In order to avoid such wide oscillations, instead of using the instantaneous **cell-cell** surface value (that is, the value of the **cell** surface at a specific MCS), I choose to average the **cell** surface values in time using the following equation:

$$(Eq. 6.3) \quad \langle S \rangle_t = \langle S \rangle_{t-1} \times w + S \times (1 - w),$$

where w is a number between 0 and 1 that sets the weight between the current surface (S) and the previous averaged surface ($\langle S \rangle_{t-1}$). Figure 6.3 shows the time-plot of the **cell-cell** surface for different values of the parameter w .

I chose a value for α_c that maintains the original wild type **cells** on the **tubule** epithelial layer in an inhibited state. As is can be seen on Figure 6.3, even the use of (Eq. 6.3) to calculate **cell** surface leaves some fluctuations around its mean value. Therefore I set a value for α_c to be below $\langle \alpha \rangle - 2 * \text{std}(\alpha)$, where $\text{std}(\alpha)$ is the standard deviation from the mean value of the **cell-cell** contact surface for the modeled epithelial **cells** ($\langle \alpha \rangle$).

Cell divisions

Under the classic CPM formalism, **cell** divisions are implemented by crossing a plane at a specific, or random, direction through the **cell's** center of mass (which usually coincides with its geometrical center) and assigning all **cell's** lattice sites on one side of the plane to the daughter **cell**. Such a recipe is problematic when using the dynamic domains model

because the **cell** compartments are, in principle, randomly distributed. Even if the compartments are already segregated due to interaction with the external environment, implementation of the old division algorithm is still challenging. and use of an alternative approach is preferable.

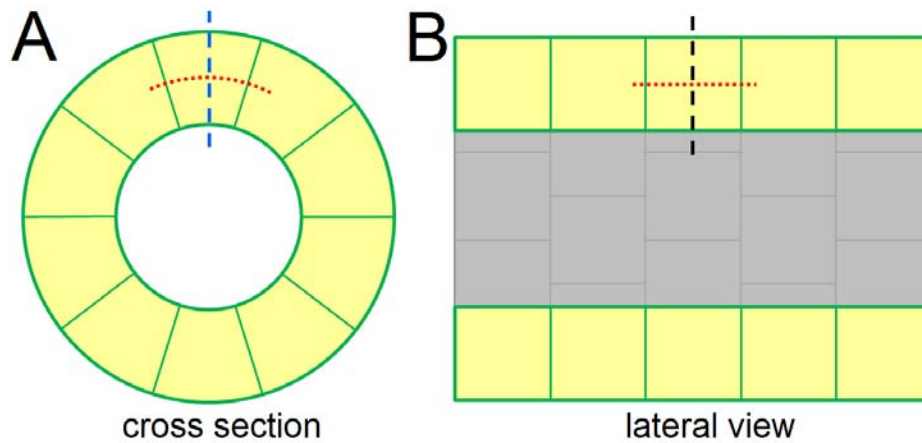


Figure 6.4 - Division planes

(A) Cross section and (B) lateral view of the renal tubule. Red dotted lines represent division plane parallel to the plane of the epithelium, while dashed lines represent division planes orthogonal to the plane of the epithelium. Blue dashed line represents division planes parallel to the tubule axis and black dashed line represent division planes parallel to the tubule radius and orthogonal to its axis.

An alternative approach is to break the division procedure into 3 different steps. First, we merge all cell compartments into one compartment (here, all the surface compartments join the **cytosol**). Next, we proceed as before and cut the now single-compartment **cell** into two halves according to some predefined orientation. Finally, we randomly distribute the other compartments inside the volume of each daughter **cell** and let them rearrange in the next MCS according to their immediate external environments.

Such an approach not only solves all the difficulties of the redistribution of the **cell** compartments into the new daughter **cells**, but mimics what actually happens during the

division of real epithelial cells, where they first unpolarize, round up, divide and later regain their polarity.

For any given **cell** in the renal tubule, division can be oriented in three main directions: parallel to the plane of the **epithelium** (Figure 6.4, red dotted lines), parallel to the **tubule** axis (Figure 6.4a, blue dashed line), or parallel to the **tubule** radius and orthogonal to its axis (Figure 6.4b, black dashed line). Division planes on single epithelial layers, especially on tubular structures, are usually orthogonal to the plane of the epithelium and guided by PCP signaling, when present. Since I choose to not include PCP in this model, **cell** division planes, while always orthogonal to the plane of the **epithelium**, are randomly oriented with respect to **tubule** axis.

Cystogenesis model

While tubule diameter is essentially constant in time, the lumen of new cysts sprouting from the tubule wall grows in time. Many factors regulate cyst size, including matrix and cell elasticity, stretch-induced cell proliferation and osmotic pressure due to differences between external and internal ion concentrations.

Because our primary interest is the onset of cyst formation from the renal tubule wall, I choose to model cyst formation and size regulation in simple terms, as was done by Engelberg *et al.* [89], rather than the more detailed continuum models found elsewhere [91, 92]. Cystic **lumen** is created at the intersection of 3 **apical** compartments whose **cells**

are not currently in contact with any existing **lumen**. Once a **lumen** is created, its expansion/retraction is regulated by the following equation:

$$(Eq. 6.4) \quad \frac{dV_1}{dt} = k_1 \times (N_{\text{cells}} - k_r \times S_1) - f(N_{\text{cells}}, J, T, \lambda_{\text{volume}})$$

where V_1 is the **lumen** volume, N_{cells} is the number of **cells** in contact with the lumen, S_1 is the surface area of the **lumen**, k_r is a retraction/leakage constant and k_1 sets the time scale of growth/shrinkage. The extra term f accounts for the additional pressure from the surrounding epithelial **cells** that resist lumen expansion, which depends on the number of **cells** (N_{cells}), their adhesivity (J) and elasticity ($T, \lambda_{\text{volume}}$) (see Chapter 2). The effect of external pressure on the growth of individual **cells** is negligible and was omitted from (Eq. 6.2).

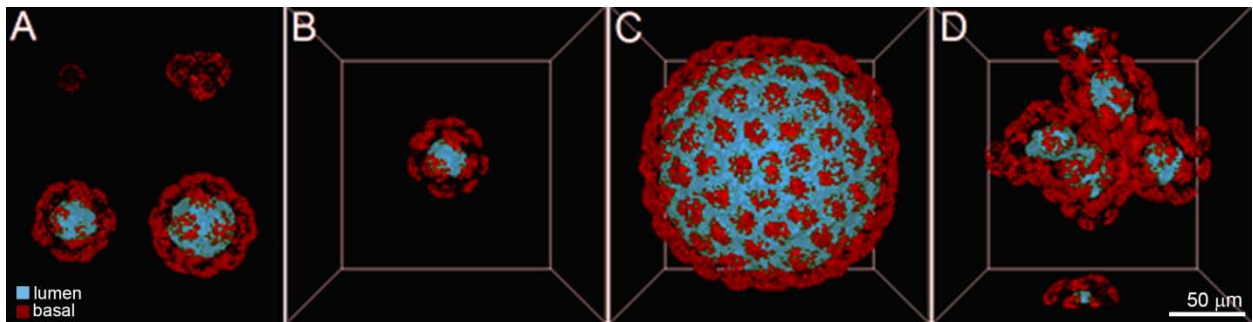


Figure 6.5 – Cystogenesis simulation

(A) Typical cyst formation simulation starting from a single cell. Snapshots at 25, 2000, 5000 and 15000 MCS. (B) Small cyst phenotype, (C) big cyst phenotype, (D) multiple-cyst phenotype. (B-D) Snapshots taken at 30000 MCS. Lumen in light blue, basal compartments in dark red; all other cell compartments made invisible for visualization purposes.

For a simulation beginning with a single isolated **cell**, the **cell** proliferates and form a **cyst** (Figure 6.5a). **Cyst** morphology depends on the balance between **lumen** growth (Eq.

6.4) and **cell** properties such as **cell** proliferation (Eq. 6.2) and the relative adhesion strengths between **cells** and between **cells** and **substrate**. Small simple **cysts** form when **cell** proliferation is slow and adhesion between the **cells** is strong enough to offset the pressure from **lumen** growth (Figure 6.5b). Large simple **cysts** form when the adhesion between **cells** is weak and/or **cell** proliferation is increased (Figure 6.5c). Complex multiple **cyst** morphology is obtained when adhesion between **cells** is weak and the rate of **lumen** growth is high (Figure 6.5d). This leads to frequent collapse of the spherical **cysts** due to **lumen** leakage resulting in formation of multiple **cysts** or multi-lobed **cysts**.

Cadherin-8 knock-in model

In our *in vitro* renal tubule culture assay, kidney epithelial cells were cultured under conditions that supported tubule formation. Then single cells in the tubules were microinjected with a cadherin-8 adenovirus construct and subsequently cadherin-8 expressing cysts developed at those locations [73]. To develop an *in silico* model of our cadherin-8 knock-in experiments, I started the simulation with a preformed, stable tubular structure as described in Figure 6.2, and chose one of the **cells** in the simulated tubule as the target of the simulated cadherin-8 adenovirus microinjection.

Ectopic expression of a cadherin in an epithelial cell can change its behaviors in many ways: it can change the strength which it adheres to other cells, specificity of cell-cell adhesion and other cell properties such as rates of proliferation and migration [93]. Here I

systematically explored the ways in which ectopic expression of cadherin-8 can interfere with cell-cell adhesion and CI.

Cell-cell adhesion is disrupted by either changes in the strength of cadherin adhesion of the specific cadherin isotype or the number of functional cadherins present in the cell membrane. I simulate the first by changing the adhesion energy between the cells (J) and the latter by changing the size of the **lateral** surface domain. CI disruptions are characterized by lowered, sensitivity of cell proliferation to inhibition by cell-cell contacts [94]. In the model this is simulated by changing the critical ratio of **cell-cell** contact area (α_c) in (Eq. 6.2).

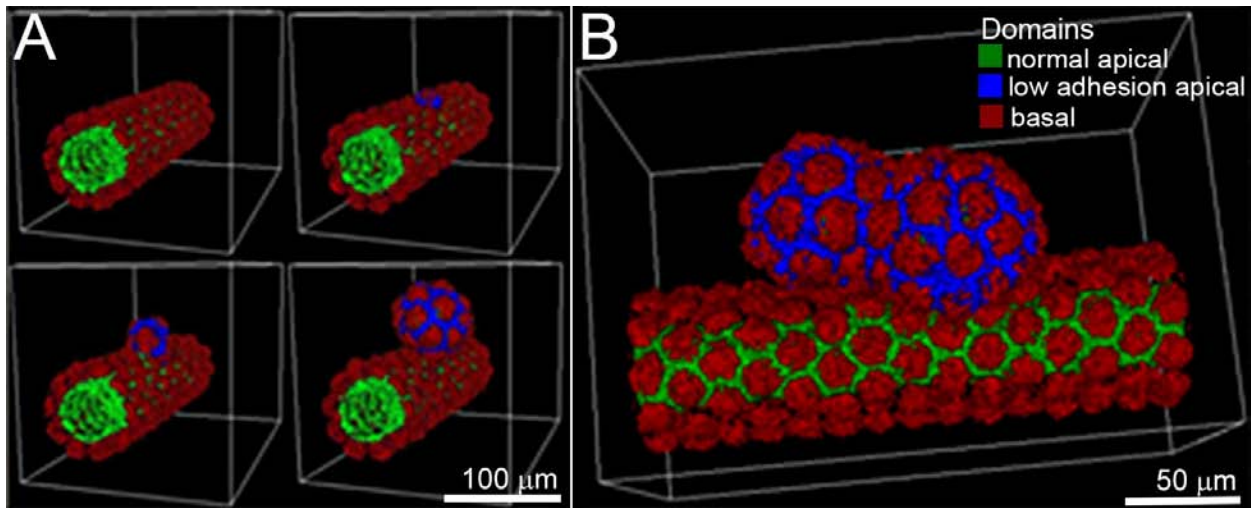


Figure 6.6 – ADPKD simulation

(A) Starting from a stable tubular structure (first panel) we modeled cadherin-8 phenotype by changing the macroscopic properties of the microinjected cell (blue cell in second panel). Increased surface tension between wild type and cadherin-8 expressing cells leads to budding out, deactivation of contact-inhibition regulation, proliferation and formation of a single ectopic cyst. (B) 3D view of a similar ADPKD simulation (identical parameters) showing two formed cysts. (A-B) Lumen in dark green, basal compartment in dark red; cadherin-8 expressing lateral compartment in blue; all other cell compartments made invisible for visualization purposes.

Cadherin-8 acts by reducing normal cell adhesion

I first modeled changes in cell-cell adhesion by varying the adhesion strength between the microinjected and normal **cells**. We found that no level of increase in the relative **cell-cell** adhesion between target **cell** and normal surrounding **cells** was sufficient to induce **cyst** formation. The model, instead, predicts that a five-fold decrease in the strength of wild type and target **cell** adhesion will lead to partial budding out of the cadherin-8 microinjected **cells** from the renal tubule wall. The increased exposure of the affected **cell** to the extracellular **matrix** eventually turns off the CI mechanism, leading to proliferation of cadherin-8 expressing **cells** at the margin of the renal **tubule** and the formation of **cysts** (Figure 6.6).

Next I tested whether changes in the amount of functional cadherin present in the membrane could initiate cyst formation. To do this I changed the size of the **lateral** surface of the target **cell**, while maintaining the cadherin-cadherin adhesion strength. Simulations with increased **lateral** surface failed to lead to **cyst** formation, while a reduction of **lateral** surface of the target **cells** by a factor of three from normal was sufficient to give rise to cysts in a similar way as done by decreased **cell-cell** adhesion strength.

Together these results predict that adhesion disruptions from ectopic expression of cadherin-8 can only lead to cystogenesis by either a reduction in cadherin binding strength between perturbed and wild type renal cells or a reduction in the number of functional cadherins on the cadherin-8 expressing cell.

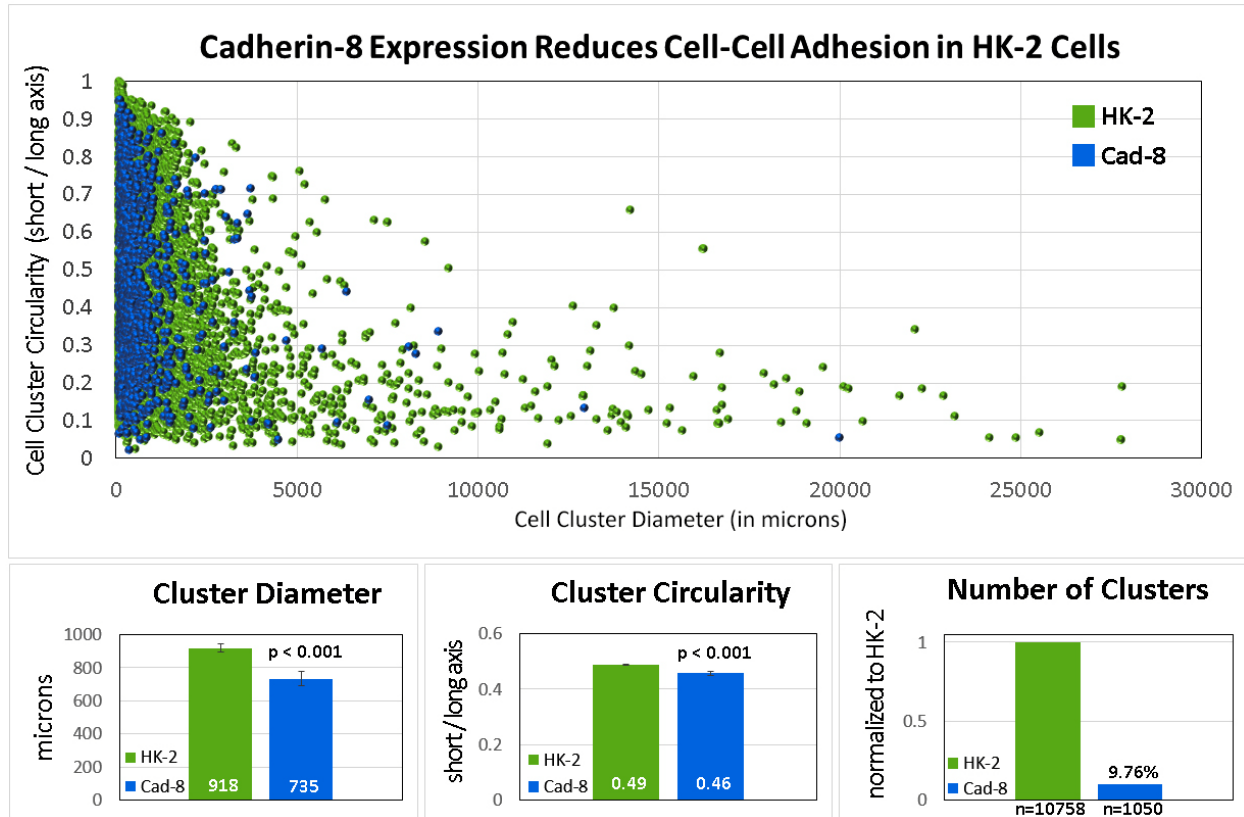


Figure 6.7 – Cadherin-8 expression reduces cell-cell adhesion

Using hanging drop assays, cell-cell adhesion was compared in HK-2 cell and in HK-2 cells ectopically expressing cadherin-8. Fused aggregates were counted and their diameter and circularity were measured using FIJI-ImageJ.

To test this prediction experimentally, Dr. Clendenon and Dr. Bacallao used hanging-drop assays [95, 96] to measure relative cell-cell adhesion strengths of wild type HK-2 cells (a normal human kidney cell line) and HK-2 cells transduced with cadherin-8. In hanging drop assays HK-2 cells predominantly formed tight spherical aggregates while HK-2 cells with ectopic cadherin-8 expression most frequently failed to aggregate, with aggregates that did form being smaller with cells protruding from the surface and sometimes forming groups that were only loosely associated. These results show that

ectopic expression of cadherin-8 leads to decreased cell-cell adhesion in accordance with our model predictions (Figure 6.7).

Adhesion vs proliferation ADPKD initiation patterns

Besides changes in cell-cell adhesion, ectopic cysts might also form by direct disruptions in CI of proliferation alone. To test this in the *in silico* model I changed the CI mechanism of the target **cell** (by changing the values of α_c in (Eq. 6.2)), while holding the adhesion parameters between perturbed and wild type **cells** constant. Our model found that both mechanisms generate **cysts** made of cadherin-8 expressing renal epithelial cells only, with no wild type renal **cells**, despite the fact that that both **cell** types are motile and free to mix.

The emergent outcomes from the two modeled disruptions, reduced cell-cell adhesion and CI of proliferation, match the observed phenotype of cadherin-8 knock-in experiments, where cysts are formed of cadherin-8 expressing cells only (Figure 6.6c) and are consistent with data showing that cell turnover is infrequent in normal adult renal tubule and increased in ADPKD patients [97]. The model found, however, that the temporal evolution of the cysts is different in both cases.

Cysts that formed from loss of adhesion (Figure 6.8a) began with a **cell** protruding out into the **ECM** from the epithelia of the **tubule**. **Cyst** formation then proceeded entirely outside of the **tubule**, with few common **cells** between the forming **cyst** and **tubule** maintaining a neck-like connection.

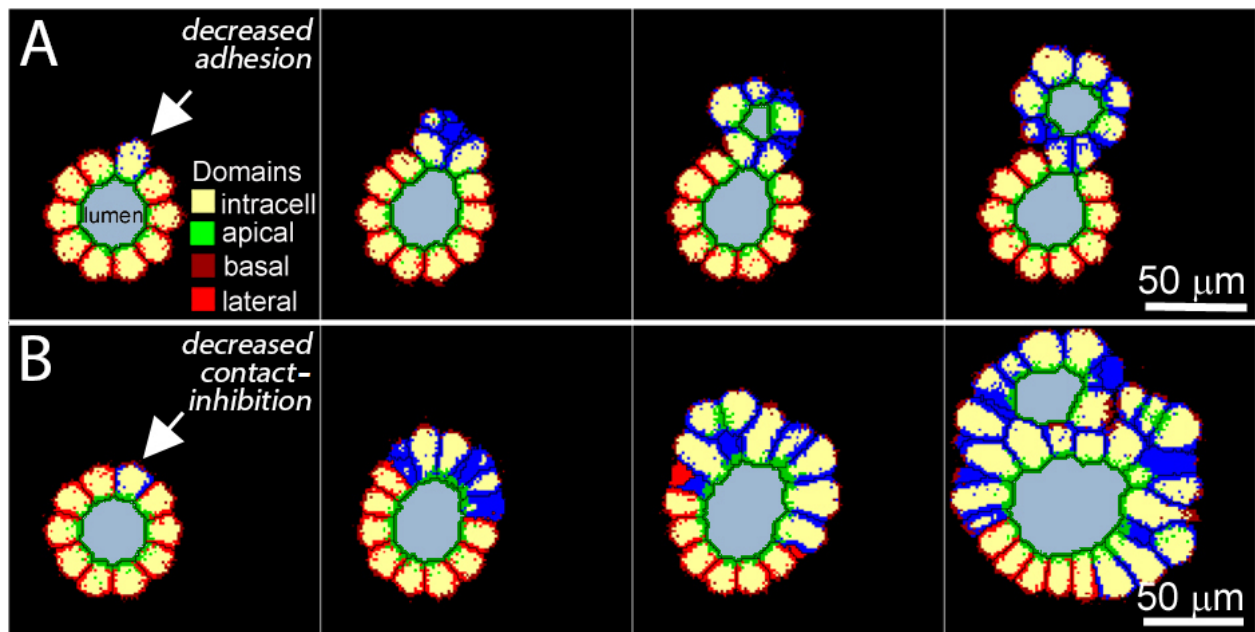


Figure 6.8 – ADPKD initiation patterns

Shown are 2D slices from 3D simulations. (A) Lower cell adhesion leads to proliferation of perturbed cells outside the renal tubule, while (B) changes in proliferation rate through disruptions of contact-inhibition lead to lateral spread of cells before cyst formation.

Cysts that formed from disrupted CI in the target cell first formed a patch of cadherin-8 expressing daughter cells within the epithelia of the tubule which subsequently buckled out to form a cyst (Figure 6.8b). We thus predict that the effects of ectopic expression of cadherin-8 can be distinguished by the temporal evolution of the cysts.

To test this Dr. Bacallao did immune-fluorescence images of cysts stained for cadherin-8 in his *in vitro* assay (Figure 6.9). He found that the morphology of simulated cysts formed by reduction of adhesion (Figure 6.8a) matched that of cysts formed from tubules *in vitro* and also closely resemble the morphology of isolated simple renal cysts in microdissections of human nephrons [74]. This, combined with the hanging drop analysis (Figure 6.7), confirms that ectopic expression of cadherin-8 in renal cells induces cyst

formation by reductions in adhesion between normal renal epithelial cells and cadherin-8 expressing cells.

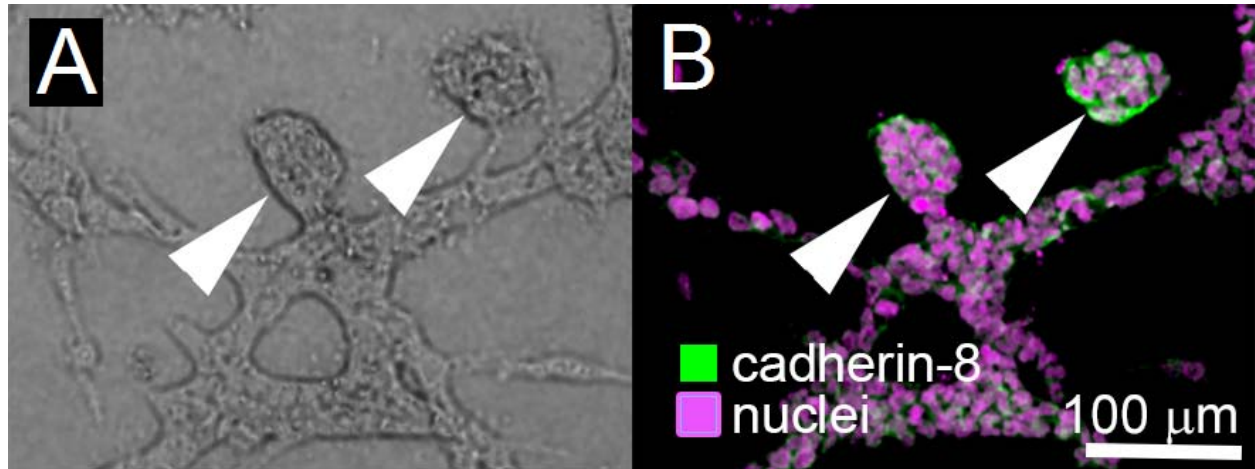


Figure 6.9 – In vitro cyst formation pattern

Immuno-fluorescence images of cysts (arrows) stained for cadherin-8 (green). (A) Phase-contrast image. (B) Same view as in (A) labeled for nuclei (pink) and cadherin-8 (green).

While cyst morphology formed by decreased CI of proliferation did not match that of ectopic cadherin-8 *in vitro* experiments, it does closely resemble the complex saccular dilations found in microdissections of human nephrons [74]. This suggests that *in vivo*, both decreased adhesion and decreased contact inhibition contribute to cyst formation.

Conclusion

The combined computational and experimental results provide a mechanistic account for how changes in cell behaviors can initiate cyst formation on an otherwise stable structure. We hypothesize that when cadherin selection is altered in a specific way (here by

addition of a type II cadherin) the resulting changes in adhesion between perturbed and wild type cells and CI of proliferation are then sufficient to initiate cyst formation.

How exactly the expression of cadherin-8 disrupts perturbed and wild type adhesion, however, is still not understood. In the model, both reduction of cadherin-cadherin binding strength and reduction of the number of functional cadherins give the same qualitative results. Therefore the exact mechanism can only be selected if one of these processes could be reproduced or measured experimentally under the same conditions.

Although this work provides the first biomechanical explanation of how ectopic cadherin-8 expression can initiate cystogenesis, the connection between the two known polycystic mutations in ADPKD and cadherin type switching remains to be explored. Although this is mainly a systems-biology problem, the model presented here provides a platform for linking the subcellular networks known to be affected by polycystin mutations with those driving selection and function of junctional complex molecules.

CHAPTER 7 – SOMITES *WITH* AND *WITHOUT* A CLOCK

While in the last two chapters I showed that the two developed simulation techniques (dynamic domains and dynamic links) can be used to successfully model biological processes by themselves, here I show that they can be combined into a single simulation to model somitogenesis in an early vertebrate embryo.

In the extending limb bud project, an external signal – the putative morphogen from the ectoderm – lead to the asymmetric cell forces which maintained tissue shape during growth. In Chapter 4, where the model for cell intercalation was developed, the same forces were used to break tissue asymmetry, but in both cases, cell asymmetry was set externally.

In contrast, in the polycystic kidney disease project, cell asymmetry results from local interactions. While the cyst formation model – either from a pre-formed tubule or by itself

– was capable of generating a large structure, it was a homogenous one, and the individual asymmetry of each cell did not translate into a tissue wide asymmetry.

In the model showed at the end of this chapter cell behavior asymmetry is set internally and by direct contact with other cells, which in turn generates a tissue wide asymmetry leading to a repeating, regular pattern of tissue structure. Such pattern was believed to be set externally, but here we show, for the first time, that it can result from a self-generated, self-organized process.

What is somitogenesis?

Somitogenesis is the earliest evident segmentation process that occur during the development of vertebrate embryos [98]. During somitogenesis, an initially homogeneous mesenchymal tissue – the *presomitic mesoderm (PSM)* – is patterned/subdivided into periodic clusters of epithelial tissue – the *somites* –, consisting of a few cells, that later will give rise to the ribs, vertebrae and striated muscle. Somite formation is regular in both time and space, with a pair of somites (one on either side of the notochord, see Figure 7.1) forming and separating from the anterior of the PSM approximately every 30 minutes in zebrafish, every 90 minutes in chick, and every 120 minutes in mouse.

The striking spatio-temporal periodicity and dynamic morphology of somitogenesis is believed to depend on mechanisms operating at a range of scales, as well as interactions between scales: genetic and protein oscillations and regulatory networks at the *subcellular*

scale [99], *juxtacrine* (contact-dependent) and *paracrine* (secretion-dependent) cell-cell signaling [100, 101], adhesion-driven cell-cell interactions at the *cellular* and *multicellular* scales [102, 103], and PSM-spanning morphogen concentration gradients [104, 105] and gene expression patterns [106] at the *tissue* scale (Figure 7.3).

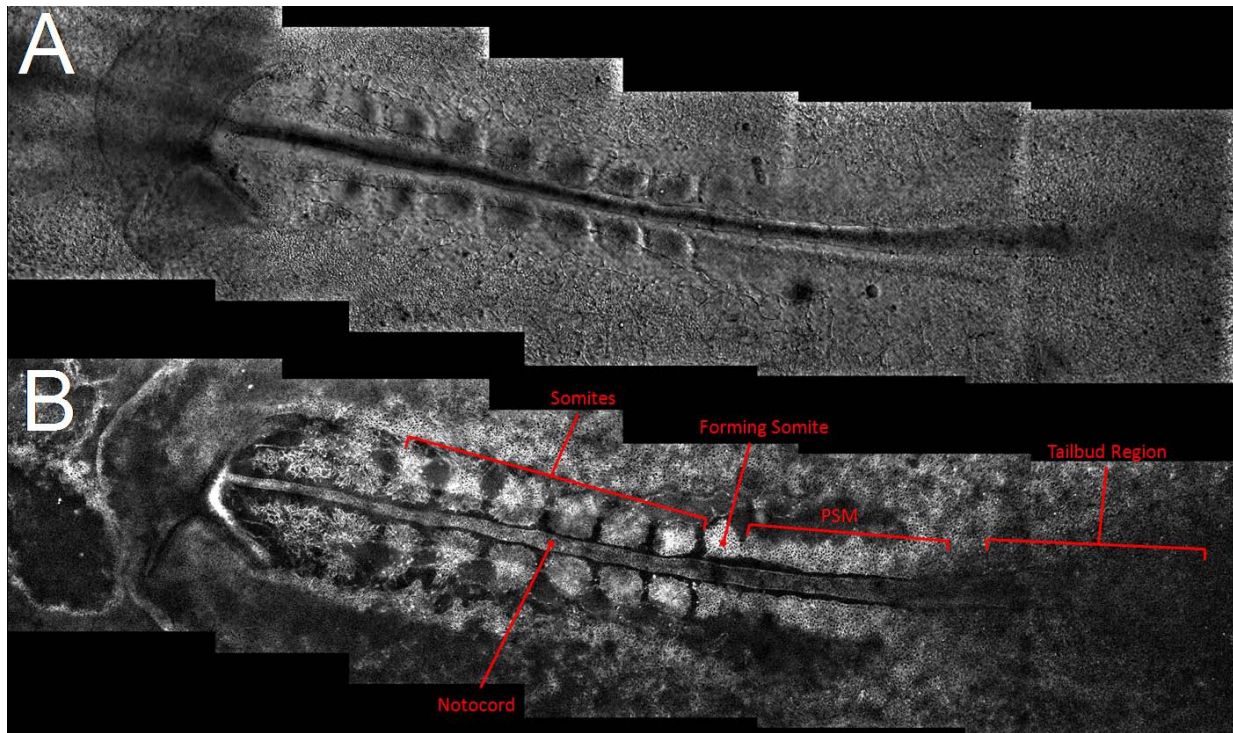


Figure 7.1 – Chick somitogenesis

(A) DIC image of a live HH Stage 10 chick embryo. (B) The same embryo, labeled with *Lens culinaris agglutinin-FITC*. Anterior (head) at left, posterior (tail bud) at right.

All these processes/scales are believed to interact and be necessary for somite formation according to the *clock-and-wavefront* model of segmentation. This hypothesis was initially proposed by Cooke and Zeeman in 1976 [107] and describes a smoothly varying intracellular oscillator (the *segmentation clock*) that interacts with a posterior-propagating front of cell maturation in the PSM (the *wavefront*) to divide the PSM into periodic segments at regular spatio-temporal intervals (Figure 7.2). Since its proposal, many

experiments have identified suitable candidates for both the clock and wavefront components in the PSM. This has boosted the model's popularity and led to a family of clock-and-wavefront models at all abstraction levels. These models differ in detail but adhere to the idea that an intracellular segmentation clock and a posteriorly advancing wavefront establish and coordinate the temporal and spatial periodicity of somitogenesis.

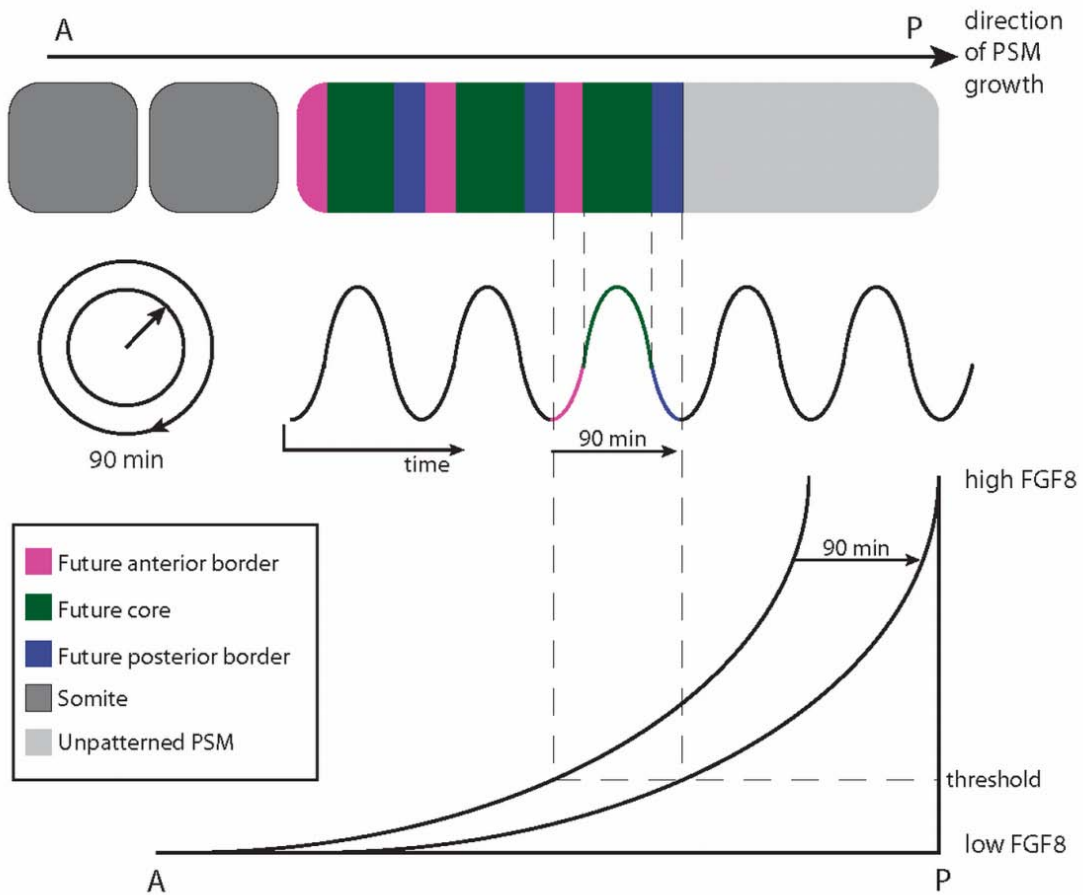


Figure 7.2 – Schematic version of the clock and wavefront hypothesis

The position of a threshold value along the retreating FGF8 gradient acts as a determination front past which cells are able to sense the phase of their segmentation clocks. Once past the FGF8 determination front, a cell is destined to become a somitic cell whose properties are determined by the phase of its segmentation clock upon encountering the determination front.

Do we really know how somites form?

The conceptual clock-and-wavefront biological model is not a complete explanation of somitogenesis. It lacks molecular explanations for the origin and behavior of the clock and wavefront; how the intracellular segmentation clocks interact between cells to maintain synchrony and phase-locking despite molecular noise, cell movement and cell division; how the clock and wavefront interact to induce determination and differentiation; how oscillating segmentation clock molecules cause stable expression and localization of structural proteins like cell adhesion molecules; and, finally, how the distribution of structural molecules leads to the post-differentiation dynamics of segmentation and epithelialization.

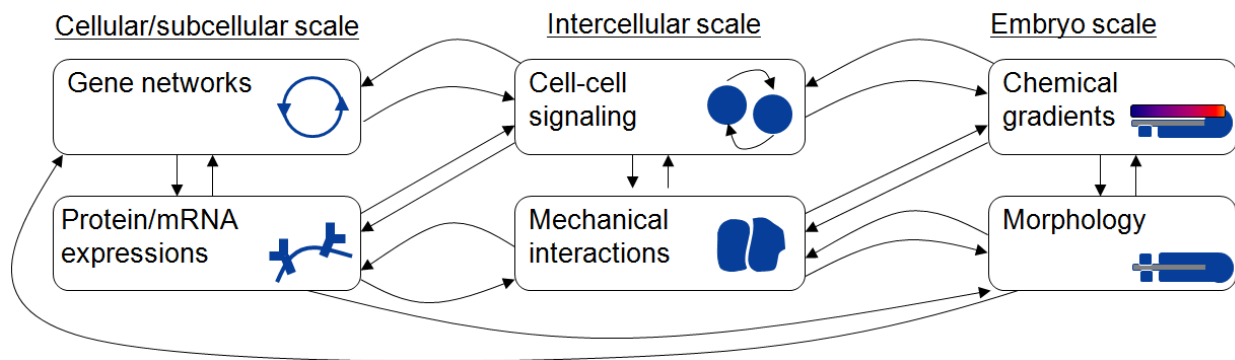


Figure 7.3 – Clock and wavefront complexity

Despite its apparent simplicity, the clock and wavefront hypothesis actually involves the cross interaction of many biological process happening at different scales.

A variety of mathematical submodels address one or two of these aspects: *segmentation clock submodels* address protein and mRNA oscillations within cells [108, 109], *synchronization submodels* address crosstalk, synchronization and phase-locking between neighboring cells' segmentation clocks [101, 110], *determination front* and *differentiation*

submodels address the spatial progression of PSM maturation and somite formation [104, 111, 112], *clock-wavefront readout submodels* address the signaling and genetic regulatory events through which the segmentation clock and determination front interact to segment the PSM [113, 114], and *cell adhesion submodels* address the cell mechanics behind the morphological events during somite formation [103].

Until recently, those mechanisms of somitogenesis have been studied independently by both mathematicians/modelers and experimentalists. So, even though all the clock and wavefront ingredients have been shown to be present in experiments on chick, zebrafish and mouse, we still do not know if they are consistent with each other and, if combined together, are capable of reproducing somite formation.

A multi-scale model of somitogenesis

While we lack experimental proof that the clock-and-wavefront submechanisms operating together produce somites, an analogous investigation using the current mathematical models of the clock-and-wavefront ingredients is practical. That is what Dr. Susan Hester and I set to do six years ago [2]. Using the CP/GGH model, we built a composite clock-and-wavefront 2D model including submodels of the intracellular segmentation clock, intercellular segmentation clock coupling via Delta/Notch signaling, an FGF8 determination front, delayed cell differentiation after determination, clock-wavefront readout and differential cell-cell adhesion-driven cell sorting.

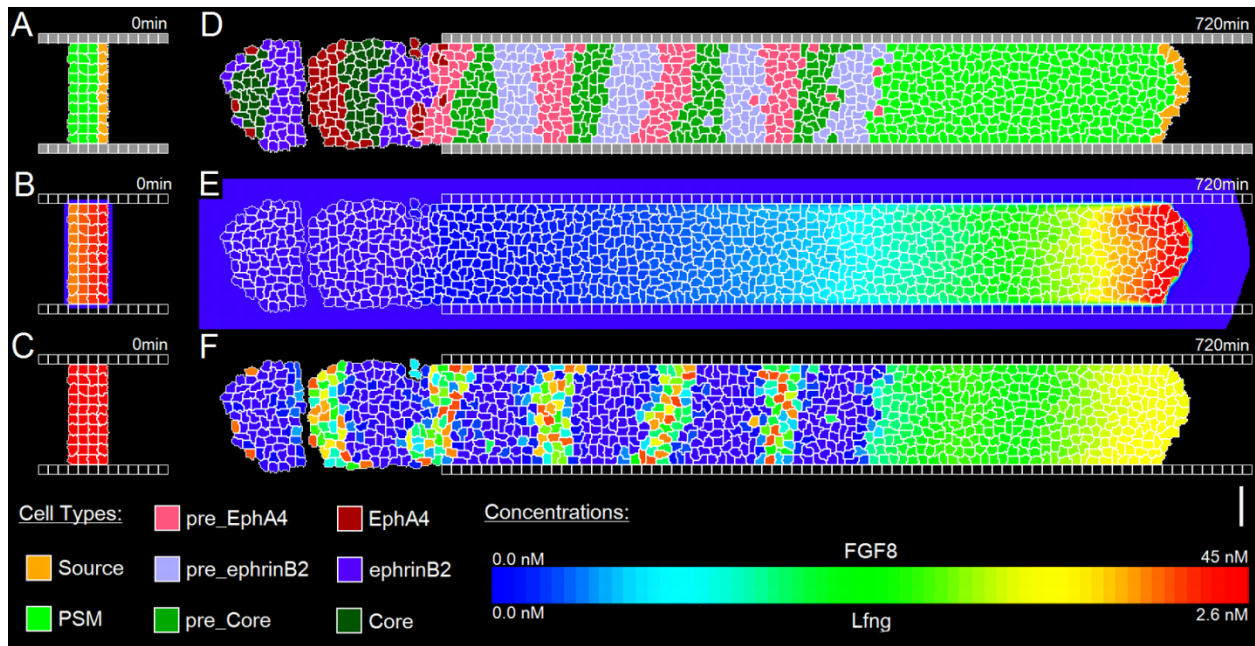


Figure 7.4 – Multi-scale model of somitogenesis via the clock and wavefront mechanism

(A-C) Initial model conditions, visualizing (A) cell types, (B) [FGF8] and (C) [Lfng]. Not shown: initially, the constraining walls extend the full AP length of the simulation. (D-F) The modeled PSM after reaching its full length, visualizing (D) cell types, (E) [FGF8] and (F) [Lfng]. The patterns present in the full-length PSM arise spontaneously from the model's behavior. The first, ill-formed somite to the anterior (left) of the full-length PSM results from the model's non-biological initial conditions.

We model somitogenesis beginning after formation of the first four somites, when the PSM has already grown to the length it will roughly maintain throughout formation of the next 22-24 somites. To avoid biasing the evolution of the model with a pre-imposed pattern, we initialize the model with only four layers of **PSM cells** between two columns of confining **Wall cells** that represent the medial and lateral structures confining the PSM (Figure 7.4a-c). Posterior to the **PSM cells** we added a single layer of **Source cells** that constantly grow and divide, thus feeding the simulated **PSM** with new **cells**.

Source and **PSM cells** in our biological model secrete FGF8 and Wnt3a proteins that diffuse and decay in space (Figure 7.4b,e). Each **cell** has an internal concentration of $fgf8$ mRNA that determines the **cell's** FGF8 secretion rate. **Source cells** have a constant concentration of $fgf8$ mRNA ($mfgf_0$) that **PSM cells** inherit from their parent **Source cell**. In **PSM cells**, $fgf8$ mRNA decays exponentially in time with a decay constant k_{mfgf} :

$$(Eq. 7.1) \quad \frac{d}{dt}[mfgf_{cell}] = -k_{mfgf} \times [mfgf_{cell}].$$

In vivo, $fgf8$ mRNA is translated into FGF8 protein in the cell before being secreted by the cell into the intercellular space, where it binds to receptors on cell membranes and induces the FGF signaling cascade within cells. We simplify this process in our model by setting **PSM** and **Source cells'** FGF8 secretion rate directly proportional to their intracellular concentrations of $fgf8$:

$$(Eq. 7.2) \quad S(\bar{x}) = s_{fgf} \times [mfgf_{cell(\bar{x})}],$$

where \bar{x} is a field lattice site corresponding to a cell lattice site occupied by the **cell**, and each **PSM** and **Source cell** secretes FGF8 from every lattice site it occupies.

A second simplification is that **cells** in our model do not impede diffusion (**cells** and FGF8 co-occupy space), and do not consume FGF8 during signaling, so the local FGF8 concentration obeys the two-dimensional diffusion equation with secretion from (Eq. 7.2):

$$(Eq. 7.3) \quad \frac{d}{dt}[\text{FGF8}] = D_{fgf} \nabla^2[\text{FGF8}] - k_{fgf}[\text{FGF8}] + S(\bar{x})$$

Finally, we simplify FGF8 signaling by not modeling the interaction between extracellular FGF8 and cells' transmembrane FGF receptor proteins. Biologically, cells in the PSM generally express FGFR1 [100]; in our computational model, we assume that intracellular FGF signaling is proportional to the local FGF8 concentration and is not affected by the concentration of FGFR1 on a cell's surface.

To reduce computation time, and because no experimental evidence suggests a more complex Wnt3a profile, we did not model independent *wnt3a* mRNA transcription and Wnt3a translation, secretion, diffusion and decay, but set the local Wnt3a concentration proportional to the level of *fgf8* mRNA:

$$(Eq. 7.4) \quad [Wnt3a_{\text{cell}}] = C_{f2w} \times [mfgf8_{\text{cell}}].$$

We set the level of Wnt3a proportional to the concentration of *fgf8* mRNA rather than the concentration of FGF8 for computational simplicity and because its very short diffusion length [105, 115] effectively restricts it to the secreting cell's immediate neighborhood.

Our model somite clock extends the kinetic equations proposed by Goldbeter and Pourqu   [108] to include Delta/Notch cell-cell synchronization from Lewis [101] and our own hypothesis for additional connections necessary for proper cell-cell synchronization (Figure 7.5). In a simulation of a single self-coupled cell (*i.e.*, the cell receives an incoming Delta signal equal to its outgoing Delta signal, as it would in an homogenous tissue), our clock model produces oscillations in *Lfng*, *Axin2* and *Dusp6* with the qualitative phase

relationships seen *in vivo* (Figure 7.6a). When we simulate multiple model segmentation clock networks with different initial phases coupled via Delta/Notch signaling, they phase lock with the same phase while maintaining the desired intracellular FGF-Wnt-Notch phase relationships.

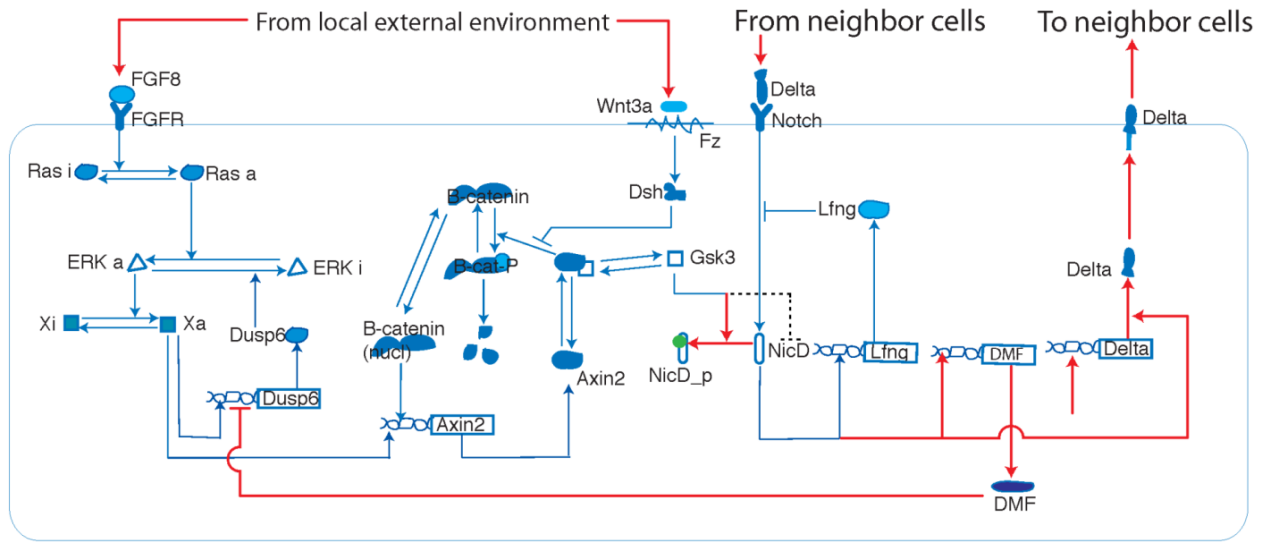


Figure 7.5 – Modeled network for the clock

We adapted and extended the Goldbeter and Pourquié segmentation clock model to include Delta signaling and to maintain observed phase locking between the FGF, Wnt and Notch oscillators in multiple coupled cells. Red lines show connections/processes in our model that are not in the original clock model and dotted lines show connections in the original model not used in our clock model.

Since our modified **clock** model (as well as the original) receives input from the FGF8 and Wnt3a gradients through the FGFR1 and Frizzled receptors (see Figure 7.5), we simulated how FGF8 and Wnt3a levels affect **clock** period. We found that, while the **clock** requires a minimal level of FGF8 to oscillate, the absolute level of FGF8 has no impact on the period of the **clock**. However, Wnt3a affects the period of the **clock**, with higher levels of Wnt3a leading to higher frequency oscillations (Figure 7.6b, black squares), consistent

with observations *in vivo* of clock oscillations slowing within cells as they approach the anterior of the PSM, which has lower Wnt3a levels.

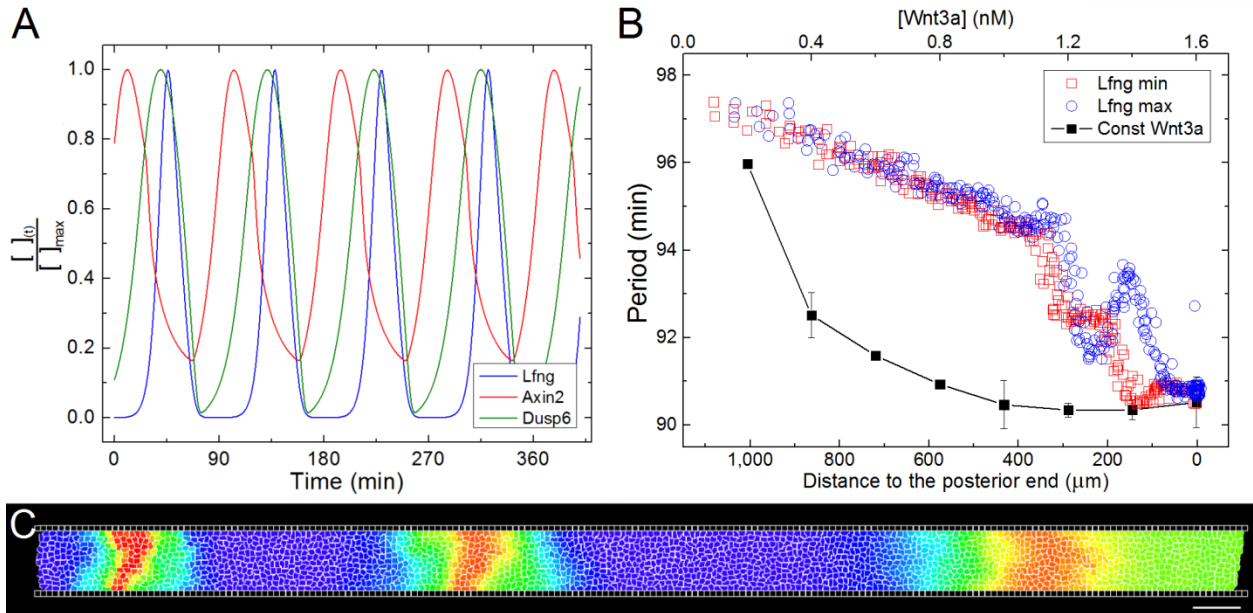


Figure 7.6 – Clock periodicity and pseudo-travelling waves

(A) Normalized Lfng, Axin2 and Dusp6 concentrations in a single, self-coupled cell. (B) Clock period versus Wnt3a concentration for a single cell with fixed external levels of Wnt3a (black) and for cells in a PSM tissue as a function of cell distance from the posterior end of the PSM. Red circles (blue squares) indicate period as measured between maximum (minimum) Lfng concentrations. (C) The distance between consecutive [Lfng] peaks and the width of the waves gets shorter as they move anteriorly (right to left). Scale bar 40 μm .

When the **clock** is added to the each **cell** of our growing **PSM** model and coupled with the FGF8 and Wnt3a gradients we observe pseudo-travelling waves in the phase of clock expression. When we visualize any specific **clock** component, such as Lfng, we observe that stripes of high Lfng concentration appear to form in the posterior and travel in the anterior direction, narrowing as they do (Figure 7.6c). As expected, such stripes do not occur in a **tissue** with constant levels of Wnt3a, in either the presence or absence of an

FGF8 gradient. Our results are consistent with a cell-autonomous oscillator-period pseudo-wave explanation for the characteristic traveling stripes of gene expression in the PSM [116-118] rather than a propagating-wave or conserved-phase-offset explanation.

Model of cell differentiation

While our multi-scale model has been very successful in explaining the observed clock behaviour in the PSM, linking the clock expression levels in the PSM cells to cell differentiation (the set of cell properties' changes that lead to somite formation) was a problem. The literature lacked both models of differentiation and experimental data on the molecular pathways which cause PSM cells to change their properties and inducer the formation of somites.

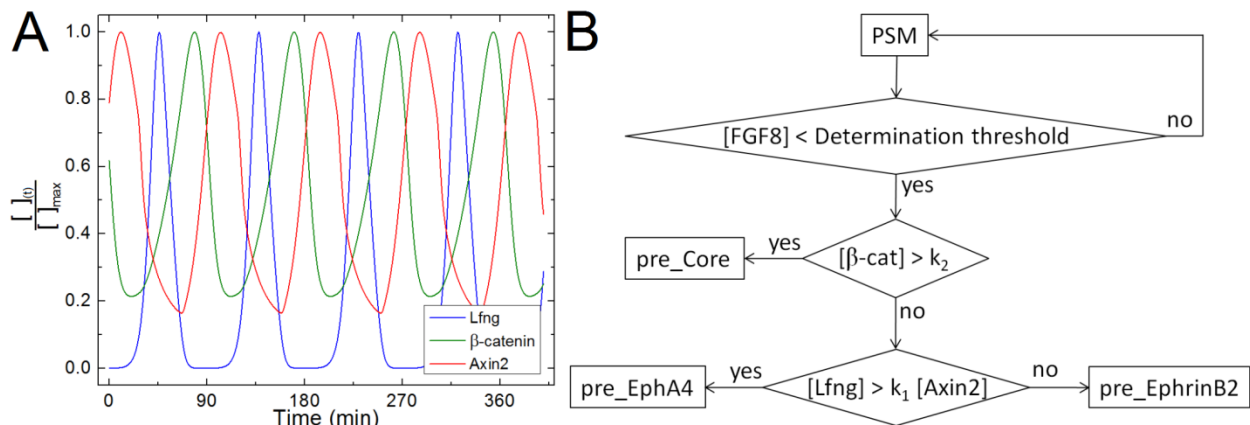


Figure 7.7 – *Ad hoc differentiation model*

(A) Normalized concentrations of *Lfng*, β -catenin and *Axin2* at the time of differentiation. (B) Boolean read-out model for PSM cell differentiation.

We therefore defined the simplest phenomenological Boolean read-out mechanism compatible with observed correlations among experimental data on cell fates, the

concentrations of clock components at the determination front and subsequent changes in cell-adhesion properties at the time of segmentation (Figure 7.7). The integrated model (the previous model as shown in Figure 7.5 and Figure 7.6 plus the read out mechanism shown in Figure 7.7) produces a first single irregular somite (reflecting the initial conditions) followed by an unlimited series of somites with consistent size and shape (Figure 7.4 and Figure 7.8a).

Simulated **PSM** and **somite tissue** morphologies closely resemble those *in vivo*. In both, somites are initially block-like and gradually round up as they mature (Figure 7.8b). The simulations also reproduce the typical border correction events described by Henry *et al.* [119] (in zebrafish) and Kulesa and Fraser [120] (in chick), where the somite edges are initially rough and later smooth as presumptive somite and PSM cells that are initially out of place rearrange to their correct position with respect to the PMS/somite border (Figure 7.8c-c'). We also showed that through adjustments of the clock period or the **PSM** growth rate, the model could produce bigger or smaller **somites** of different aspect ratios, thus corroborating the idea that the clock-and-wavefront mechanism is compatible with the evolutionary diversity of somite sizes and morphologies seen among vertebrates.

However, despite all the latter results, one of the most important findings of our project may have been the realization that we lack a set of molecular pathways to describe differentiation *in vivo*. Without these links, we cannot prove that the experimentally observed biochemical oscillators and gradients are the mechanism which produces somites.

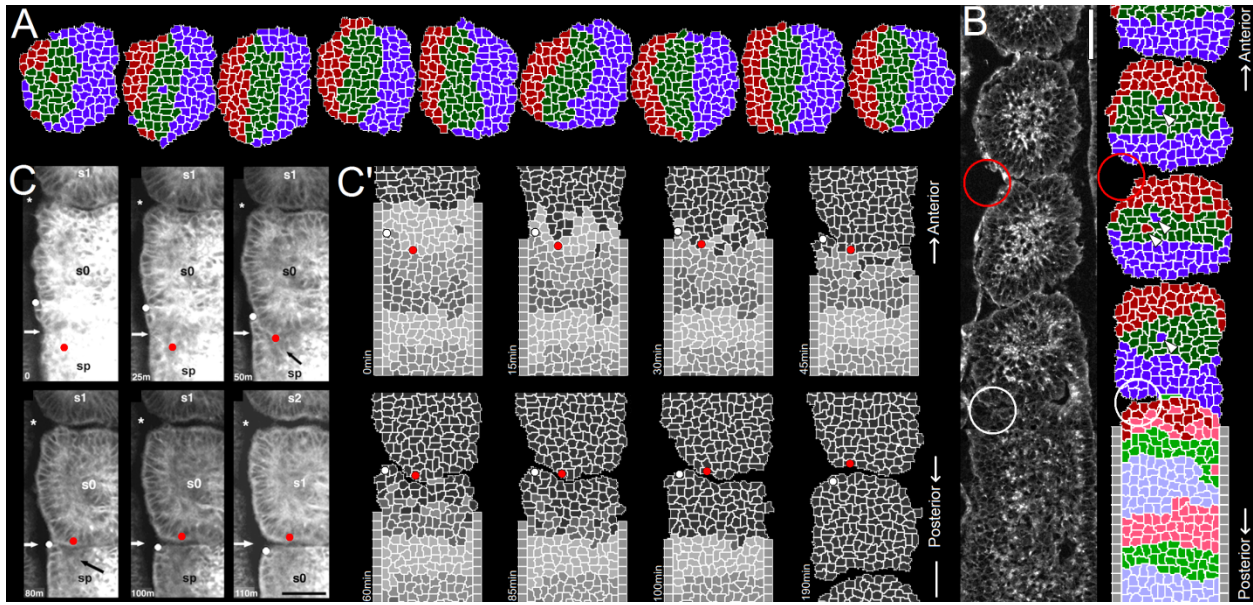


Figure 7.8 – Multi-scale model results

(A) Sequence of 9 somites from a simulation. (B) Simulated somite morphology (right) closely resembles that of chicken somites observed in vivo (left), including the initially narrow gap separating adjacent somites (white circles), the block-like shape of the newly forming somite, the gradual rounding of more mature somites, and the resulting notch-like intersomitic clefts at the medial and lateral edges of maturing somites (red circles). (C-C') Due to cell movement and errors in differentiation, some cells end up on the wrong side of the forming border between the somite and PSM. As the border develops, these two populations of cells rearrange to position themselves correctly. (C) Experimental images of chicken somites from Kulesa and Fraser [120]. Scale bar 50 μm . (C') Simulation reproducing the “ball and socket” morphology shown in (C). Scale bar 40 μm . The white and red dots in the simulation (C') correspond to the white and red dots in the experimental images in (C).

An experimental challenge to the clock and wavefront model

While we were publishing our multi-scale somite model, Dr. Claudio Stern, from University College London (UCL), and his Ph.D student, Ana S. Dias (later, Dr. Irene de

Almeida would join the project) were conducting experiments that would challenge the clock-and-wavefront hypothesis.

Their experiments pursued the observation that the BMP antagonist Noggin – which is expressed in the notochord, medial to where somites form at the tip of the *primitive streak* (PS) – suffices to transform ventral (lateral plate or posterior streak) cells, which normally do not form somites, to a dorsal (somite) fate [121, 122]. This led to the hypothesis that somites might be induced through Noggin treatment alone.

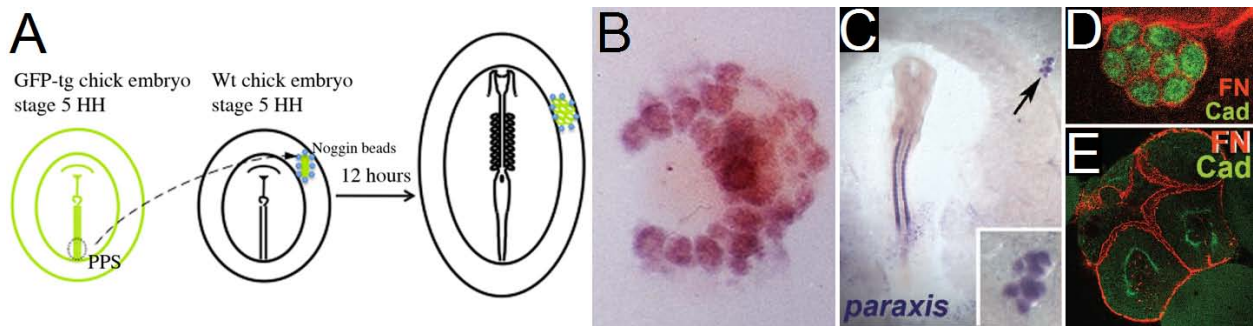


Figure 7.9 – Ectopic somite experiment

(A) Schematic of the procedure used to induce ectopic somites. (B) “Bunch-of-grapes” structure of the ectopic somites. The ectopic somites have many properties of normal somites: they express *paraxis* (C) and *N-cadherin* (green) and are surrounded by a *Fibronectin* matrix (red) (D-E).

To test whether Noggin could induce somite formation in the absence of oscillating “segmentation clock” proteins [106, 123] they applied Noggin as evenly as possible [124] to dorsalize posterior PS explants (PS cells do not form somites nor express oscillating clock genes) from quail or GFP-transgenic chick embryos. They incubated PS explants from stage-5 [125] embryos in Noggin for 3h, then grafted them into a remote region of a host chick embryo (the area opaca), where positional signals to the PSM are absent, and surrounded the explant by Noggin-soaked beads (Figure 7.9a). A few hours later (total 9-

12h), 6-14 somite-like structures, which they called *ectopic somites*, formed in a “bunch-of-grapes” pattern (Figure 7.9b) rather than in linear sequence. Like normal somites, ectopic somites express *paraxis* [122] (Figure 7.9c), consist of epithelial cells around a lumen (Figure 7.9d-e), with apical N-cadherin and a Fibronectin-positive basal lamina (Figure 7.9d-e) and are of the same size as normal somites.

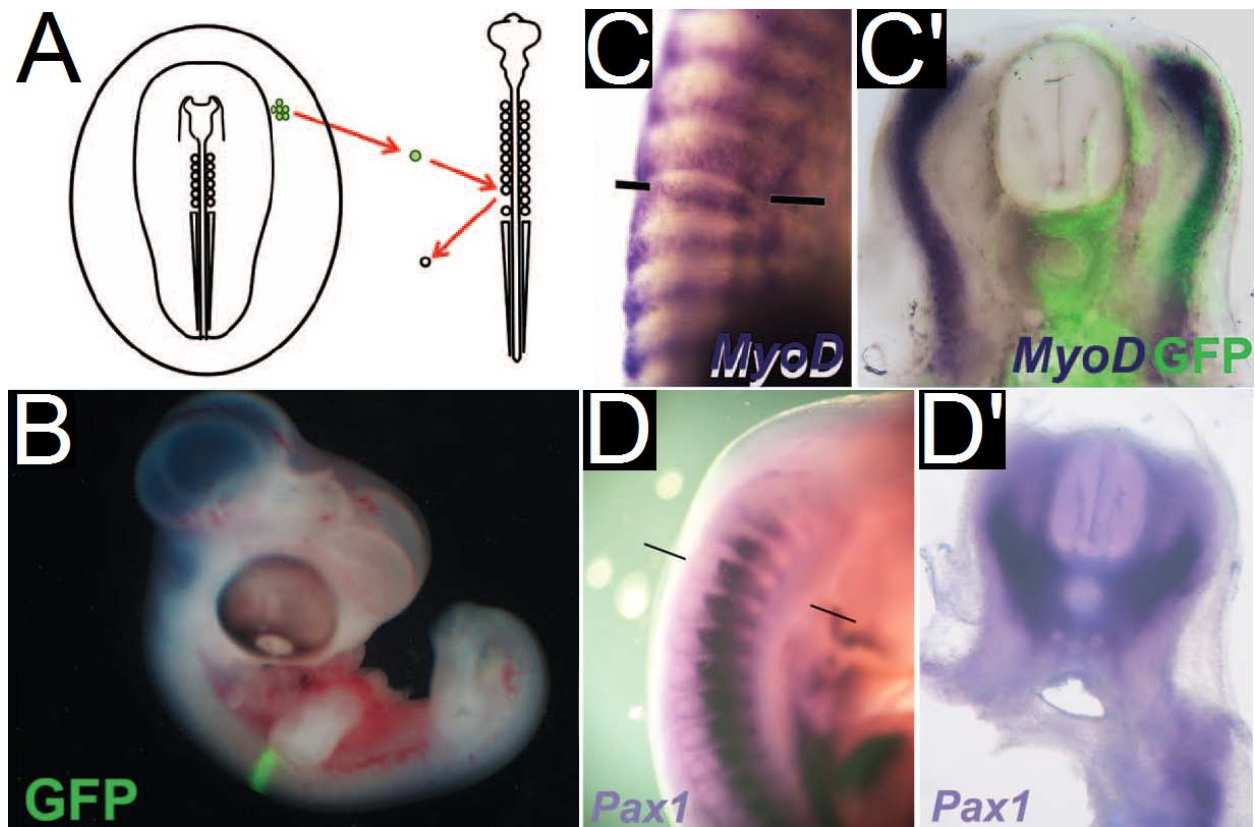


Figure 7.10 – Ectopic somite transplant

(A) Schematic of the replacement of a normal somite by an ectopic. (B) The ectopic somite incorporates well into the embryo. After 2 to 3 days, the grafted somite appropriately expresses *MyoD* (C-C') as well as *Pax1* (D-D').

To test whether ectopic somites can give rise to normal somite derivatives, they replaced individual recently-formed somites in 10-14 somite secondary hosts with ectopic GFP-transgenic somites (Figure 7.10a). After 2-3 days (stage 19-25) the grafted somite was

well integrated into the developing host tissue (Figure 7.10b) and expressed the dermomyotome/muscle marker *MyoD* (Figure 7.10c-c') and the sclerotome/vertebral marker *Pax1* (Figure 7.10d-d') in the correct positions. Some blood vessels also formed, which may be normal somite derivatives [126, 127] or a result of some cells retaining their original lateral (non somitic) fates. Thus, the ectopic somites are functionally similar to normal somites.

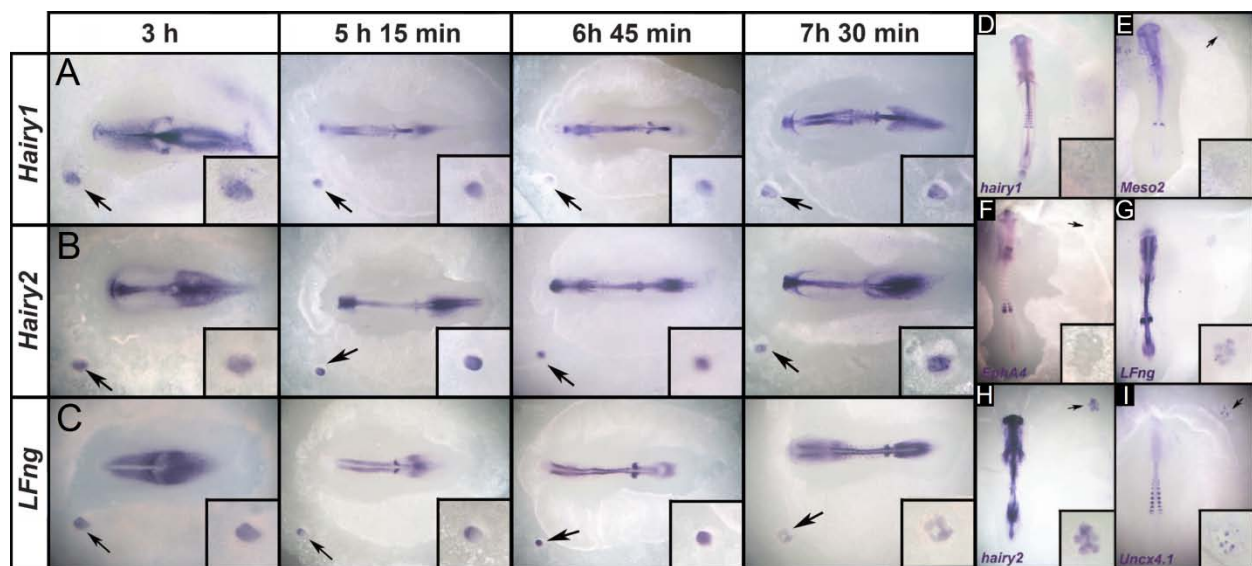


Figure 7.11 – Clock and somite expressions on ectopic somites

(A-C) Embryos were fixed at 45-min intervals (examples shown at 3, 5.15, 6.45, and 7.5 hours after grafting into a host embryo) then stained for expression of *Hairy1* (A), *Hairy2* (B), and *LFng* (C). Genes with oscillatory expression in normal PSM remained at constant levels in the implanted tissue (insets). Ectopic somites do not express caudal markers *Hairy1* (D) or *Meso2* (E) or the rostral marker *EphA4* (F). They express the caudal markers *LFng* (G) and *Hairy2* (H) weakly and uniformly; and the caudal marker *Uncx4.1* (I) in random patches. Insets show magnified view of the grafts.

To test whether they form sequentially or simultaneously, they filmed ectopic GFP-transgenic somite formation in time-lapse. While normal somites form sequentially every 1.5 hours in chick, about 6-14 somites form within 2 hours (9-11h after grafting). The

almost synchronously formation of so many somites suggests that ectopic somites form independently of a clock. To assess the molecular clock, they examined embryos at different time points prior to ectopic somites formation for expression of “clock-genes” *Hairy1* (Figure 7.11a), *Hairy2* (Figure 7.11b) and *Lfng* (Figure 7.11c) at 45 min intervals between 3-7.5 hours following exposure of PS explants to Noggin. While host embryos had typical [106] oscillatory patterns of expression, the explants showed approximately the same expression at every time point.

Normal presomitic mesoderm expresses *Dapper-1* for several hours before somite formation and *Dapper-2* during and after somite formation. Before and after producing ectopic somites, Noggin-treated PS mesoderm expresses *Dapper-2*, but not *Dapper-1*, suggesting that ectopic somites form without the prior presomitic-like state seen in normal PSM. These results strongly suggest that the ectopic somites form simultaneously and without cyclic expression of “clock-genes”.

Normal somites consist of rostral and caudal halves with different gene expression patterns, a property subsequently required for proper development of the peripheral nervous system [128]. To test whether the ectopic somites are subdivided they examined expression of caudal (*Hairy1*, *Hairy2*, *LFng*, *Uncx4.1*, *Meso2*) and rostral (*EphA4*) markers. Ectopic somites seem to lack coherent rostrocaudal identity. The caudal markers *Hairy1* (0/22), *Meso2* (0/22) and the rostral marker *EphA4* (0/19) were not expressed (Figure 7.11d-f). The rostral marker *LFng* (22/24) (Figure 7.11g) and *Hairy2* (8/8) (Figure 7.11h)

were expressed weakly and uniformly throughout the somites and *Uncx4.1* (13/19) in patches (Figure 7.11i).

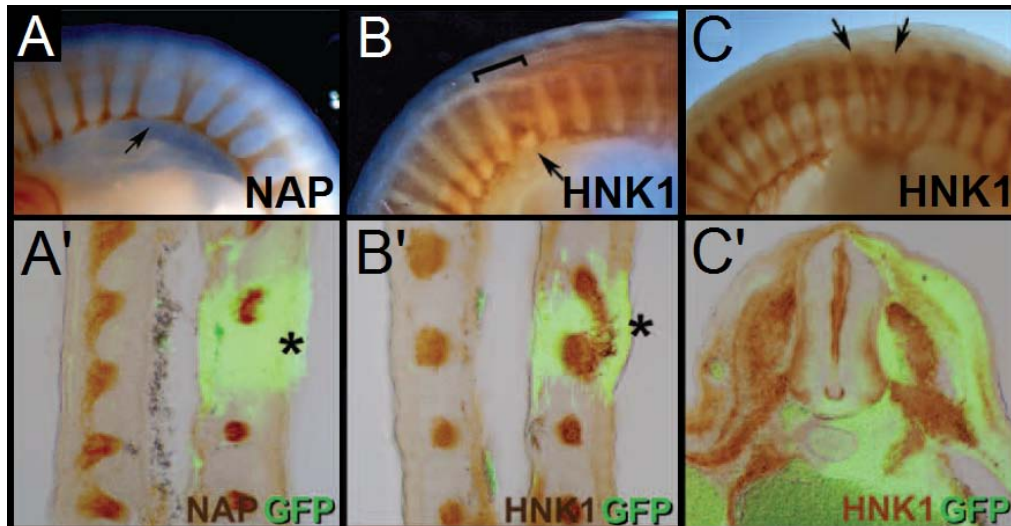


Figure 7.12 – Motor axons and neural crest staining on grafts

Chick embryos with grafted ectopic somites were stained for motor axons [NAP, (A), brown] or neural crest cells [HNK1, (B,C), brown] and anti-GFP [green in (A',B',C')]. An abnormal large gap (A), fused roots (B), and multiple small ganglia (C) form in the ectopic somite (arrows, asterisks). Sections (A',B') are coronal and (C') is transverse at the level of the graft.

As neural crest cells and motor axons normally only migrate through the rostral half of the sclerotome [128], they used this as an additional test of somite patterning. After grafting an ectopic GFP-somite in a secondary host (Figure 7.10a) they confirmed that, at stage 22-25, the patterns of motor axon growth (Figure 7.12a-b) and neural crest migration (Figure 7.12c) were disrupted. Abnormalities included an enlarged gap between motor roots (Figure 7.12a), fusion of adjacent roots (Figure 7.12b) and formation of several small ganglia within a grafted somite (Figure 7.12c), as if the somite contained random islands of permissive (non-caudal) cells exploited by axons and crest cells. These results suggest that the ectopic somites are not subdivided into rostral and caudal halves, suggesting that either

the AP gradients or the oscillatory genes of the clock is required for this feature of segmentation [129].

What does control somite formation?

While ectopic somites form without an oscillating “segmentation clock” or a determination wavefront, their properties, except for their subdivision into rostral and caudal halves, are normal. Thus, induction and regulation of somite formation seem not to require the segmentation clock or wavefront.

If clock-and-wavefront mechanisms do not control somite formation, what does? The ectopic somites suggest that local cell-cell interactions must be responsible. A local mechanism also agrees with other embryological experiments of Dr. Stern [130] that suggest that somites are self-organizing structures, regulated by intrinsic cell and ECM properties and by the packing constraints of cells undergoing *mesenchymal-to-epithelial* (*MTE*) transition.

In order to test the hypothesis that MTE mechanics regulates somite initiation and formation, I built a new model for somite formation including MTE mechanisms, but without a clock or sequential cell differentiation. If virtual tissue simulations of this model produce rostral-size somite-like structures synchronously, clock-and-wavefront mechanisms are not necessary for somitogenesis, though they may well play a signaling role *in vivo*.

A self-organizing somitogenesis model

Unlike our multi-scale model of clock-and-wavefront somitogenesis, I now model ectopic somite formation, not *in vivo* somitogenesis. Thus, all modeled **cells** are initially identical and differentiate and epithelialize at the same time.

To form large, repeating structures from this starting condition, the cells must first be able to polarize and rearrange their polarity according to their immediate neighbors, and then use their polarity to pull on other cells and rearrange their positions to form a local epithelium segment, which on a larger scale would be part of a somite-like structure. I model dynamic cell polarization using the dynamic domains method from Chapters 3 and 6, and use it to control polarized pulling forces using the dynamic links method from Chapters 4 and 5.

The key biological assumptions that I made in order to construct the model are:

- i) **extra-cellular fluid** is already present between the **cells** before differentiation;
- ii) **cells** in the **tissue** are exposed to Noggin evenly and simultaneously;
- iii) in response, **cells** gradually polarize and elongate;
- iv) polarized **cells** secrete **extracellular-matrix (ECM)**;
- v) Apical and basal surfaces of polarized **cells** have an affinity for **ECM** and **extra-cellular fluid** and repel each other;
- vi) tight junctions form between apical ends of adjacent and aligned **cells**;
- vii) misplaced **cells** rearrange their polarity and attach to their appropriate ends.

Assumptions i) and ii) describes the initial condition in the ectopic somite induction experiments. Assumption iii) is a necessary condition given the changes in shape of the cells before and after somite formation, both *in vivo* and in the graft experiments. Before forming somites, the PSM cells and the posterior PS cells are mesenchymal and isotropic; while after somite formation their shapes are no longer symmetric, but elongate to an almost 1:12 ratio between their major and minor axis.

To model the cell epithelialization process the differentiated cells are represented with three compartments: **Apical**, **Basal** and **Lateral**, which, as was done in Chapter 6, are randomly distributed inside the cell volume at the time of differentiation. Because of the highly elongated shape that the cells will acquire, I choose to not include an **internal/core** compartment, as I did in Chapters 3 and 6.

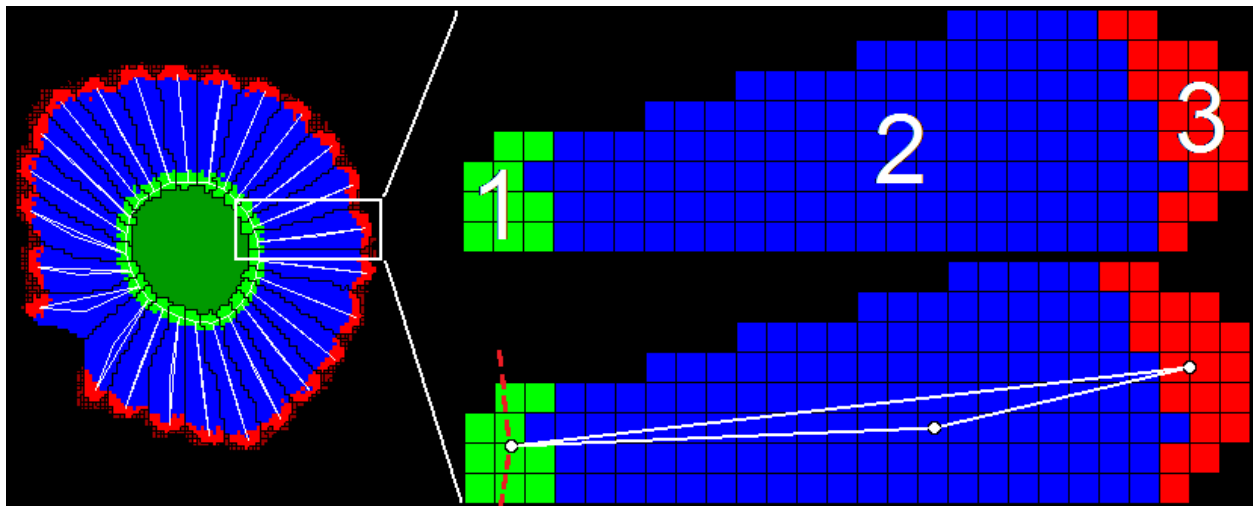


Figure 7.13 – Ectopic somite model

Left: simulated ectopic somite. Upper right: close up of an epithelial somite cell with 3 compartments: Apical (green), Lateral (blue) and Basal (red). Bottom right: internal links (solid white lines) between the centers of mass of the compartments drive and maintain cell elongation. External links (dashed red lines) between cells drive Apical constriction. Dark green represents Lumen; dark red represents ECM.

To implement the cell elongation occurring during somitogenesis I used internal length constraints between the cells' **Apical**, **Basal** and **Lateral** compartments. Initially, when the **cell** first polarizes (or when it repolarizes, as I explain later), these constraints are weak, to allow free rearrangement and segregation of the compartment in response to cues from the cells' immediate **neighbors**. As time passes, the target length between compartments (**Lateral- Apical** and **Lateral-Basal**) gradually increases, elongating the **cell** up to a pre-defined aspect ratio. Because the microtubules in polarized cells are straight and rigid, I also include a third link between the **Apical** and **Basal** compartments with a target length set equal to the sum of the first two, thus preventing bending of the **cell**.

Assumptions iv) and v) directly represent experimental observations. During normal somitogenesis some ECM is present by the time of somites form. In ectopic somites the cells produces all the ECM during somite formation. I model this ECM production by creating a small volume of **ECM**, represented by an **ECM cell**, at the interface between the **cell's Basal** surface and another **Basal** surface or **Medium**, as long as they are not already in contact with another **ECM**. Here, **Medium** represents the host environment to where the posterior PS mesenchymal cells were transplanted.

As the somites (normal and ectopic) are assembled, they form a single layer of epithelium enclosing a luminal space. Since the lumen is not created by the cells (in fact, the cells actually pump some fluid out of it⁵) this extracellular space must be already present with the mensechyme. As the cells epithelialize and pack, this extracellular space is

⁵Dr. Claudio Stern private communication

rearranged and localizes into the interior space of the somites. In the model, in order to conserve locality, the **extra-cellular fluid** is represented as a series of small **cells** placed around the **mesenchymal cells**. If I represented it as one big **domain**, then, due to the Potts formalism, nothing would prevent its volume from shrinking at one locality and increasing at another, unconnected (but pre-existing) spot. By using a series of **domains** instead, each **lumen compartment** have to be spatially transported between any two places, which yield a more realistic representation of a fluid in the Potts formalism, as was done previously in [131].

Together, the two experimental observations provide the existence of two types of extracellular space: an internal space, which is already present and later localizes to the interior of the **somites**, modeled as the **extra-cellular fluid**; and an external space, generated by the **cells**, that envelops each **somite**, modeled as the **ECM**. This gives the **somite cells** two cues that help them orient their polarization and indicate to them whenever they are misplaced or not. Only properly oriented **cells** – *i.e.* **cells** whose **Basal** ends are oriented to the external medium (**Medium** or **ECM**) and **Apical** ends oriented to the **extra-cellular fluid** – are allowed to proceed with elongation; the fate of misplaced **cells** will be discussed momentarily.

As the cells epithelialize, they apically constrict, thus curving the forming epithelium and giving rise to the spherical shape of the somites. In the model, apical constriction of properly aligned/polarized **cells** is modeled in a similar way as was presented on Figure 4.1a-d: neighboring **Apical** compartments are linked by a spring force whose target

distance decrease gradually in time down to some lower limit. Those links can only be made by **cells** that are aligned (share contact surface between **Apical-Apical** and **Lateral-Lateral** compartments) to prevent connection between opposing **cells**.

The process of somite formation is very dynamic and cells often rearrange their positions and extend filopodia in different directions until they reach their “correct” locations [132]. This happens for “lost” cells both near the forming apical/internal surface of the somite that try to reach the basal side/fibronectin matrix around the somite, as well as for cells lying at the periphery of the forming somite that are trying to extend to the apical side. I model this behavior with the dynamic links method in a similar way as was done in Chapters 4 and 5. In the model, partially misplaced **cells**, *i.e.* **cells** whose **Basal** or **Apical** ends are not properly exposed, temporarily forms a link between their misplaced compartments (let’s say it is the **Basal**) and the **Basal** compartment of a randomly selected neighboring **cell**. The misplaced **cell** then pushes and elongates toward that direction. If successful, that is, the **cell** comes into contact with **ECM** or **Medium**, the **cell** will spontaneously stabilize in the new position, otherwise a new attempt will be made later. The same happens for misplaced **Apical** compartments.

If a **cell** happens to be completely misplaced, that is, when both ends are not exposed to the appropriate external environment, the **cell** reset its polarity by losing its **compartments**, which are later randomly distributed again inside the **cell** volume. These events, repolarization and tentative attachments, are not done continuously, but at a predefined frequency.

Results

For simulations with large number of **cells** ($N \geq 198$, Figure 7.14a), ectopic **somite** formation can be classified in three stages: *cell polarization*, *tissue epithelialization* and *somite clustering*. The first stage is marked by intense **cell** rearrangement and repolarization until some small groups of **cells** start to form short epithelial segments of 2 to 4 **cells** with a continuous **Basal-ECM** surface and a common **Apical-extra-cellular fluid** end (Figure 7.14b-c). As the simulation proceeds, those segments grow through attachment of neighboring **cells**, while new epithelial segments form on other regions of the simulated graft until most of the **cells** are properly epithelialized/elongated (Figure 7.14c-d). At the last stage, small **somite**-like structures start to form and grow to their appropriate sizes (to be discussed later), usually by **cell** attachment to small **somites** or fusion of adjacent small **somites** (Figure 7.14e-f). When a larger than usual **somite** forms through fusion it quickly shrinks back near to the average size by detachment of some of its **cells**, that later repolarizes and join neighboring **somites**.

It is not clear if the three stages of ectopic **somite** formation occurs in the same way in the ectopic somite experiments. Because the extraembryonic region of the chick (where the cells are grafted) moves during the course of ectopic somite formation, it is hard to maintain a close focus on the graft. As a result, the collected images/videos do not have sufficient time or spatial resolution to distinguish individual cell behaviors. However, at the

time this thesis is being written, new students have joined his lab to conduct experiments aimed to that end.

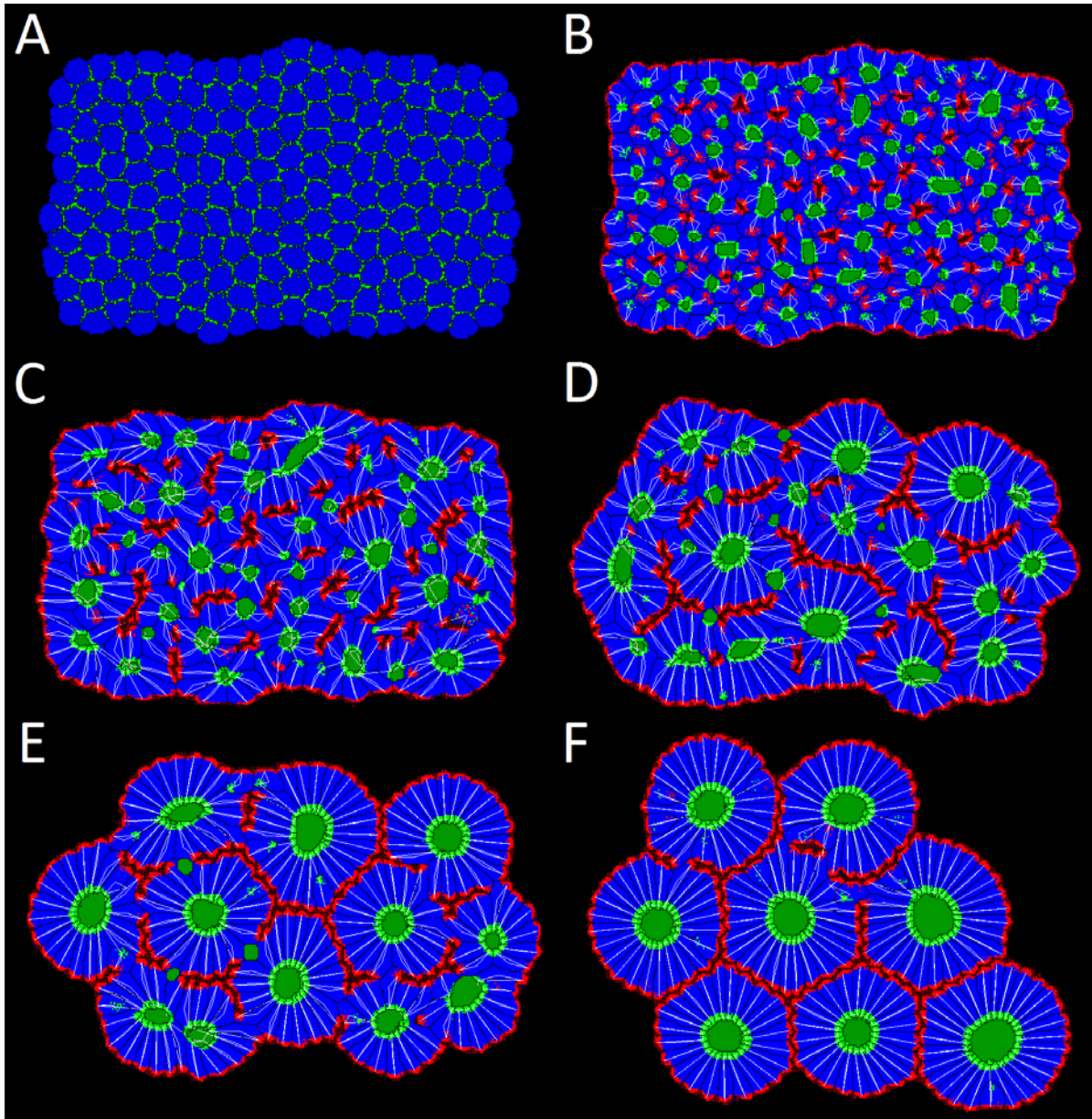


Figure 7.14 – Ectopic somite simulation with 198 cells

(A) Initially all cells are mesenchymal and distributed in a rectangular area. (B) After Noggin treatment, each cell undergo MET and increase the adhesion to each other. (C) The polarized cells start to elongate and secrete ECM. (B-E) As cells rearrange their positions the internal liquid is displaced and accumulates at the center of the forming somites. (F) After some time the cells stabilize and forms somite-like structures of similar shape and size. Snapshots at 4000, 5000, 6000, 10000, 20000 and 50000 MCS.

In the simulation shown on Figure 7.14, all **somites** have about the same size ($\langle N_{\text{somite}} \rangle = 24.5 \pm 2$ **cells**). While this number fluctuates by up or down one **cell** for different runs, it does not increase or decrease by any significant value if more **cells** are added to the initial condition (as long as the geometric distribution of **cells** remains closely the same, as it will be discussed later). This regularity is a result of the packing constraint of the **cells**, such as their ratio of elongation, the degree of apical constriction and the sizes of the **Apical** and **Basal** compartments. When I vary those constraints, the model produces **somites** of different sizes, as it can be seen on Figure 7.15.

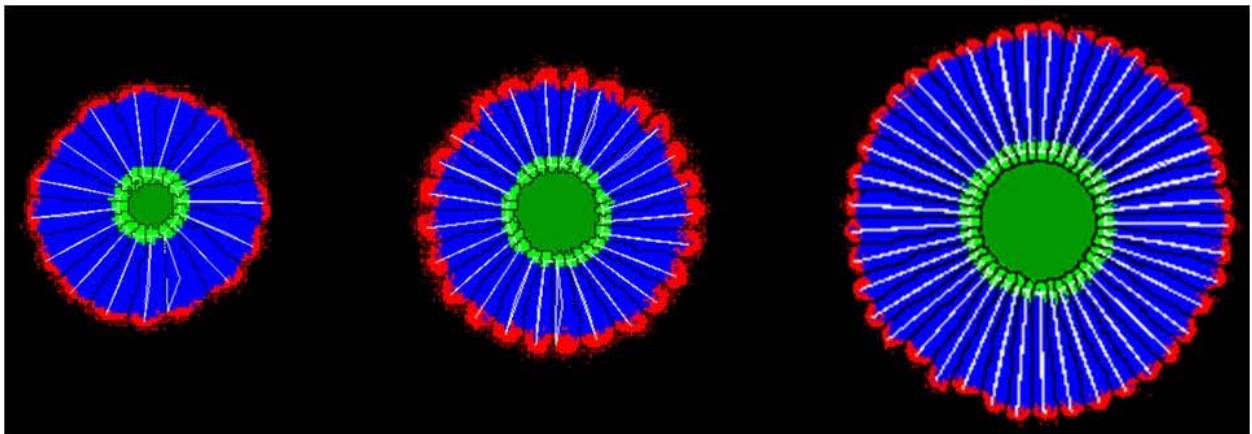


Figure 7.15 – Somite sizes

*The number of cells per somite is determined by packing constraints such as the degree of cell elongation, the apical constriction tension and the sizes of **Apical** and **Basal** compartments. From left are somites made of 16, 25 and 41 cells.*

While I did not make a systematic study on how all the different parameters combinations affect **somite** size, they seem to be subjected to at least two restrictions to assure proper **somite** formation: i) the size of the **Basal** compartment should be proportional to **somite** curvature (as determined by the degree of elongation and apical

constriction); ii) the amount of **extra-cellular fluid** should be proportional to the number of **cells per somite** and the degree of **apical constriction**. In all simulations presented below, the packing constraints were chosen so that the somites should have an ideal, or average size of $N_{\text{somite}} = 25$ cells.

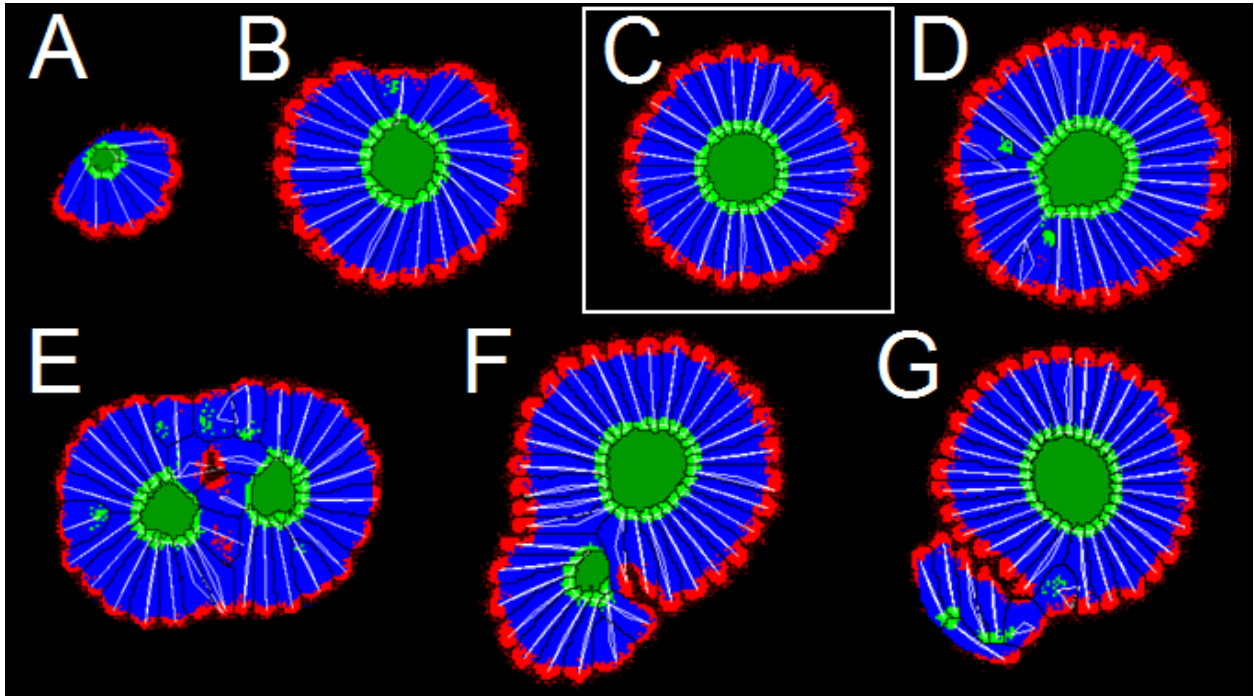


Figure 7.16 – Number of cells and somite formation

Panels (A-B) show simulations with less cells than the average somite size [25 cells, shown in (C)] and panels (D-G) shows simulations with more cells than the average somite size. From (A) to (G), simulations with 6, 20, 25, 30, 32, 35 and 35 cells.

Besides a coherent set of internal packing constraints, there are also two spatial requirements to assure proper **somite** formation in the model: i) the number of initial **cells** (N) must be close to a multiple of the average number of **cells per somite** (N_{somite} , as determined by the packing constraints); and the geometrical distribution of **cells** must be isotropic and “compacted” enough to allow clustering of all **cells** into a single structure.

Because the typical size of a **somite** (as given by a set of parameters) is not a precise number, but varies around a mean, the first spatial requirement ($N/N_{\text{somite}} \cong x, x \in \mathbb{N}$) is only important for simulations with a small number of initial **cells** ($N/N_{\text{somite}} < 5$). If N is at, or close to that mean, **somite** forms normally (Figure 7.16b-d). If N is significantly smaller than N_{somite} , a small, bended **epithelial** segment forms instead of a small **somite** (Figure 7.16a). And if N lies between two N/N_{somite} ratios, the simulations can display pairs (or triplets) of semi-fused **somites** of roughly the same size (Figure 7.16e) or of different sizes (Figure 7.16f), or even a well formed **somite** with lost **cells** or **epithelial** segments around it (Figure 7.16g); in the last case it is not possible to predict the actual outcome.

The second spatial requirement, the geometry of **tissue** distribution, is perhaps more critical to proper **somite** formation than the previous one, as in this case **somites** can completely fail to form even if a large number of **cells** is provided. Because **cell** epithelialization, or **compartment** distribution (**Apical**, **Basal**, **Lateral**), is partially guided by the immediate neighborhood of the **cell**, the first stage of **somite** formation, cell polarization, fails if the **cells** are not initially in contact with each other. So, in the model, **somite** fails to form when the **cells** are initially scattered instead of being close to one another.

If the **cells** are not sparsely distributed, but are all connected in a contiguous **tissue**, the first two stages of **somite** formation (cell polarization and tissue epithelialization) will definitely occur, but that is not enough to ensure proper **somite** formation. For example, if 25 **cells** are distributed in a narrow row instead of in a more compact shape (like a 5x5

square), they form small **epithelial** segments (as in Figure 7.16a), but not a **somite**, despite having the required number of **cells**.

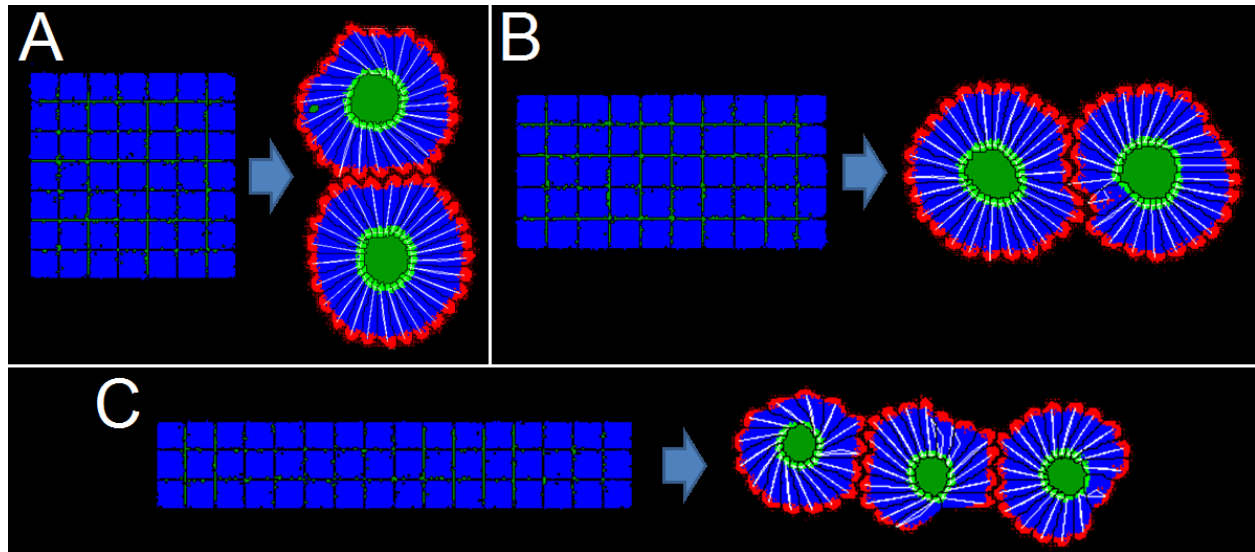


Figure 7.17 – Graft geometry and somite formation

In all panels, the simulations start with similar number of cells, sufficient to produce 2 somites. (A) A compact initial distribution of 49 cells (7x7) produces two somites aligned at random orientations (here, vertically). (B) When 50 cells are distributed in a rectangular area (5x10), the two somites form aligned with the longer axis of the initial distribution. (C) If 48 cells are distributed in a highly isotropic shape (here 3x16), 3 ill-formed somites are produced instead of 2.

The geometry of **cell** distribution also influences the alignment and the number/sizes of the **somites**. For a simulation with packing constraints that favor a 25-cell **somite** (as presented in Figure 7.13, Figure 7.14 and Figure 7.16) and enough **cells** to make two of them, the resulting **somites** will be randomly aligned if the initial distribution is a circle or a square (Figure 7.17a). If the **tissue** is distributed in a rectangular area instead, such as the 5x10 cells geometry in Figure 7.17b, the two resulting **somites** will always be aligned with the longer side of the rectangle. Finally, Figure 7.17c shows a situation where 48 **cells** are distributed in a highly anisotropic shape (3x16 **cells**). In this case, because one of the sides

of the **tissue** (3 cells) is significantly short compared to the diameter/side of the ideal **somite** for the given set of packing constraints, instead of forming two **somites**, the simulation will produce 3 ill-formed **somites** aligned with the major axis of initial geometry.

Back to normal somites

The self-organized somite model has successfully reproduced the main features of the ectopic somite experiments, thus suggesting that an epithelialization process alone can account for the formation of such structures. But a second question is whether the same mechanism could also be involved in the formation of somites as seen *in vivo*. While I cannot answer this question (at least when formulated in this general way), I can certainly address a more specific one: can the ectopic somite model also generate **somites** sequentially rather than synchronously?

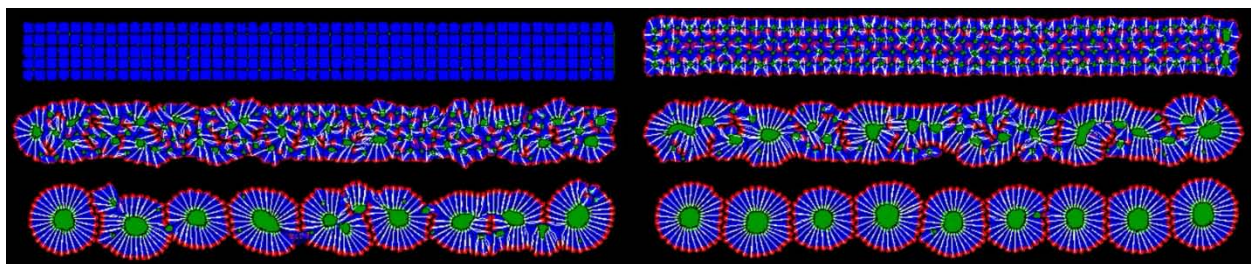


Figure 7.18 – Ectopic somite formation on a PSM-like strip

*When the **tissue** is distributed as a stripe of 5x50 cells and set to differentiate at the same time, 9 somites form on a line in the same sequential stages as seen in Figure 7.14.*

As a first step, I ran the ectopic somite model using an initial **tissue** distribution of 5x50 cells (Figure 7.18) that closely resembles the shape of a real chick PSM segment

(Figure 7.1). Because the width of the stripe is about the same length of the lateral side of the ideal **somite**, the simulation produces properly formed **somites** (in contrast with Figure 7.17c) aligned with the initial **tissue** layout. Not surprisingly, the sequence of **cell** movements leading to **somite** formation is the same as the three stages described for the simulation shown on Figure 7.14. However, instead of forming 10 **somites** of 25 **cells**, the simulation forms 9 **somites** of about 27 **cells** in size.

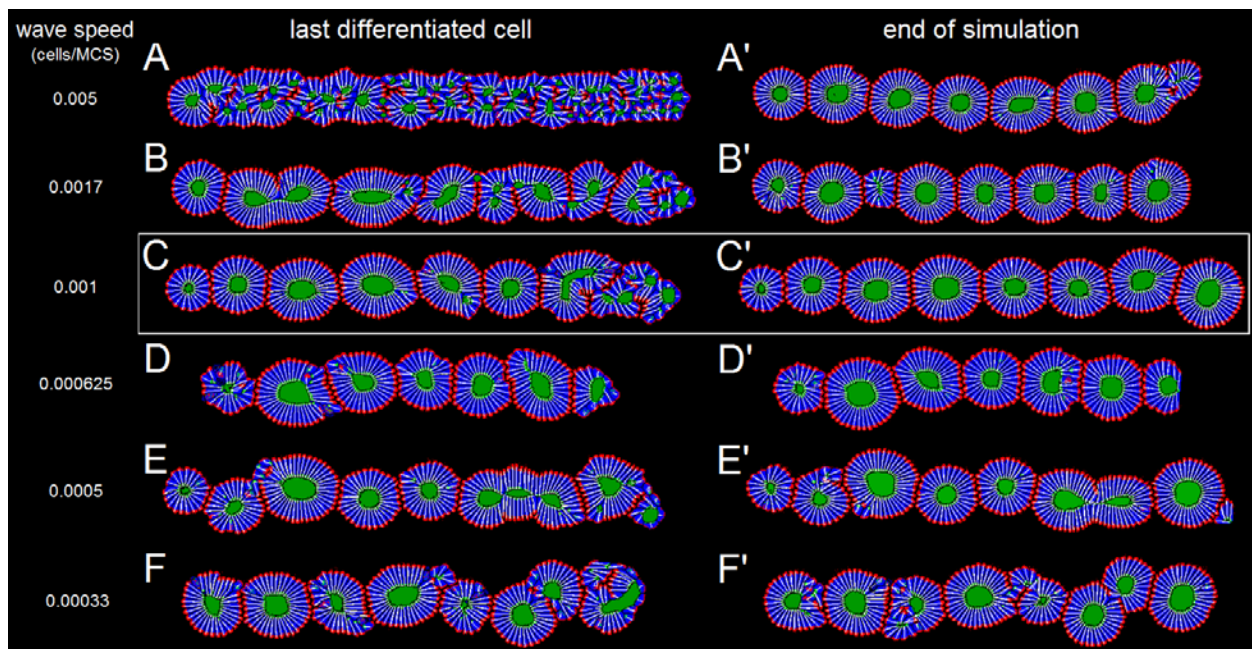


Figure 7.19 – Wavefront speed versus somite formation

*The first column (A-F) shows the state of the **tissue** at the time the last column of **cells** differentiates. The right column (A'-F') shows the **tissue** at the end of the simulation. Each row corresponds to a different wave speed, as indicated on the left. Anterior to the left, posterior to the right.*

Next I simulated a PSM-like strip of **tissue** where the **cells** differentiate sequentially, rather than synchronously, to reproduce the presence of a wavefront. The speed of the wavefront (measured as **cells** per MCS) seems to have no effect on the final **somite** size distribution (Figure 7.19a'-f'). In all simulations, most of the **somites** are well formed and

have similar sizes (about 34 cells), with some small **somites** (usually at the anterior end) and a few ill **formed** somites or **epithelial segments**, usually at the posterior end of the simulated **PSM** (in those cases, this can be attributed to an insufficient number of available **cells** at the end of the **PSM**). At higher wave speeds, however, the occurrence of such defects seem to be more frequent (compare Figure 7.19d'-f' to Figure 7.19a'-c').

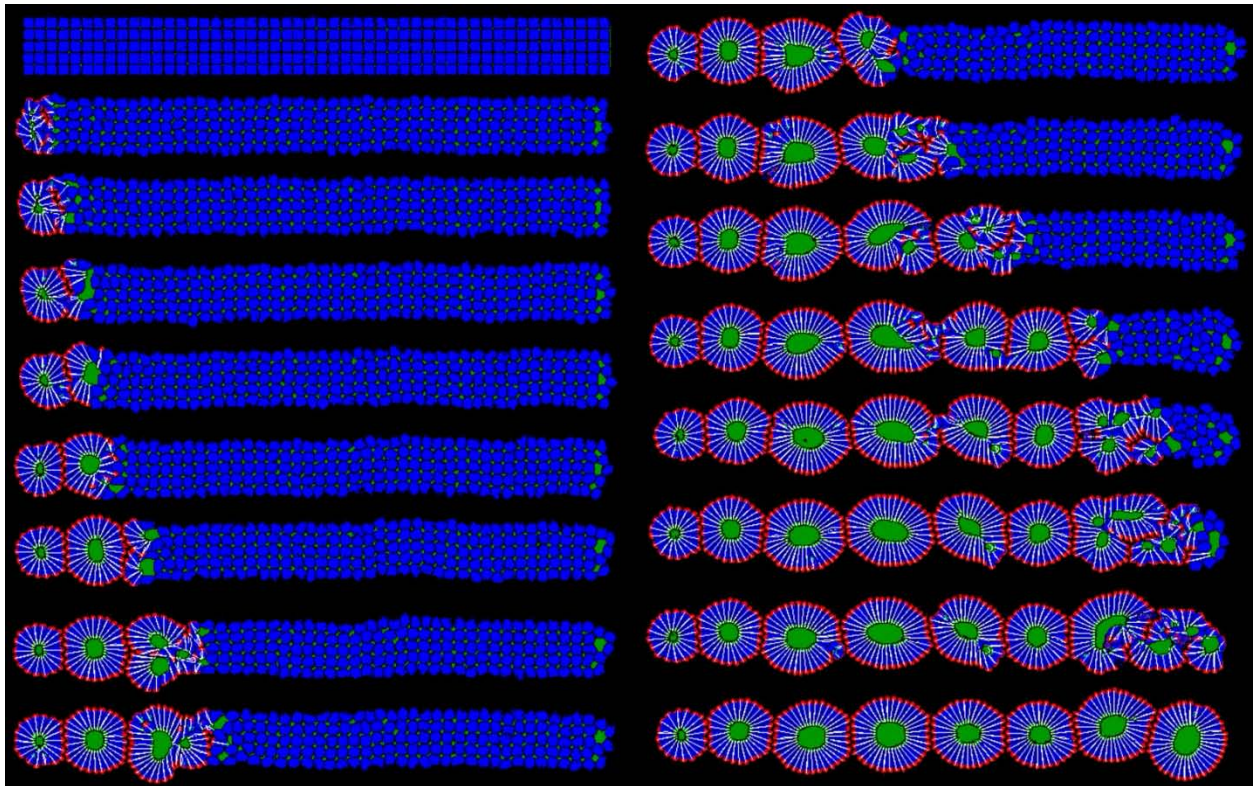


Figure 7.20 – Somitogenesis with self-organizing somites

Snapshots of the simulation shown in Figure 7.19a. The first two formed somites (to the left) are smaller than the subsequent somites, which have an average size of 34 cells. Somite sizes (from left): 18, 27, 35, 36, 32, 30, 35 and 36 cells.

While the **somite** shape distributions look alike at the end of the simulations, inspection of **somite** shapes as the wavefront moves reveals more variation among the different wave speeds. When the wave moves too fast, the **cells** have not formed any

somites by the time the wave reaches the posterior end of the **PSM** (Figure 7.19a), and the **tissue** looks like the initial stage of ectopic **somite** formation on the third panel of Figure 7.18, with all the **cells** polarized, but not forming any **epithelial segment** yet. Slightly slower wave speeds result in a **tissue** that looks like the second stage of ectopic **somite** formation, mainly composed of **epithelial segments** and a few forming **somites** (Figure 7.19b). When the wave moves too slow, the **cells** tend to form bigger **somites**, that, due to incompatibility with the packing constraints, are not stable and result in ill-formed or semi-fused somites (Figure 7.19d-f).

For wave speeds at around 0.001 **cells** per MCS, most of the **tissue** is composed of properly formed **somites** by the time the wave reaches the posterior end of the **PSM**, with the rest of the **tissue** (which will form the last two **somites**) already epithelialized (Figure 7.19c). At this speed, **somites** form and stabilize continuously as the wave passes (Figure 7.20), with the **cells** quickly forming an **epithelial segment** soon after differentiation. It is interesting to note that in this particular simulation the first two **somites** are smaller than the rest, similar to what is observed in normal chicken somitogenesis.

Discussion

The computational work presented here complements the experimental work of Dr. Stern *et al.* While our collaborator demonstrated that the “bunch-of-grapes” is indeed composed of real somites that form without a clock, I show that a set of reasonable

assumptions about the symmetry breaking process as the cells differentiate and epithelialize can result in the spontaneous formation of **somite**-like structures. In the last part of this chapter, I go a beyond what we have published [1] and show that the same model can also produce **somites** sequentially, similarly to real vertebrate somitogenesis.

For the ectopic somite model I can safely assume that all **cells** differentiate at the same time, but the sequence of **cell** behaviors (polarization, adhesion, elongation, pulling etc) and their rates/intensities cannot be directly compared to experimental data as those measurements have not been done yet. This makes any inference about the conversion of MCS to real time units problematic. A detailed study of the epithelialization process in ectopic somites and its use to fine tune the model is a project that we are currently pursuing.

As for the real somites, the sequence of cell behaviors leading somite formation has been subject of study for some time and the recent paper by Dr. Martins *et al.* [132] reveals much about the cell movements taking place during this process. Those details, however, were not included in the simulations of the sequence activation of cell differentiation shown in the previous subsection. There I choose to limit the investigation as to whether the same processes used for the formation of ectopic **somites** could also generate them in a sequential fashion, and what are the conditions at which it does so.

A more accurate simulation of *in vivo* somite formation without the use of a clock would require a 3D version of the model, as somites seems to first epithelialize their the dorsal and ventral sides before they form their anterior border. As was shown in Chapters 5

and 6, the two basic methods used for the new somite formation model – the dynamic domains and the dynamic links – can be easily extended to three dimensions. Doing so, however, requires readjustment of many CPM parameters and comes at the cost of the extra computational time. While I believe that the extra dimension will actually smooth and facilitate the **somite** formation process, there was no time to address this before the completion of this thesis.

Finally, I would like to end by bringing to attention that the ectopic somite formation model presented here would not be possible to simulate – at least within the CP/GGH framework – without the two techniques that I developed in the first part of this thesis. I hope that I successfully made the case that both numerical techniques are valuable extensions to the CP/GGH model, and that, as exemplified by the PCP model of Chapter 3, the cell intercalation model of Chapters 4 and 5, the renal tubule model of Chapter 6 and this last Chapter (were both are combined), they can be used to successfully model real biological problems.

REFERENCES

1. Dias, A.S., et al., *Somites Without a Clock*. Science, 2014. **343**(6172): p. 791-795.
2. Hester, S.D., et al., *A Multi-cell, Multi-scale Model of Vertebrate Segmentation and Somite Formation*. Plos Computational Biology, 2011. **7**(10).
3. Ermentrout, G.B. and L. Edelstein-Keshet, *Cellular automata approaches to biological modeling*. J Theor Biol, 1993. **160**(1): p. 97-133.
4. Deutsch, A. and S. Dormann, *Cellular automaton modeling of biological pattern formation : characterization, applications, and analysis*. Modeling and simulation in science, engineering and technology. 2005, Boston: Birkhauser. xxiii, 331 p.
5. Paiva, L.R., et al., *Multiscale model for the effects of adaptive immunity suppression on the viral therapy of cancer*. Phys Biol, 2013. **10**(2): p. 025005.
6. Honda, H., *Description of cellular patterns by Dirichlet domains: the two-dimensional case*. J Theor Biol, 1978. **72**(3): p. 523-43.
7. Drasdo, D., R. Kree, and J.S. McCaskill, *Monte Carlo approach to tissue-cell populations*. Phys Rev E Stat Phys Plasmas Fluids Relat Interdiscip Topics, 1995. **52**(6): p. 6635-6657.
8. Honda, H., M. Tanemura, and T. Nagai, *A three-dimensional vertex dynamics cell model of space-filling polyhedra simulating cell behavior in a cell aggregate*. J Theor Biol, 2004. **226**(4): p. 439-53.

9. Weliky, M. and G. Oster, *The mechanical basis of cell rearrangement. I. Epithelial morphogenesis during Fundulus epiboly*. Development, 1990. **109**(2): p. 373-86.
10. Fletcher, A.G., et al., *Implementing vertex dynamics models of cell populations in biology within a consistent computational framework*. Prog Biophys Mol Biol, 2013. **113**(2): p. 299-326.
11. Graner, F. and J.A. Glazier, *Simulation of biological cell sorting using a two-dimensional extended Potts model*. Phys Rev Lett, 1992. **69**(13): p. 2013-2016.
12. Glazier, J.A. and F. Graner, *Simulation of the differential adhesion driven rearrangement of biological cells*. Phys Rev E Stat Phys Plasmas Fluids Relat Interdiscip Topics, 1993. **47**(3): p. 2128-2154.
13. Glazier, J., A. Balter, and N. Poplawski, *Magnetization to Morphogenesis: A Brief History of the Glazier-Graner-Hogeweg Model*, in *Single-Cell-Based Models in Biology and Medicine*, A.A. Anderson, M.J. Chaplain, and K. Rejniak, Editors. 2007, Birkhäuser Basel. p. 79-106.
14. Swat, M.H., et al., *Multicell simulations of development and disease using the CompuCell3D simulation environment*. Methods Mol Biol, 2009. **500**: p. 361-428.
15. Belmonte, J.M., et al., *Self-propelled particle model for cell-sorting phenomena*. Phys Rev Lett, 2008. **100**(24): p. 248702.
16. Zhang, Y., et al., *Computer Simulations of Cell Sorting Due to Differential Adhesion*. PLoS One, 2011. **6**(10).
17. Poplawski, N.J., et al., *Simulation of single-species bacterial-biofilm growth using the Glazier-Graner-Hogeweg model and the CompuCell3D modeling environment*. Math Biosci Eng, 2008. **5**(2): p. 355-88.

18. Scianna, M., L. Munaron, and L. Preziosi, *A multiscale hybrid approach for vasculogenesis and related potential blocking therapies*. Progress in Biophysics & Molecular Biology, 2011. **106**(2): p. 450-462.
19. Starruss, J., et al., *A new mechanism for collective migration in Myxococcus xanthus*. Journal of Statistical Physics, 2007. **128**(1-2): p. 269-286.
20. Swat, M.H., et al., *Multi-scale modeling of tissues using CompuCell3D*. Methods Cell Biol, 2012. **110**: p. 325-66.
21. Andasari, V., et al., *Mathematical modeling of cancer cell invasion of tissue: biological insight from mathematical analysis and computational simulation*. Journal of Mathematical Biology, 2011. **63**(1): p. 141-71.
22. Angermann, B.R., et al., *Computational modeling of cellular signaling processes embedded into dynamic spatial contexts*. Nat Methods, 2012. **9**(3): p. 283-9.
23. Maree, A.F., et al., *Polarization and movement of keratocytes: a multiscale modelling approach*. Bull Math Biol, 2006. **68**(5): p. 1169-211.
24. Zecca, M. and G. Struhl, *Recruitment of cells into the Drosophila wing primordium by a feed-forward circuit of vestigial autoregulation*. Development, 2007. **134**(16): p. 3001-10.
25. Zecca, M. and G. Struhl, *A feed-forward circuit linking wingless, fat-dachsous signaling, and the warts-hippo pathway to Drosophila wing growth*. PLoS Biol, 2010. **8**(6): p. e1000386.
26. Shirinifard, A., et al., *Adhesion Failures Determine the Pattern of Choroidal Neovascularization in the Eye: A Computer Simulation Study*. Plos Computational Biology, 2012. **8**(5).
27. Hirashima, T., Y. Iwasa, and Y. Morishita, *Dynamic modeling of branching morphogenesis of ureteric bud in early kidney development*. Journal of Theoretical Biology, 2009. **259**(1): p. 58-66.

28. Huang, J., et al., *The mechanism of lens placode formation: A case of matrix-mediated morphogenesis*. *Developmental Biology*, 2011. **355**(1): p. 32-42.
29. Honda, H., T. Nagai, and M. Tanemura, *Two different mechanisms of planar cell intercalation leading to tissue elongation*. *Developmental Dynamics*, 2008. **237**(7): p. 1826-1836.
30. Rauzi, M., et al., *Nature and anisotropy of cortical forces orienting Drosophila tissue morphogenesis*. *Nat Cell Biol*, 2008. **10**(12): p. 1401-10.
31. Zajac, M., G.L. Jones, and J.A. Glazier, *Model of convergent extension in animal morphogenesis*. *Physical Review Letters*, 2000. **85**(9): p. 2022-2025.
32. Zajac, M., G.L. Jones, and J.A. Glazier, *Simulating convergent extension by way of anisotropic differential adhesion*. *Journal of Theoretical Biology*, 2003. **222**(2): p. 247-259.
33. Backes, T.M., et al., *Convergent extension by intercalation without mediolaterally fixed cell motion*. *Journal of Theoretical Biology*, 2009. **256**(2): p. 180-186.
34. Weliky, M., et al., *Notochord Morphogenesis in Xenopus-Laevis - Simulation of Cell Behavior Underlying Tissue Convergence and Extension*. *Development*, 1991. **113**(4): p. 1231-&.
35. Shih, J. and R. Keller, *Cell motility driving mediolateral intercalation in explants of Xenopus laevis*. *Development*, 1992. **116**(4): p. 901-14.
36. Boehm, B., et al., *The Role of Spatially Controlled Cell Proliferation in Limb Bud Morphogenesis*. *Plos Biology*, 2010. **8**(7).
37. Davidson, L.A., et al., *Integrin alpha5beta1 and fibronectin regulate polarized cell protrusions required for Xenopus convergence and extension*. *Curr Biol*, 2006. **16**(9): p. 833-44.
38. Abley, K., et al., *An intracellular partitioning-based framework for tissue cell polarity in plants and animals*. *Development*, 2013. **140**(10): p. 2061-74.

39. Keller, R.E., *The Cellular Basis of Epiboly - an Sem Study of Deep-Cell Rearrangement during Gastrulation in Xenopus-Laevis*. Journal of Embryology and Experimental Morphology, 1980. **60**(Dec): p. 201-234.
40. Ede, D.A. and J.T. Law, *Computer simulation of vertebrate limb morphogenesis*. Nature, 1969. **221**(5177): p. 244-8.
41. Niswander, L. and G.R. Martin, *FGF-4 regulates expression of Evx-1 in the developing mouse limb*. Development, 1993. **119**(1): p. 287-94.
42. Reiter, R.S. and M. Solursh, *Mitogenic property of the apical ectodermal ridge*. Dev Biol, 1982. **93**(1): p. 28-35.
43. Boehm, B., et al., *The role of spatially controlled cell proliferation in limb bud morphogenesis*. PLoS Biol, 2010. **8**(7): p. e1000420.
44. Gros, J., et al., *WNT5A/JNK and FGF/MAPK pathways regulate the cellular events shaping the vertebrate limb bud*. Curr Biol, 2010. **20**(22): p. 1993-2002.
45. Wyngaarden, L.A., et al., *Oriented cell motility and division underlie early limb bud morphogenesis*. Development, 2010. **137**(15): p. 2551-8.
46. Gao, B., et al., *Wnt Signaling Gradients Establish Planar Cell Polarity by Inducing Vangl2 Phosphorylation through Ror2*. Developmental cell, 2011. **20**(2): p. 163-176.
47. Sato, K., et al., *Morphogenetic change of the limb bud in the hand plate formation*. J Exp Zool B Mol Dev Evol, 2010.
48. Li, S. and K. Muneoka, *Cell migration and chick limb development: chemotactic action of FGF-4 and the AER*. Dev Biol, 1999. **211**(2): p. 335-47.
49. Baena-Lopez, L.A., A. Baonza, and A. Garcia-Bellido, *The orientation of cell divisions determines the shape of Drosophila organs*. Curr Biol, 2005. **15**(18): p. 1640-4.

50. Tawk, M., et al., *A mirror-symmetric cell division that orchestrates neuroepithelial morphogenesis*. Nature, 2007. **446**(7137): p. 797-800.
51. Keller, R., et al., *Mechanisms of convergence and extension by cell intercalation*. Philosophical Transactions of the Royal Society of London. Series B: Biological Sciences, 2000. **355**(1399): p. 897-922.
52. Keller, R., D. Shook, and P. Skoglund, *The forces that shape embryos: physical aspects of convergent extension by cell intercalation*. Physical Biology, 2008. **5**(1): p. 015007.
53. Voiculescu, O., et al., *The amniote primitive streak is defined by epithelial cell intercalation before gastrulation*. Nature, 2007. **449**(7165): p. 1049-52.
54. Ciruna, B. and J. Rossant, *FGF Signaling Regulates Mesoderm Cell Fate Specification and Morphogenetic Movement at the Primitive Streak*. Developmental cell, 2001. **1**(1): p. 37-49.
55. Verheyden, J.M., et al., *Conditional inactivation of Egfr1 in mouse defines its role in limb bud establishment, outgrowth and digit patterning*. Development, 2005. **132**(19): p. 4235-4245.
56. Bénazéraf, B., et al., *A random cell motility gradient downstream of FGF controls elongation of an amniote embryo*. Nature, 2010. **466**(7303): p. 248-52.
57. Gong, Y., C. Mo, and S.E. Fraser, *Planar cell polarity signalling controls cell division orientation during zebrafish gastrulation*. Nature, 2004. **430**(7000): p. 689-93.
58. Gros, J., O. Serralbo, and C. Marcelle, *WNT11 acts as a directional cue to organize the elongation of early muscle fibres*. Nature, 2009. **457**(7229): p. 589-93.
59. Heisenberg, C.P., et al., *Silberblick/Wnt11 mediates convergent extension movements during zebrafish gastrulation*. Nature, 2000. **405**(6782): p. 76-81.
60. Kilian, B., et al., *The role of Ppt/Wnt5 in regulating cell shape and movement during zebrafish gastrulation*. Mech Dev, 2003. **120**(4): p. 467-76.

61. He, F., et al., *Wnt5a regulates directional cell migration and cell proliferation via Ror2-mediated noncanonical pathway in mammalian palate development*. *Development*, 2008. **135**(23): p. 3871-9.
62. Wang, B., et al., *Disruption of PCP signaling causes limb morphogenesis and skeletal defects and may underlie Robinow syndrome and brachydactyly type B*. *Hum Mol Genet*, 2011. **20**(2): p. 271-85.
63. Barrow, J.R., et al., *Ectodermal Wnt3/β-catenin signaling is required for the establishment and maintenance of the apical ectodermal ridge*. *Genes & Development*, 2003. **17**(3): p. 394-409.
64. Parr, B.A., et al., *Mouse Wnt genes exhibit discrete domains of expression in the early embryonic CNS and limb buds*. *Development*, 1993. **119**(1): p. 247-261.
65. Chapin, H.C. and M.J. Caplan, *The cell biology of polycystic kidney disease*. *J Cell Biol*, 2010. **191**(4): p. 701-10.
66. Gallagher, A.R., G.G. Germino, and S. Somlo, *Molecular advances in autosomal dominant polycystic kidney disease*. *Adv Chronic Kidney Dis*, 2010. **17**(2): p. 118-30.
67. Harris, P.C. and V.E. Torres, *Polycystic kidney disease*. *Annu Rev Med*, 2009. **60**: p. 321-37.
68. Calvet, J.P., *Polycystic kidney disease: primary extracellular matrix abnormality or defective cellular differentiation?* *Kidney Int*, 1993. **43**(1): p. 101-8.
69. Fedeles, S.V., A.R. Gallagher, and S. Somlo, *Polycystin-1: a master regulator of intersecting cystic pathways*. *Trends Mol Med*, 2014.
70. Markoff, A., et al., *Annexin A5 interacts with polycystin-1 and interferes with the polycystin-1 stimulated recruitment of E-cadherin into adherens junctions*. *Journal of Molecular Biology*, 2007. **369**(4): p. 954-66.

71. Charron, A.J., et al., *Compromised cytoarchitecture and polarized trafficking in autosomal dominant polycystic kidney disease cells*. Journal of Cell Biology, 2000. **149**(1): p. 111-24.
72. Roitbak, T., et al., *A polycystin-1 multiprotein complex is disrupted in polycystic kidney disease cells*. Molecular Biology of the Cell, 2004. **15**(3): p. 1334-46.
73. Kher, R., et al., *Ectopic expression of cadherin 8 is sufficient to cause cyst formation in a novel 3D collagen matrix renal tubule culture*. Am. J. Physiol. Cell Physiol., 2011. **301**(1): p. C99-C105.
74. Baert, L. and A. Steg, *On the pathogenesis of simple renal cysts in the adult. A microdissection study*. Urological Research, 1977. **5**(3): p. 103-8.
75. Cho, E.A., et al., *Differential expression and function of cadherin-6 during renal epithelium development*. Development, 1998. **125**(5): p. 803-12.
76. Marciano, D.K., et al., *p120 catenin is required for normal renal tubulogenesis and glomerulogenesis*. Development, 2011. **138**(10): p. 2099-109.
77. Nouwen, E.J., et al., *Stage- and segment-specific expression of cell-adhesion molecules N-CAM, A-CAM, and L-CAM in the kidney*. Kidney Int, 1993. **44**(1): p. 147-58.
78. Wertz, K. and B.G. Herrmann, *Kidney-specific cadherin (cdh16) is expressed in embryonic kidney, lung, and sex ducts*. Mech Dev, 1999. **84**(1-2): p. 185-8.
79. Nürnbergger, J., et al., *N-cadherin is depleted from proximal tubules in experimental and human acute kidney injury*. Histochem Cell Biol, 2010. **133**(6): p. 641-9.
80. Uhlen, M., et al., *Towards a knowledge-based Human Protein Atlas*. Nat Biotechnol, 2010. **28**(12): p. 1248-50.
81. Reiser, J., et al., *The glomerular slit diaphragm is a modified adherens junction*. J Am Soc Nephrol, 2000. **11**(1): p. 1-8.

82. Song, X., et al., *Systems biology of autosomal dominant polycystic kidney disease (ADPKD): computational identification of gene expression pathways and integrated regulatory networks*. Hum Mol Genet, 2009. **18**(13): p. 2328-43.
83. Goto, S., et al., *Involvement of R-cadherin in the early stage of glomerulogenesis*. J Am Soc Nephrol, 1998. **9**(7): p. 1234-41.
84. Lee, J.E., M.H. Park, and J.H. Park, *The gene expression profile of cyst epithelial cells in autosomal dominant polycystic kidney disease patients*. Journal of Biochemistry & Molecular Biology, 2004. **37**(5): p. 612-7.
85. Blaschke, S., et al., *Expression of cadherin-8 in renal cell carcinoma and fetal kidney*. Int J Cancer, 2002. **101**(4): p. 327-34.
86. Elberg, D., et al., *Transforming growth factor- β inhibits cystogenesis in human autosomal dominant polycystic kidney epithelial cells*. Exp Cell Res, 2012. **318**(13): p. 1508-16.
87. Thedieck, C., et al., *Expression of Ksp-cadherin during kidney development and in renal cell carcinoma*. Br J Cancer, 2005. **92**(11): p. 2010-7.
88. Wendeler, M.W., et al., *Ksp-cadherin is a functional cell-cell adhesion molecule related to LI-cadherin*. Exp Cell Res, 2004. **294**(2): p. 345-55.
89. Engelberg, J.A., et al., *MDCK cystogenesis driven by cell stabilization within computational analogues*. PLoS Comput Biol, 2011. **7**(4): p. e1002030.
90. Wang, A.Z., G.K. Ojakian, and W.J. Nelson, *Steps in the morphogenesis of a polarized epithelium. I. Uncoupling the roles of cell-cell and cell-substratum contact in establishing plasma membrane polarity in multicellular epithelial (MDCK) cysts*. J Cell Sci, 1990. **95**: p. 137-51.
91. Kucken, M., et al., *An osmoregulatory basis for shape oscillations in regenerating hydra*. Biophysical Journal, 2008. **95**(2): p. 978-85.

92. Gin, E., E.M. Tanaka, and L. Brusch, *A model for cyst lumen expansion and size regulation via fluid secretion*. J Theor Biol, 2010. **264**(3): p. 1077-88.
93. Wheelock, M.J., et al., *Cadherin switching*. J Cell Sci, 2008. **121**(Pt 6): p. 727-35.
94. Martz, E. and M.S. Steinberg, *The role of cell-cell contact in "contact" inhibition of cell division: a review and new evidence*. J Cell Physiol, 1972. **79**(2): p. 189-210.
95. Benjamin, J.M., et al., *α E-catenin regulates actin dynamics independently of cadherin mediated cell-cell adhesion*. Journal of Cell Biology, 2010. **189**(2): p. 339-352.
96. Kim, J.-B., et al., *N-cadherin Extracellular Repeat 4 Mediates Epithelial to Mesenchymal Transition and Increased Motility*. Journal of Cell Biology, 2000. **151**(6): p. 1193–1205.
97. Nadasdy, T., et al., *Proliferative activity of cyst epithelium in human renal cystic diseases*. J Am Soc Nephrol, 1995. **5**(7): p. 1462-8.
98. Gossler, A. and M. Hrabe de Angelis, *Somitogenesis*. Curr Top Dev Biol, 1998. **38**: p. 225-87.
99. Dequeant, M.L., et al., *A complex oscillating network of signaling genes underlies the mouse segmentation clock*. Science, 2006. **314**(5805): p. 1595-8.
100. Wahl, M.B., et al., *FGF signaling acts upstream of the NOTCH and WNT signaling pathways to control segmentation clock oscillations in mouse somitogenesis*. Development, 2007. **134**(22): p. 4033-41.
101. Lewis, J., *Autoinhibition with transcriptional delay: a simple mechanism for the zebrafish somitogenesis oscillator*. Curr Biol, 2003. **13**(16): p. 1398-408.
102. Duband, J.L., et al., *Adhesion molecules during somitogenesis in the avian embryo*. J Cell Biol, 1987. **104**(5): p. 1361-74.

103. Glazier, J.A., et al., *Coordinated action of N-CAM, N-cadherin, EphA4, and ephrinB2 translates genetic prepatterns into structure during somitogenesis in chick*. *Curr Top Dev Biol*, 2008. **81**: p. 205-47.
104. Dubrulle, J., M.J. McGrew, and O. Pourquié, *FGF signaling controls somite boundary position and regulates segmentation clock control of spatiotemporal Hox gene activation*. *Cell*, 2001. **106**(2): p. 219-32.
105. Aulehla, A., et al., *Wnt3a plays a major role in the segmentation clock controlling somitogenesis*. *Dev Cell*, 2003. **4**(3): p. 395-406.
106. Palmeirim, I., et al., *Avian hairy gene expression identifies a molecular clock linked to vertebrate segmentation and somitogenesis*. *Cell*, 1997. **91**(5): p. 639-48.
107. Cooke, J. and E.C. Zeeman, *A clock and wavefront model for control of the number of repeated structures during animal morphogenesis*. *J Theor Biol*, 1976. **58**(2): p. 455-76.
108. Goldbeter, A. and O. Pourquié, *Modeling the segmentation clock as a network of coupled oscillations in the Notch, Wnt and FGF signaling pathways*. *J Theor Biol*, 2008. **252**(3): p. 574-85.
109. Jensen, P.B., et al., *A Wnt Oscillator Model for Somitogenesis*. *Biophysical Journal*, 2010. **98**(6): p. 943-950.
110. Uriu, K., Y. Morishita, and Y. Iwasa, *Synchronized oscillation of the segmentation clock gene in vertebrate development*. *Journal of Mathematical Biology*, 2010. **61**(2): p. 207-229.
111. Baker, R.E., S. Schnell, and P.K. Maini, *A clock and wavefront mechanism for somite formation*. *Dev Biol*, 2006. **293**(1): p. 116-26.

112. Baker, R.E., S. Schnell, and P.K. Maini, *A mathematical investigation of a Clock and Wavefront model for somitogenesis*. Journal of Mathematical Biology, 2006. **52**(4): p. 458-482.
113. Oginuma, M., et al., *Mesp2 and Tbx6 cooperatively create periodic patterns coupled with the clock machinery during mouse somitogenesis*. Development, 2008. **135**(15): p. 2555-62.
114. Watanabe, T., et al., *EphrinB2 coordinates the formation of a morphological boundary and cell epithelialization during somite segmentation*. Proc Natl Acad Sci U S A, 2009. **106**(18): p. 7467-72.
115. Christian, J.L., *BMP, Wnt and Hedgehog signals: how far can they go?* Current Opinion in Cell Biology, 2000. **12**(2): p. 244-249.
116. Gibb, S., et al., *Interfering with Wnt signalling alters the periodicity of the segmentation clock*. Dev Biol, 2009. **330**(1): p. 21-31.
117. Morelli, L.G., et al., *Delayed coupling theory of vertebrate segmentation*. HFSP J, 2009. **3**(1): p. 55-66.
118. Tiedemann, H.B., et al., *Cell-based simulation of dynamic expression patterns in the presomitic mesoderm*. J Theor Biol, 2007. **248**(1): p. 120-9.
119. Henry, C.A., et al., *Two linked hairy/Enhancer of split-related zebrafish genes, her1 and her7, function together to refine alternating somite boundaries*. Development, 2002. **129**(15): p. 3693-3704.
120. Kulesa, P.M. and S.E. Fraser, *Cell dynamics during somite boundary formation revealed by time-lapse analysis*. Science, 2002. **298**(5595): p. 991-5.
121. Tonegawa, A., et al., *Mesodermal subdivision along the mediolateral axis in chicken controlled by different concentrations of BMP-4*. Development, 1997. **124**(10): p. 1975-84.

122. Streit, A. and C.D. Stern, *Mesoderm patterning and somite formation during node regression: differential effects of chordin and noggin*. Mech Dev, 1999. **85**(1-2): p. 85-96.
123. Oates, A.C., L.G. Morelli, and S. Ares, *Patterning embryos with oscillations: structure, function and dynamics of the vertebrate segmentation clock*. Development, 2012. **139**(4): p. 625-39.
124. Online-Supplementary-Material.
125. Hamburger, V. and H.L. Hamilton, *A series of normal stages in the development of the chick embryo*. J Morphol, 1951. **88**: p. 49-92.
126. Beddington, R.S. and P. Martin, *An in situ transgenic enzyme marker to monitor migration of cells in the mid-gestation mouse embryo. Somite contribution to the early forelimb bud*. Molecular biology & medicine, 1989. **6**(4): p. 263-74.
127. Stern, C.D., et al., *A cell lineage analysis of segmentation in the chick embryo*. Development, 1988. **104 Suppl**: p. 231-244.
128. Keynes, R.J. and C.D. Stern, *Segmentation in the vertebrate nervous system*. Nature, 1984. **310**(5980): p. 786-9.
129. Takahashi, Y., et al., *Feedback loops comprising Dll1, Dll3 and Mesp2, and differential involvement of Psen1 are essential for rostrocaudal patterning of somites*. Development, 2003. **130**(18): p. 4259-68.
130. Stern, C.D. and R. Bellairs, *The roles of node regression and elongation of the area pellucida in the formation of somites in avian embryos*. J Embryol Exp Morphol, 1984. **81**: p. 75-92.
131. Fortuna, I., et al., *Growth Laws and Self-Similar Growth Regimes of Coarsening Two-Dimensional Foams: Transition from Dry to Wet Limits*. Physical Review Letters, 2012. **108**(24).

132. Martins, G.G., et al., *Dynamic 3D cell rearrangements guided by a fibronectin matrix underlie somitogenesis*. PLoS One, 2009. 4(10): p. e7429.

CURRICULUM VITAE

ADDRESS

Julio Monti Belmonte (julio.belmonte@embl.de)
EMBL Heidelberg, Meyerhofstraße 1
69117 Heidelberg, Germany

ACADEMIC FORMATION

December 2014 PhD in Physics - Biophysics track

Indiana University Bloomington – Biocomplexity Institute

Title: *Modeling Tissue Polarization and Break of Symmetry in Development and Disease*

Advisor: James A. Glazier

2007 Master of Physics.

Universidade Federal do Rio Grande do Sul, Rio Grande do Sul, Brazil.

Title: *Modelo de Animóides Aplicado à Segregação Celular (Boids Model applied to Tissue Segregation)*

Advisor: Gilberto Lima Thomas

2004 Bachelor of Physics.

Universidade Federal do Rio Grande do Sul, Rio Grande do Sul, Brazil.

Sponsorship: Fundação de Amparo à Pesquisa do Estado do Rio Grande do Sul, FAPERGS, Brazil.

COMPLEMENTARY FORMATION

2014 Modeling Cellular Processes in Space and Time (48h)
Porquerolles, France.

- 2014 Embryology: Concepts & Techniques in Modern Developmental Biology (135h)
Woods Hole Oceanographic Institution, Woods Hole, MA, USA.
- 2012 Tracking across scales: from single molecules to cells (12h)
Centre for Genomic Regulation, Barcelona, Spain.
- 2010 Q-Bio Summer School (42h)
Los Alamos National Laboratory, Los Alamos, NM, USA.
- 2008 Gene Regulatory Networks for Development (45h)
Woods Hole Oceanographic Institution, Woods Hole, MA, USA.
- 2002 Introdução à Teoria de Grupos (*Introduction to Group Theory*) (6h)
Universidade Federal de Goiás, UFG, Goiás, Brazil.

AWARDS

- 8 EIPOD-Marie Curie Fellowship, 2014.
- 7 Travel Award, USC Convergence of Sciences Short Course, 2013.
- 6 Poster Honorable Mention at 17th International Conference of Developmental Biology, 2013.
- 5 QuanTissue Short Visit Grant 4892 to James Sharpe Lab at CRG, Barcelona, Spain, 2012.
- 4 National Science Foundation (NSF) Travel Grant DMS-1135663, ECMTB/SMB 2011.
- 3 European Society for Mathematical and Theoretical Biology (ESMTB) Travel Grant, ECMTB/SMB 2011.
- 2 National Science Foundation (NSF) Travel Grant, Casablanca International Workshop 2011.

- 1 Destaque do XIII Salão de Iniciação Científica (*Award from the XII Meeting of Undergraduate Research*), Pró-Reitoria de Pesquisa/PROPESQ da Universidade Federal do Rio Grande do Sul. Brazil.

SCIENTIFIC MEMBERSHIPS

- 7 Latin American Society for Developmental Biology
- 6 American Physical Society
- 5 Society for Industrial and Applied Mathematics
- 4 Society for Developmental Biology
- 3 American Association of Anatomists
- 2 Society for Mathematical Biology
- 1 European Society for Mathematical and Theoretical Biology

PARTICIPATION IN EVENTS

- 17 Mechanobiology of Somitogenesis, 2014.
Lorentz Center, Leiden, Netherlands.
- 16 Workshop on Computational Toxicology, 2013.
Virginia Tech, VA.
- 15 From Cells to Ecosystems: Frontiers in Collaborative Quantitative Physics-Based Multiscale Modeling of Biological Processes, 2013.
Porto Alegre, Brazil.
- 14 17th International Conference of Developmental Biology, 2013.
Cancun, Mexico.

- 13 QuanTissue: Quantitative Models in Cell and Developmental Biology, 2012.
Barcelona, Spain.
- 12 Casablanca International Workshop in Mathematical Biology: Analysis and Control, 2011.
Casablanca, Morocco.
- 11 ECMTB/SMB, 2011.
Kraków, Poland.
- 10 Computational Cell Biology, 2011.
Cold Spring Harbor, NY - USA.
- 9 Cell Behaviour Ontology IX, 2011.
Bloomington, IN - USA.
- 8 Biocomplexity XI, 2010.
Bloomington, IN - USA.
- 7 Q-Bio Conference, 2010.
Santa Fe, NM - USA.
- 6 Biocomplexity X / CBO II, 2009.
Bloomington, IN - USA.
- 5 Workshop on Transport and Self-Organization in Complex Systems, 2004.
Universidade Federal do Rio Grande do Sul, Porto Alegre, RS - Brazil.
- 4 54^a Reunião Anual da Sociedade Brasileira para o Progresso da Ciência (*54th Annual Reunion of the Brazilian Society for the Progress of Science*), 2002.
Universidade Federal de Goiás, Goiânia, GO - Brazil.
- 3 XIV Salão de Iniciação Científica (*XIV Meeting of Undergraduate Research*), 2002.
Universidade Federal do Rio Grande do Sul, Porto Alegre, RS - Brazil.

- 2 Escola Regional de Alto Desempenho (*Regional School of High Performance Computing*), 2001.
Gramado, RS - Brazil.
- 1 XIII Salão de Iniciação Científica (*XIII Meeting of Undergraduate Research*), 2001.
Universidade Federal do Rio Grande do Sul, Porto Alegre, RS - Brazil.

INVITED TALKS

- 6 *CompuCell3D and Cellular Potts Modeling*
Virginia Tech, September 2013.
- 5 *Sub-Cellular Potts Model*
Universidade Federal do Rio Grande do Sul, Porto Alegre, Brazil, March, 2013.
- 4 *Multi-scale model of somite formation*
Instituto Gulbenkian de Ciência, Lisbon, Portugal, February, 2012.
- 3 *Multi-scale model of somite formation*
Universidade do Algarve, Centre for Molecular and Structural Biomedicine, Faro, Portugal, February, 2012.
- 2 *Multi-cell, Multi-scale Models of Vertebrate Somitogenesis*
University of Oxford, Centre for Mathematical Biology, Oxford, UK, July, 2011.
- 1 *Modelo computacional multiescala da somitogênese*
Universidade Federal do Rio Grande do Sul, Porto Alegre, Brazil, July, 2010 .

TEACHING EXPERIENCE

- 9 *10th User Training CompuCell3D Workshop*, Hamner Institute, Research Triangle Park, September 2014.
- 8 *Workshop on Computational Toxicology*, Virginia Tech, September 2013.

- 7 *From Cells to Ecosystems: Frontiers in Collaborative Quantitative Physics-Based Multiscale Modeling of Biological Processes*, UFRGS, Porto Alegre, 2013
- 6 *Modeling of Multicellular Development and Cancer: Hands-on Workshop*, Lorentz Center, October 2012.
- 5 *Developing Multi-Scale, Multi-Cell Biological Simulations*, Hamner Institute, Research Triangle Park, July 2012.
- 4 Teaching Assistant, Department of Physics, Indiana University, Fall 2011.
- 3 *5th User Training CompuCell3D Workshop*, Indiana University, August, 2011.
- 2 *Multi-cell, Multi-scale Modeling*, NIMBioS, University of Tennessee, Knoxville, May, 2011.
- 1 *3rd User Training CompuCell3D Workshop*, Indiana University, August, 2009.

SCIENTIFIC PRODUCTION

Scientific publications

- 4 *Somites Without a Clock*
Dias, Ana S; de Almeida, Irene; **Belmonte, Julio M**; Glazier, James A;
Stern, Claudio D
Science **343**: 791 (2014)
- 3 *Multi-scale Modeling of Tissues Using CompuCell3D*
Swat, Maciej H; Thomas, Gilberto L; **Belmonte, Julio M.**; Shirinifard, Abbas;
Hmeljak, Mitja; Glazier, James A
Methods in Cell Biology **110**: 325 (2012)
- 2 *A Multi-cell, Multi-scale Model of Vertebrate Segmentation and Somite Formation*
Hester, Susan D; **Belmonte, Julio M**; Gens, J Scott; Clendenon, Sherry G;
Glazier, James A
PLoS Comput. Biol. **7**: e1002155 (2011)

- 1 *Self-Propelled Particle Model for Cell-Sorting Phenomena*
Belmonte, Julio M; Thomas, Gilberto L; Brunnet, Leonardo G; de Almeida, Rita M C; Chaté, Hugues
Phys. Rev. Lett. **100**: 248702 (2008)

Submitted or in preparation

- 1 *3D Simulations of Wet Foam Coarsening Evidence a Self Similar Growth Regime*
Thomas, Gilberto L; **Belmonte, Julio M**; Graner, François; Glazier, James A; de Almeida, Rita M C
(submitted to Colloids and Surfaces A: Physicochemical and Engineering Aspects)
- 2 *The Cellular Basis of Limb Morphogenesis*
Lesnicar-Pucko, Gaja; **Belmonte, Julio M**; Musy, Marco; Glazier, James A; Sharpe, James A
(to be submitted to Developmental Cell)
- 3 *Novel Convergent-Extension Model by Pulling Forces*
Belmonte, Julio M; Swat, Maciej H; Glazier, James A
(to be submitted)
- 4 *Adhesion Defects are Sufficient to Initiate Polycystic Kidney Disease*
Belmonte, Julio M; Clendenon, Sherry G; Swat, Maciek H; Glazier, James A; Bacallao, Robert, L.
(in preparation)

Abstracts in events annals

- 13 *Computer Model of Renal Cyst Formation*
Belmonte, Julio M; Clendenon, Sherry G; Glazier, James A; Bacallao, Robert L
In: KIDNEY WEEK, 2013, Atlanta, GA, p. 935A.
- 12 In: AMERICAN SOCIETY FOR CELL BIOLOGY MEETING, 2013, New Orleans, LA.

- 11 *Adhesion Defects are Sufficient to Initiate Polycystic Kidney Disease*
Belmonte, Julio M; Clendenon, Sherry G; Swat, Maciek H; Glazier, James A;
Bacallao, Robert L
In: CONVERGENCE OF SCIENCES SHORT COURSE, 2013, USC, CA.
- 10 *Blood Flow and Oxygen Distribution in a Simulated 3D Liver Lobule*
Belmonte, Julio M; Fu, Xiao; Sluka, James P; Swat, Maciek H; Glazier, James A
In: MSM CONSORTIUM MEETING, 2013, Bethesda, MD.
- 9 *Modeling Somites With and Without a Clock*
Belmonte, Julio M; Dias, Ana S; Stern, Claudio D; Glazier, James A
In: 17th INTERNATIONAL CONFERENCE OF DEVELOPMENTAL
BIOLOGY, 2013, Cancun, Mexico, p. 160.
- 8 *Modeling of Epithelial Organization in PKD Cystogenesis*
Belmonte, Julio M; Clendenon, Sherry G; Glazier, James A; Bacallao, Robert L
In: KIDNEY WEEK, 2012, San Diego, CA, p. 950A.
- 7 *Multi-Cell, Multi-Scale Models Of Vertebrate Somitogenesis*
Belmonte, Julio M; Hester, Susan D; Gens, J Scott; Clendenon, Sherry G;
Glazier, James A
In: QUANTISSUE SYMPOSIUM, 2012, Barcelona, Spain.
In: ECMTB/SMB, 2011, Kraków, Poland, p. 462.
In: CASABLANCA INTERNATIONAL WORKSHOP, 2011, Casablanca,
Morocco.
In: COMPUTATIONAL CELL BIOLOGY CONFERENCE, 2011, Cold Spring
Harbor, NY, USA, p. 14.
- 3 *Modeling of the Interaction of Oscillatory Networks and Biomechanics in Somitogenesis*
Belmonte, Julio M; Hester, Susan D; Gens, Scott; Clendenon, Sherry G;
Glazier, James A
In: Q-BIO CONFERENCE, 2010, Santa Fe, NM - USA
- 2 *Estados de Equilíbrio para Espumas Bidimensionais (Equilibrium States for 2D Foams)*
Belmonte, Julio M; Grieneisen, Veronica A; Idiart, Marco A P;
de Almeida, Rita M C
In: XIV SALÃO DE INICIAÇÃO CIENTÍFICA, 2002, Porto Alegre, v. 1, p. 25.

- 1 *Simulação da Morfologia Celular Induzida por Pontos de Adesão* (Simulation of Cellular Morphology Induced by Focal Adhesions)
Belmonte, Julio M; Grieneisen, Veronica A; Castro, Mauro; Mombach, José C M;
de Almeida, Rita M C
In: XIII SALÃO DE INICIAÇÃO CIENTÍFICA, 2001, Porto Alegre, v. 1, p. 77.